Time-of-Flight Two-Photon Photoemission Spectromicroscopy with Femtosecond Laser Radiation

Dissertation
zur Erlangung des Grades
"Doktor
der Naturwissenschaften"
am Fachbereich für Physik
der Johannes Gutenberg-Universität
in Mainz

Diplom-Physiker, M.Sc. Mirko Cinchetti
geb. in Gazzaniga (Bergamo, Italien)

Part of this work has been published in:

- *Observation of Cu surface inhomogeneities by multiphoton photoemission spectromicroscopy*,
  M. Cinchetti, A. Oelsner, G.H. Fecher, H.J. Elmers, and G. Schönhense,
  Applied Physics Letters **83**, 1503 (2003).

- *Emission electron microscopy of nanoparticles in strong fs laser fields*,
  M. Cinchetti, A. Gloskovskii, D.A. Valdaitsev, A. Oelsner, G.H. Fecher, S.A. Nepjiko, H.J. Elmers and G. Schönhense,
  Microscopy and Microanalysis **9 (Suppl. 3)**, 168 (2003).

- *Photoemission time-of-flight spectromicroscopy of Ag nanoparticle films on Si(111)*,
  M. Cinchetti, D.A. Valdaitsev, A. Gloskovskii, A. Oelsner, S.A. Nepjiko, and G. Schönhense,
  Journal of Electron Spectroscopy and Related Phenomena **137-140C**, 249 (2004).

- *Two-photon photoemission spectromicroscopy from noble metal clusters on surfaces studied using time-of-flight PEEM*,
  M. Cinchetti and G. Schönhense,
  Journal of Physics: Condensed Matter, in print.

Contents

Chapter 1

Introduction

In 1908 Gustav Mie presented a work [Mie08] where he analyzed the interaction of electromagnetic radiation with small metal particles. His classical electrodynamic calculations predict well defined resonances, occurring for particular light's wavelengths, whose position depends on the dielectric properties of the material under study and on the particles size. In the Mie theory there is no attempt to give any information about the electron dynamics. In fact, the metal particles are described by their dielectric function, which summarizes all the information about the electrons' behavior. In particular, Mie simply refers to resonances of different multipolar order. Nowadays, the Mie resonances are interpreted in terms of **collective electron excitations**, called Localized Surface Plasmons (LSP's) [Sha00] or, equivalently, Surface Plasmon-Polaritons [Kre93].
The progress in the understanding of such phenomena became only possible in the last decades, when different experimental methods have been developed to produce small metal particles, also often denoted as clusters, colloids or nanoparticles. For example, beams of small particles were generated and characterized by mass spectroscopy [DH87]. At the same time, progress in surface science made it possible to grow small metal particles on a substrate by deposition of atoms from the gas phase [Ven94, Hen98].
The interest of the scientific community in the LSP's behavior is still raising. This is mainly due to the fact that LSP's possess the unique characteristic of **compressing** electromagnetic energy into a tiny volume, creating an intense local electric field that can be potentially used in many applications. Recently, the term **plasmonics** has been introduced to describe the whole range of nanotechnologies based on the excitation of LSP's in small metal particles and nanostructures, which could lead, for example, to the production of perfect lenses, rapid medical tests and superfast computers [Sch03]. Such potential applications will become reality, as soon as we will learn how

to couple light to LSP's in a controlled way.
As already mentioned, the main fingerprint of LSP's is their influence on the local fields generated close to the excited particles. Such fields are often called near-zone (NZ) fields. From this point of view, usual optical experiments [Kre93] are not suitable, since they measure the behavior of the far-fields, i.e., the fields far away from the sample[1]. On the contrary, an experimental technique which allows to study the NZ-field behavior is the so-called photon scanning tunnelling microscopy (PSTM), a modification of scanning near-field optical microscopy (SNOM) [Kre99, Sal00], developed in the last ten years.
In this thesis, we address the main question on how the excitation of LSP's affects the photoemission from small metal particles. Since photoemission is governed by the NZ-field behavior, our work opens the possibility to study the NZ-fields behavior from another point of view.
We excited LSP's in Cu and Ag nanoparticles using a pulsed, femtosecond laser with wavelength in the range of 400 nm, corresponding to a photon energy of about 3.0 eV. Since this photon energy is smaller than the work function of the studied metals, the dominant electron emission mechanism is two-photon photoemission (2PPE).
In an illustrative picture, a 2PPE process can be described as the successive absorption of two photons by an electron in a metal, followed by the emission of the electron from the solid into vacuum. Between the absorption of two photons, the occupied intermediate electron energy level undergoes a time evolution due to different relaxation mechanisms. Recording electron energy resolved 2PPE spectra allows both to gain information about the unoccupied electronic states laying between the Fermi and the vacuum level and on their relaxation dynamics [Pet97, Kno96].
2PPE spectroscopy is a spatially integrating technique and was previously applied to study homogeneous surfaces. It is possible to find some examples in literature [Mer00, Sch01a], where nanostructured samples deposited on a substrate are studied. This is possible only if there are convincing arguments allowing to distinguish between the sample and substrate contributions to 2PPE. Moreover, these previous methods did not give the possibility to laterally resolve the electrons emitted by 2PPE.
To overcome these limits, we developed a new experimental technique, called 2PPE time-of-flight spectromicroscopy, that combines the lateral resolution of an imaging photoemission electron microscope (PEEM) with spectroscopy. It makes possible to laterally resolve the electrons emitted by 2PPE and

[1] With *far away* we mean a distance which is much bigger than the linear dimensions of the studied structure and the light wavelength

simultaneously to measure their energy distribution spectra. This method gives two main advantages. First of all, it allows to gain a deep understanding into the dynamics of two-photon processes mediated by the excitation of LSP's. Secondly, it gives the unique possibility to laterally resolve the NZ-field behavior through the recorded photoemitted electrons, without the use of a scanning-probe technique.

The work is organized as follows:

- In **Chapter 2** we describe the experimental setup, concentrating our attention on the newly developed 2PPE time-of-flight spectromicroscopy technique.

- In **Chapter 3** we overview and elaborate the theoretical concepts relevant for this work. In particular, we deal with the concept of LSP's and point out that such collective electron modes can be excited by light only in small metal particles or, similarly, roughness features of a metal surface. On the contrary, no collective mode can be excited by light on a smooth surface.

  The chapter continues with the description of the behavior of NZ-fields generated close to the features where LSP's are excited. The NZ fields differ significantly from the field of the exciting electromagnetic wave and from the scattered far-fields. Basically, the NZ-fields are more intense, have a stronger spatial dependence and a different polarization.

  Finally, we give a theoretical description of 2PPE from noble metal (in particular Cu and Ag) homogeneous and rough surfaces, and explain how the NZ-fields influence the 2PPE and its dynamics.

- In **Chapter 4** we present and discuss our experimental results. We recorded 2PPE spectra from Ag and Cu nanoclusters with linear dimensions ranging between 40 nm and several 100 nm. They reveal the same qualitative differences from the spectra of the corresponding homogeneous surfaces (showing 2PPE spectra as known from literature). In particular, they show an enhanced photoemission yield (up to 70 times higher) and present a different overall shape, characterized by differences around the Fermi level onset and a steeper intensity increase at lower final state energies. These differences are explained taking into account the effects of LSP excitation in the clusters and the resulting modification of the NZ field, which in turn affects the 2PPE and its dynamics.

If from one side 2PPE spectromicroscopy gives precious information about 2PPE dynamics in small metal clusters, on the other side the lateral resolution of the 2PPE signal gives a fingerprint of the NZ field behavior. This is demonstrated by an experiment on Ag nanostructures with a well-defined shape (so-called *Ag moon-like structures*). It is shown that the laterally resolved 2PPE signal is in good agreement with the theoretical calculation of the NZ field's spatial and intensity distribution. This experiment is very promising as it provides a good technique for the direct lateral visualization of the NZ field behavior of nanostructured samples.

The Chapter ends with the description of an experiment, where non-linear electron emission of order higher than two (namely three-photon photoemission) is studied and compared to 2PPE.

- In **Chapter 5** we summarize the obtained results and the most important conclusions that can be drawn from their interpretation.

- The **Appendix (A-E)** contains results that complete the considerations presented in the Thesis.

Einleitung

1908 veröffentlichte Gustav Mie eine Arbeit [Mie08], in der die Wechselwirkung zwischen elektromagnetischen Wellen und kleinen metallischen Teilchen analysiert wird. Es handelt sich um klassische elektrodynamische Berechnungen, die sehr gut definierte Resonanzen voraussagen. Die Wellenlänge der elektromagnetischen Strahlung, bei der die Resonanzen auftreten, hängt von den dielektrischen Eigenschaften des untersuchten Materials sowie von dessen Größe ab. Die Mie-Theorie liefert keine Information über das Verhalten der Elektronen in den Metallteilchen, denn sämtliche Information hierüber wird durch deren dielektrische Funktion beschrieben. Mie's Theorie bezieht sich also nur auf Resonanzen verschiedener multipolarer Ordnungen. Heute werden solche Mie-Resonanzen als **kollektive Elektronenschwingungen** interpretiert, die von manchen Autoren als Lokalisierte Oberflächenplasmonen (Localized Surface Plasmons - LSP) [Sha00], von anderen wiederum als Oberflächen Plasmon-Polaritonen (Surface Plasmon-Polaritons) [Kre93] bezeichnet werden.

Die intensive Erforschung der LSP während der letzten Jahrzehnte wurde nur durch die Entwicklung geeigneter experimenteller Methoden zur Herstellung kleiner Teilchen, auch Clusters, Kolloide oder Nanoteilchen genannt, möglich. Beispiele hierfür sind die Erzeugung von Strahlen aus Nanoteilchen und deren Charakterisierung mittels Massenspektroskopie [Bor81, DH87] sowie das Aufwachsen kleiner Teilchen auf einem Substrat durch Abscheidung aus der Gasphase [Ven94, Hen98].

Mittlerweile steigt das wissenschaftliche Interesse an LSP stetig. Ein Zeichen dafür ist die Prägung des Wortes **Plasmonics** [Sch03], wodurch das ganze Gebiet der auf LSP-Anregung basierenden Anwendungen beschrieben wird. Die wichtigste Eigenschaft von LSP ist die Fähigkeit, elektromagnetische Energie in einem kleinen Volumen zu **komprimieren**, was letztendlich ein sehr intensives lokales elektrisches Feld entstehen lässt. Für dieses Feld, auch Nahzonenfeld (NZ-Feld) genannt, sind eine Vielzahl verschiedenster Applikationen denkbar, wie zum Beispiel die Herstellung perfekter Linsen, sehr schnelle Medizintests und superschnelle Computer [Sch03]. Die Realisierung

solcher Anwendungen wird greifbar, sobald sich die Kopplung zwischen Licht und LSP gezielt umgesetzen läßt. Wie bereits erwähnt, besteht der Fingerprint", durch den sich LSP identifizieren lassen, in ihrem Einfluss auf das NZ-Feld in unmittelbarer Umgebung des angeregten Teilchens. So gesehen sind herkömmliche lichtoptische Experimente [Kre93] unzureichend, denn diese liefern lediglich Informationen über das sog. Fernfeld. Damit bezeichnet man das elektrische Feld in einem Abstand von der Probe, der gross ist gegen die Lichtwellenlänge. Eine Methode, die die Quantifizierung des NZ-Feldes ermöglicht, ist Photon Scanning Tunneling Microscopy (PSTM). Dieses aus der Scanning Near Field Microscopy (SNOM) abgeleitete Verfahren wurde in den letzten zehn Jahre entwickelt [Kre99, Sal00].
Gegenstand dieser Doktorarbeit ist der Einfluss der LSP-Anregung auf die Photoemission kleiner Teilchen. Insbesonders werden LSP in Cu- und Ag-Nanoteilchen[2] untersucht. Als Anregungsquelle dient ein gepulster Femtosekundenlaser mit einer Wellenlänge von etwa 400 nm, was einer Photonenenergie von etwa $3,0\,\mathrm{eV}$ entspricht. Da diese Energie kleiner ist als die Austrittsarbeit der untersuchten Metalle, ist die zwei-Photonen-Photoemission (2PPE) der wahrscheinlichste Elektronenemissionmechanismus.
Schematisch beschreiben lässt sich ein 2PPE Prozess als eine aufeinander folgende Absorption zweier Photonen durch ein Elektron in einem Metall, gefolgt von der Emission des Elektrons ins Vakuum. Während der Absorption der beiden Elektronen durchläuft das besetzte Zwischenniveau aufgrund verschiedener Relaxationsmechanismen eine zeitliche Entwicklung. Mit Hilfe der 2PPE-Spektroskopie können sowohl die unbesetzten Enegieniveaus zwischen dem Fermi- und dem Vakuumniveau erforscht werden, als auch deren Relaxationsdynamik [Pet97, Kno96].
2PPE-Spektroskopie wird als lateral integrierende Methode bislang hauptsächlich für die Untersuchung homogener Proben verwendet, obwohl einige Autoren [Mer00, Sch01a] auch schon nanostrukturierte Proben untersucht haben. Dazu müssen die Beiträge von Subtrat und Probe zuverlässig getrennt werden können. Darüber hinaus ermöglicht diese Methode keine Ortsauflösung der photoemittierten Elektronen.
Um diese Beeinträchtigung zu überwinden wurde im Rahmen dieser Arbeit eine neue experimentelle Methode entwickelt, welche die 2PPE-Spektroskopie mit der lateralen Auflösung eines Elektronenmikroskops kombiniert. Die Methode wurde 2PPE-Flugzeit-Spektromikroscopie genannt. Dieses Verfahren ermöglicht es erstmals, aufgrund des 2PPE-Prozesses emittierte Elektronen lateral aufzulösen und gleichzeitig deren Energieverteilung zu messen. Die vorgestellte Technik bringt zwei entscheidende Vorteile mit sich. Erstens

[2]Die Größe der untersuchten Systemen liegt zwischen 40 nm bis zu einigen 100 nm.

ermöglicht sie ein fundamentales Verständnis der Dynamik von LSP-induzierten Zweiphotonenprozessen. Zweitens lässt sich das NZ-Feld durch die Detektion der Photoemissionselektronen lateral abbilden, ohne dabei auf probenmodifizierende Methoden wie PSTM zurückgreifen zu müssen.
Die Arbeit ist wie folgt strukturiert:

- In **Kapitel 2** wird der experimentelle Aufbau beschrieben. Der Schwerpunkt liegt dabei auf der neu entwickelten 2PPE-Flugzeit-Spektromikroscopie Methode.

- In **Kapitel 3** werden die für die Arbeit relevanten theoretischen Konzepte dargelegt und bearbeitet. Aus dem Konzept für LSP, auf das wir uns in diesem Abschnitt hauptsächlich konzentrieren, geht hervor, dass kollektive Elektronenanregung durch Licht nur in kleinen Teilchen oder in Unregelmässigkeiten wie Rauhigkeitsstrukturen der Oberfläche erfolgen kann. Im Gegensatz dazu ist die Anregung kollektiver Moden mit Photonen in glatten Oberflächen ausgeschlossen.

  Weiterhin wird das Verhalten der lokalen elektrischen NZ-Felder in unmittelbarer Umgebung der angeregten Teilchen beschrieben sowie deren signifikante Unterschiede zu den Feldern des anregenden und gestreuten Lichts. Die Hauptunterschiede bestehen in Polarisation, größerer Intensität und stärkerer Ortsabhängigkeit der NZ Felder. Dies verdeutlicht die oben gemachte Aussage über die Fähigkeit von LSP elektromagnetische Energie zu komprimieren.

  Abschließend wird eine theoretische Beschreibung des 2PPE-Prozesses für Edelmetalle (Ag und Cu) präsentiert, in der gezeigt wird, dass das Verhalten des NZ-Feldes die Hauptursache für die Unterschiede in den 2PPE-Signalen von glatten und rauen Oberflächen ist.

- In **Kapitel 4** werden die experimentellen Ergebnisse vorgestellt und diskutiert. Die 2PPE-Spektren von Ag- und Cu-Nanoteilchen mit Dimensionen zwischen 40 nm und einigen 100 nm zeigen die gleichen qualitativen Unterschiede zu den Spektren der jeweiligen homogenen Oberflächen. Insbesondere weisen die Spektren eine erhöhte Photoemissionsausbeute (bis zu 70-fach) auf sowie Unterschiede an der Fermikante wie auch steilere Anstiege bei niedrigerer Endzustandsenergie. Diese Unterschiede werden unter Berücksichtigung von LSP-Anregung in den Nanoteilchen und der daraus resultierenden Modifikation der NZ-Felder erklärt, welche ihrerseits die Dynamik des 2PPE-Prozesses beeinflusst.

  Einerseits liefert 2PPE-Spektromikroskopie wertvolle Information über die 2PPE-Dynamik in kleinen Metallteilchen. Andererseits ermöglicht

es die laterale Auflösung des 2PPE-Signals, einen Fingerabdruck des NZ-Feldes zu erhalten. Dies wird an Silber-Nanoteilchen mit definierter Form und Ausdehnung (sog. *sichelförmige Ag-Strukturen*) demonstriert. Anhand dieser Strukturen lässt sich zeigen, dass das lateral aufgelöste 2PPE-Signal gut mit theoretischen Berechnungen von räumlicher und energetischer Verteilung des NZ-Feldes übereinstimmt. Dieses Experiment ist äusserst vielsprechend, da es eine praktikable Technik liefert, die laterale Intensitätsverteilung des NZ-Feldes von Nanostrukturen direkt sichtbar zu machen.

Das Kapitel wird durch ein Experiment zur Untersuchung nichtlinearer Elektronenemission höherer Ordnung, nämlich der drei-Photonen-Photoemission abgerundet. Die Ergebnisse werden mit denen des 2PPE-Prozesses verglichen.

- **Kapitel 5** stellt die Zusammenfassung der Ergebnisse sowie der wichtigsten Schlussfolgerungen dar, die anhand der Interpretation der Resultate gezogen werden können.

- Der **Anhang (A-E)** beeinhaltet zusätzliche Ergebnisse und theoretische Überlegungen, die die Interpretationen dieser Arbeit vervollständigen.

Chapter 2

Experimental Setup

The experimental setup consisted of three main parts:

1. a femtosecond laser system, used as excitation source for nonlinear photoemission;

2. an ultra high vacuum (UHV) chamber, equipped for sample preparation and characterization;

3. a time-of-flight photoemission electron microscope (TOF-PEEM) for spectromicroscopy and a UV-lamp for reference measurements with common linear photoemission.

Figure 2.1 shows a schematic representation of the setup; its detailed description is given in the following.

2.1 The femtosecond laser system

The main component of the laser system was a pulsed Ti:sapphire laser (MaiTai, Spectra Physics) with fundamental wavelength tunable between 750 and 850 nm (photon energy $1.5 - 1.7\,\mathrm{eV}$), pulse width $< 100\,\mathrm{fs}$, repetition rate 80 MHz and average power 960 mW (at 800 nm wavelength). Its output was frequency-doubled by a commercial device with a conversion rate of 12% (at 800 nm input) and a specified output pulse width $< 200\,\mathrm{fs}$. The frequency-doubled photon beam (photon energy range: $2.9 - 3.3\,\mathrm{eV}$) was focused on the sample at an angle of 65° with respect to the surface normal. The obtained laser-spot size on the sample was $\approx 100 \times 250\,\mu\mathrm{m}^2$, giving a laser fluence pro pulse of $6.4\,\mu\mathrm{J\,cm}^{-2}$ at 3.1 eV photon energy. A Fresnel rhomb was used to rotate the polarization of the incoming light. For an incoming linear polarized photon beam with wavevector $\mathbf{k}$ there are two

orientations of the electric field **E** with respect to the sample surface: one containing a component parallel to the surface normal **n** (p-polarized light) and the other containing only a perpendicular component (s-polarized light). In other words, for p-polarized light the **E** vector lies in the plane defined by **k** and **n**, while for s-polarized light **E** is perpendicular to it; see Figure 2.2.

A flip mirror allowed to direct the fundamental (red laser) onto the sample as well, obtaining a fluence pro pulse of about $70\,\mu\mathrm{J\,cm^{-2}}$. The red laser was p-polarized.

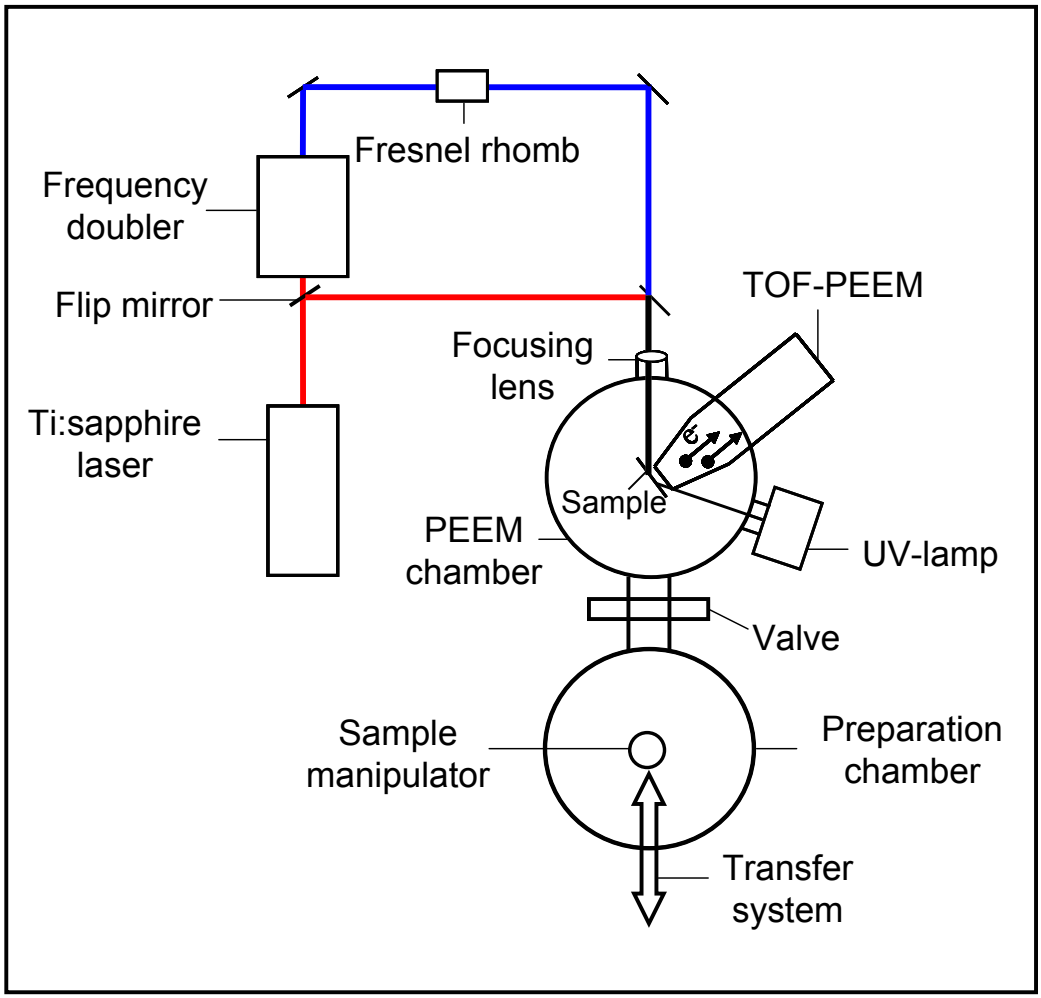

Figure 2.1: Schematic representation of the experimental setup.

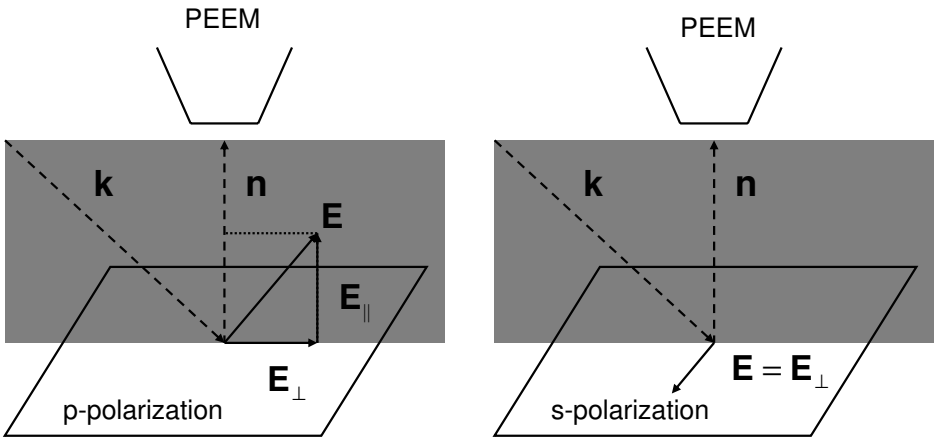

Figure 2.2: Definition of the detection geometry for p- and s-polarized light. For p-polarized light the **E** vector contains a parallel ($\mathbf{E}_{\parallel}$) and a perpendicular component ($\mathbf{E}_{\perp}$) to the surface normal **n**; s-polarized light has only the component $\mathbf{E}_{\perp}$. The photoemission microscope detects electrons in a cone around **n**.

2.2 The UHV chamber

The UHV setup consisted mainly of two parts: the standard UHV components for sample preparation and characterization, and the TOF-PEEM setup. The combination of the TOF-PEEM with the femtosecond laser source allowed us to develop a new experimental technique, namely nonlinear photoemission TOF spectromicroscopy. We discuss very briefly the standard UHV components and give a detailed description of the newly developed experimental technique.

2.2.1 Standard UHV components

The PEEM was mounted in a stainless steel UHV chamber, kept at a base pressure of $8 \cdot 10^{-11}$ mbar. The base pressure was reached by pumping with a trurbomolecular pump, an ion pump used in combination with a Ti-sublimation pump, and after baking of the system at 150°C for 50 hours. The walls of the chamber were covered with a μ-metal shield to avoid the effects of magnetic stray fields on the detection system.
The preparation chamber was coupled to a sample transfer system, which allowed the insertion of new samples without breaking the vacuum and the

transfer into the PEEM chamber. A sample manipulator allowed to move the sample in the x, y and z direction and to rotate it around the vertical z-axis. The sample was mounted on the manipulator on a sample stage, supplied with a resistive heater on the back of the sample. Direct heating was achieved by sending a current through the sample itself. The basis equipment of the chamber consisted of a sputter gun, two commercial evaporators (evaporation by electron bombardment heating), a quartz balance to allow calibration of the evaporators, and a low-energy electron diffraction (LEED) system, used to check cleanness and geometrical order of the sample surface. Two fused silica viewports with a high transparency for UV radiation were mounted to allow illumination of the sample by the laser and by a deep-UV lamp. The latter was a standard deep-UV mercury short arc lamp with 350 W average power and a photon energy range between 2.7 eV and 5.8 eV. It was used as a reference excitation source for regular (one-photon) photoemission.

2.2.2 Time-of-flight photoemission electron microscope

The main component of the setup was the TOF-PEEM. Basically, it consists of a commercial PEEM modified by integrating a low-energy drift space and combined with a (x,y,t)-resolving electron-counting detector (delay-line detector). If the photoemission is excited by a pulsed light source, this detector allows to use the PEEM as a TOF spectrometer, and thus to obtain additional spectroscopic information about the laterally resolved electron signal. In the following we describe the combination of the PEEM with the femtosecond laser system and the newly developed TOF-Spectromicroscopy technique.

The photoemission electron microscope. The PEEM is a parallel imaging microscope. It can image any flat conducting surface using laboratory light sources (high pressure mercury lamp, deuterium lamp) or Synchrotron radiation for the creation of photoelectrons via photoemission. We used a standard Focus PEEM [Sch02b]. Figure 2.3 illustrates its basic principle.
The photoelectrons emitted from the surface are accelerated by a positive voltage of at least 6 kV with respect to the sample potential into the microscope, where they go through a series of electrostatic lenses, apertures and correction elements. These potentials are regulated with respect to the main body of the microscope which is called column. It is normally kept at a positive voltage of 1 kV with respect to the sample. Finally, the photoelectron image is intensified by a multichannelplate (MCP) and imaged by a fluorescent screen for observation with a CCD camera. The contrast observed in a

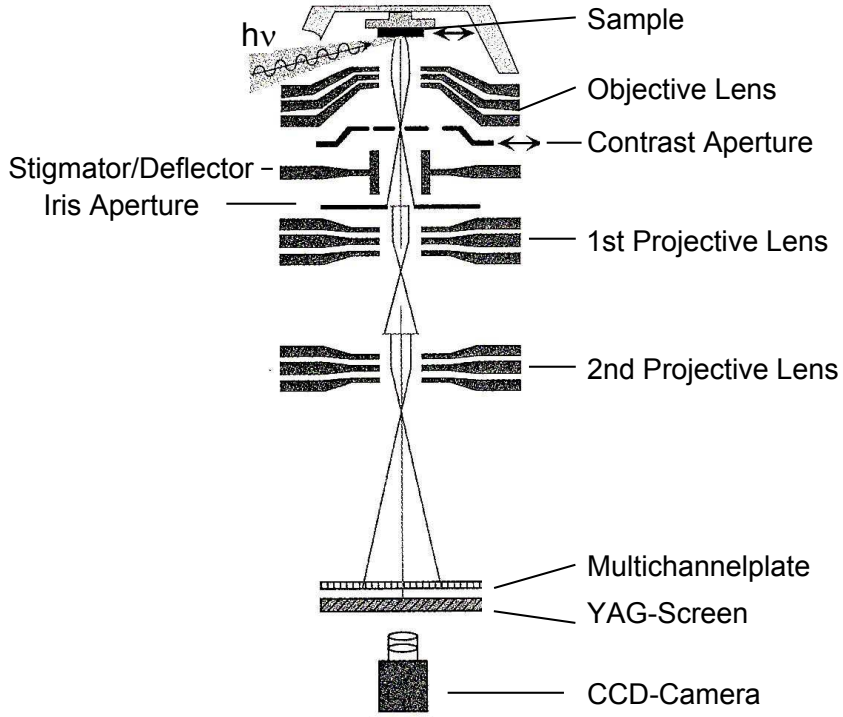

Figure 2.3: Schematic setup of a Focus PEEM.

PEEM image obtained using UV light results from spatial variations of the electron yield as a consequence of lateral variations of the local work function and of the surface topography. For higher photon energies, as available in Synchrotron facilities, element-specific imaging is also possible. More information about different designs of PEEMs and on the state-of-the-art of their performance can be found in [Gün02].

Combination of delay-line detector and femtosecond laser system. The standard imaging unit of a PEEM can be replaced by a delay-line detector. In contrast to a CCD standard unit, it allows single event readout and moreover, if the photon source is pulsed, to record the time-of-flight of the laterally resolved photoelectrons. Details of the TOF-PEEM technique and its use in Synchrotron experiments can be found for example in [Sch01c, Gün02, Oel01].
The delay-line detector consists essentially of four parts:

1. MCP-detector with delay-line anode,
2. 6-channel differential amplifier (DALATR6-module),
3. Time-to-digital-converter (TDC),
4. Computer hard- and software unit.

The MCP-detector is mounted at the end of the PEEM column, replacing the imaging unit of the standard PEEM (see Figure 2.4). It consists of a pair of MCPs mounted in front of a 2D wire-pair delay-line anode. If z denotes the axis of the PEEM (i.e., the sample surface normal direction), the wire pair lies in the (x,y)-plane. A single electron travelling through the PEEM hits the MCPs and produces a charge cloud (about $5{\cdot}10^7$ electrons), which then passes through the anode. The passage of this electron cloud through the wire pair induces an electric field pulse on the wire, i.e. a signal which can be detected

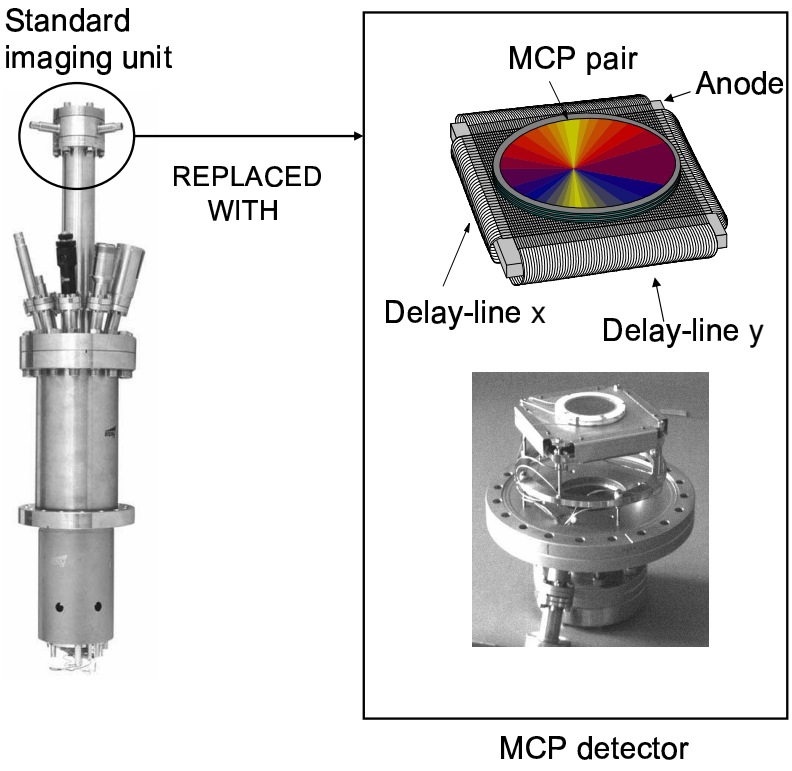

Figure 2.4: The MCP detector with delay-line anode replaces the standard imaging unit of the PEEM.

at both ends (1 and 2) of the x and y wire, denoted as delay-line x and y in Figure 2.4. Thus, every electron impinging on the MCPs generates 2 signal pairs, denoted with x_1, x_2, y_1, and y_2 in Figure 2.5. In the standard operation, these signals (*stops*), plus a reference signal taken from the back side of the MCP (*start*) are amplified by the DALATR6-module and then fed into the TDC. The TDC measures the time differences ($t_{\tilde{x}_1}$, $t_{\tilde{x}_2}$, $t_{\tilde{y}_1}$, $t_{\tilde{y}_2}$) between the *start* signal and the four *stops* and transform them into the digital array ($\tilde{x}_1$, $\tilde{x}_2$, $\tilde{y}_1$, $\tilde{y}_2$). These four values have a precise meaning. Let's assume that the electron cloud generated by a single electron hitting the MCPs reaches the point $\mathbf{P} = (\bar{x}, \bar{y})$ on the delay-line wires. For definition, the value $\tilde{x}_1$ is proportional to the time needed by the signal generated on the x wire by the electron cloud to reach the end 1 of the wire itself. Since the length of the x wire is fixed, this time can be used to calculate the value of the coordinate $\bar{x}$. Correspondingly, the meaning of the other three time differences ($\tilde{x}_2$, $\tilde{y}_1$, $\tilde{y}_2$) is clear. Thus, in principle one $\tilde{x}$ and one $\tilde{y}$ value are enough to determine the coordinates of the point $\mathbf{P}$. However, as the total delay of each line is geometrically defined (in our detector 15 m length, corresponding to ≈ 50 ns), we can increase the precision by a difference technique. In fact, the point $\mathbf{P}$

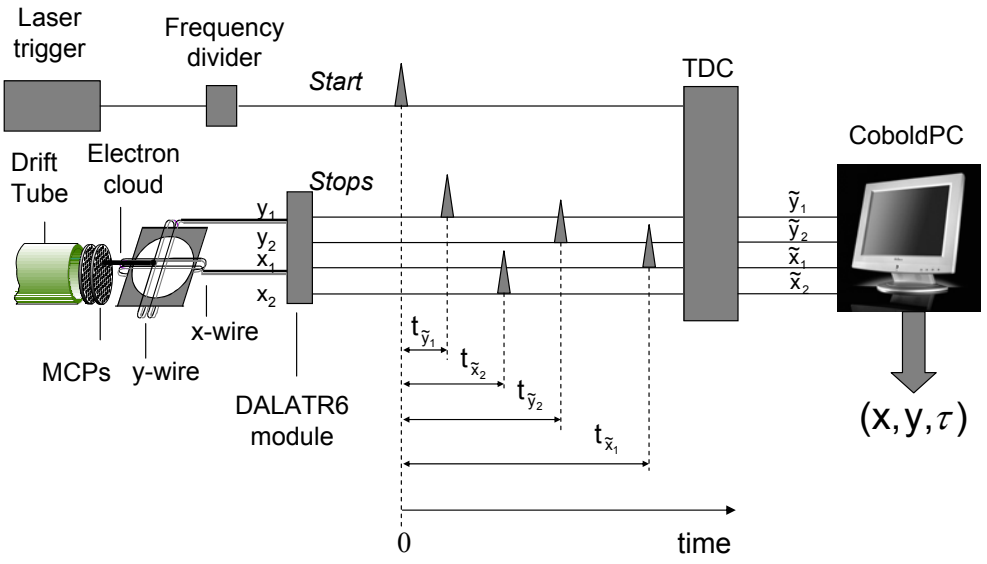

Figure 2.5: Schematic representation of the delay-line detector data processing. The 2D wire-pair has been tilted of 90° to show its details. The *start* signal is taken from the laser.

can be identified by the quantities $\Delta\tilde{x}=\tilde{x}_1-\tilde{x}_2$ and $\Delta\tilde{y}=\tilde{y}_1-\tilde{y}_2$ as well. Since $\tilde{x}_1$ and $\tilde{x}_2$ are the result of two independent measurements of two correlated events ($\tilde{x}_1+\tilde{x}_2=50\,\text{ns}$), their difference $\Delta\tilde{x}$ can be determined with a lower experimental error. The same holds for $\Delta\tilde{y}$.
The four values ($\tilde{x}_1$, $\tilde{x}_2$, $\tilde{y}_1$, $\tilde{y}_2$) are finally send from the TDC to the computer and processed by a software program (CoboldPC, RoentDek [Roe]). CoboldPC acquires these four values for every electron hitting the MCPs. A PEEM image of the sample is generated by plotting the photoemission yield (J) as a function of ($\Delta\tilde{x}$, $\Delta\tilde{y}$), and visualizing different yields with different gray levels. The photoemission yield J corresponds to the number of events registered by the DLD.
The time resolution of the TDC is $\Delta\tau_{res} = 150\,\text{ps}$. It is much larger than the width of the laser pulse ($\approx 200\,\text{fs}$). Thus, it is possible to assume that the photoelectrons excited by one laser pulse are practically simultaneously emitted. Moreover, let us assume the photoelectron energy distribution has a maximum full width of about 3 eV (cf. Chapter 4). Under these assumptions, the minimal and maximal possible kinetic energy of the photoelectrons impinging on the DLD are given by: $E_{min} = E_{col}$ and $E_{max} = E_{col} + \Delta E$, where $E_{col} \approx 1\,\text{keV}$ (corresponding to a column potential of 1 kV) and $\Delta E \approx 3\,\text{eV}$. The kinetic energy E_k is related to the time-of-flight τ by the relation:

$$E_k = \frac{mL^2}{2\tau^2} \tag{2.1}$$

where m is the electron mass and L the travelled length. The difference in the time-of-flight τ_1 and τ_2 of two electrons with respective kinetic energy E_{min} and E_{max} is given by:

$$\begin{aligned}
\Delta\tau = \tau_1 - \tau_2 &= \sqrt{\frac{mL^2}{2E_{min}}} - \sqrt{\frac{mL^2}{2E_{max}}} = \\
&= \sqrt{\frac{mL^2}{2}}\left(\frac{1}{\sqrt{E_{col}}} - \frac{1}{\sqrt{E_{col}+\Delta E}}\right) = \\
&\approx \sqrt{\frac{mL^2}{2E_{col}}}\left(\frac{1}{2}\frac{\Delta E}{E_{col}}\right)
\end{aligned} \tag{2.2}$$

where we used the fact that $E_{col} \gg \Delta E$. For $L = 1\,\text{m}$, (2.2) gives $\Delta\tau \approx 80\,\text{ps}$. Thus, the time dispersion $\Delta\tau$ of the detected electrons is negligible at 1 keV ($\Delta\tau < \Delta\tau_{res}$).
If the photon source is pulsed, its trigger can be fed into the TDC and used as *start* signal, as shown in Figure 2.5. Under the condition $\Delta\tau < \Delta\tau_{res}$

the two sums $\Sigma\tilde{x}=(\tilde{x}_1+\tilde{x}_2)$ and $\Sigma\tilde{y}=(\tilde{y}_1+\tilde{y}_2)$ are constant and proportional to the length of the x and y wire, respectively. In our experiments the photoelectrons have been dispersed in time before hitting the MCP by applying a drift voltage V_D of about 25 V (with respect to the sample potential) to the rear part of the PEEM's column, which is called - for this reason - drift tube (see Figure 2.6). Its length is approximately $L = 0.5\,\mathrm{m}$. Since the time dispersion of the electrons arriving in the drift tube is negligible, the time dispersion of the photoelectrons that have travelled through the drift tube is given by:

$$\Delta\tau = \tau_1 - \tau_2 = \sqrt{\frac{mL^2}{2}}\left(\frac{1}{\sqrt{E_D}} - \frac{1}{\sqrt{E_D + \Delta E}}\right) \approx 10\,\mathrm{ns} \qquad (2.3)$$

with E_D=25 eV. Now it holds $\Delta\tau \gg \Delta\tau_{res}$. In this case, the two quantities $\Sigma\tilde{x}$ and $\Sigma\tilde{y}$ give the time-of-flight τ of the electrons travelling through the PEEM.
In the practice, the trigger frequency (80 MHz) was too high to be used di-

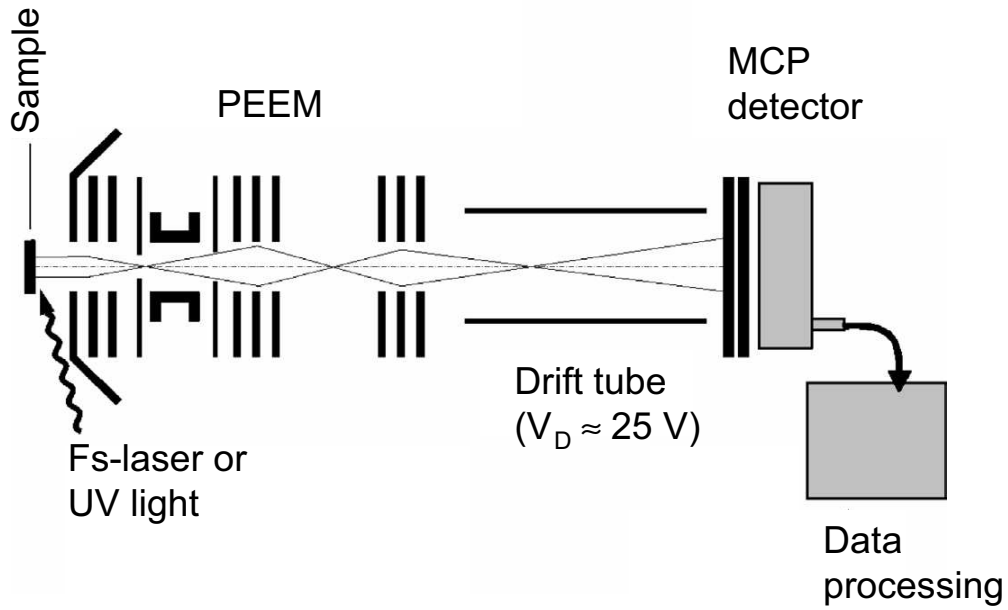

Figure 2.6: Schematic representation of the TOF-PEEM setup. The rear part of the PEEM's column - named drift tube - was kept at the drift voltage V_D of about 25 V with respect to the sample potential. The MCP detector was mounted in vacuum behind the drift tube.

rectly as start signal for the TDC. In fact, the TDC has a maximal acquisition rate of 1 MHz. This problem was solved by inserting a frequency divider before the start of the TDC (see Figure 2.5). On the other hand, we did not further treat the stop signals: experimentally we measured count rates in the order of 100 kHz, far below the laser frequency and the maximal acquisition rate of the TDC. This is due to the quantum efficiency of the photoemission process combined with the PEEM transmission function, which takes into account that not all the collected photoelectrons are imaged by the PEEM[1]. Since the transmission function T strongly depends on the electron kinetic energy, we normalized the recorded electron energy distribution curves by the function $T(E_0)$ calculated in Appendix A:

$$T(r_{ap}, E_0) \sim 8.5 \cdot 10^7 \, \frac{r_{ap}^2}{E_0} \,, \tag{2.4}$$

where r_{ap} is the radius of the used contrast aperture ($r_{ap} = 150\,\mu$m) and E_0 the initial kinetic energy at the sample surface.

The output of the DLD. To summarize, by combining the delay-line detector with the femtosecond laser source, the four coordinates ($\tilde{x}_1$,$\tilde{x}_2$,$\tilde{y}_1$,$\tilde{y}_2$) are sent from the TDC to the PC software. CoboldPC processes these values and calculates the three dimensional array (x,y,τ) for every detected electron (see Table 2.1).
In the spectromicroscopy mode, energy resolved images are generated from the (x,y) data as J(x,y) plots (J is the photoemission yield) for a fixed τ interval $\Delta\tau$ (corresponding to the desired kinetic energy interval). In the microspectroscopy mode, on the other hand, the energy distribution curves of the electrons emitted from an area of interest Δ(x,y) are plotted from the τ data fixing the corresponding (x,y) region. Note that this data analysis can be performed after the measurement, since CoboldPC can analyze the stored (x,y,τ) array in every moment. This means, in particular, that the energy resolution of the energy-filtered images and the spatial resolution of the microspectra can be varied and optimized **after** data acquisition.

Calibration of the TOF spectra. In the microspectroscopy mode the plot $J = J(\tau)$ is generated. From (2.1) one has $E_k \propto \tau^{-2}$. Using this

[1] At the present experimental condition, with high extractor voltages (> 6 kV) and narrow electron energy distributions ($\Delta E \approx 3$ eV) most of the emitted electrons are accelerated into the PEEM. Part of these electrons is then suppressed by the contrast aperture (see Figure 2.3), in order to obtain a better image contrast. An analytic expression for the PEEM transmission function is given in Appendix A.

From TDC	CoboldPC	Plots
$\tilde{x}_1$ $\tilde{x}_2$ $\tilde{y}_1$ $\tilde{y}_2$	$x \equiv \Delta\tilde{x} = (\tilde{x}_1 - \tilde{x}_2)$ $y \equiv \Delta\tilde{y} = (\tilde{y}_1 - \tilde{y}_2)$ Position coordinates $\tau \equiv \Sigma\tilde{x} = (\tilde{x}_1 + \tilde{x}_2)$ $\tau \equiv \Sigma\tilde{y} = (\tilde{y}_1 + \tilde{y}_2)$ TOF coordinates ($\tau \propto E_k^{-1/2}$)	$J=J(x,y,\tau)$ 4D-data set $\forall(x,y)$, $\tau_1 < \tau < \tau_2$: Spectromicroscopy $J_{\Delta\tau} = J(x,y)$ 3D-plot $\forall(\tau)$, $x_1 < x < x_2$, $y_1 < y < y_2$: Microspectroscopy $J_{\Delta(x,y)} = J(\tau)$ 2D-plot

Table 2.1: Coordinates calculated from CoboldPC and possible data representations (in Plots). Every detected electron generates the four coordinates ($\tilde{x}_1$, $\tilde{x}_2$, $\tilde{y}_1$, $\tilde{y}_2$) in the TDC. These values are send to CoboldPC, which calculates the three dimensional "coordinate"(x,y,τ) of the counting event. (x,y) are the spatial coordinates and τ is proportional to the TOF of the detected electron. The 4D-data set $J = J(x,y,\tau)$, where J is the accumulated number of counting events at the coordinate (x,y,τ), allows to perform spectromicroscopy and microspectroscopy on the sample.

proportionality it is possible to transform the $J(\tau)$ curves into convenient $J(E_k)$ spectra. To obtain the quantitative conversion rule, we recorded $J(\tau)$ curves from a homogeneous metal sample (Ta) for different drift voltages V_D. The electrons were excited by the blue laser. The recorded curves had a characteristic shape, see Figure 2.7 (a). We chose a typical feature of the spectra, i.e. the intensity maximum marked in Figure 2.7 (a), and followed its position for different applied drift voltages. The obtained calibration curve is shown in Figure 2.7 (b). It shows the dependence between E_D and the TOF of the electrons. This curve can also be read as the dependence between the energy of the electrons and their TOF. In fact, (2.3) shows that a change of E_D is equivalent to keeping E_D constant and changing the kinetic energy of the electrons.
The recorded two-photon photoemission spectra have a maximal width of about 3 eV. From the calibration curve it is clear that in such a small energy

interval one can assume the relation between TOF τ and kinetic energy E_k to be almost linear, and calculate the proportionality factor between τ and E_k. In Figure 2.7 (b) we marked three regions were a linear fit was performed (fitting curve: $E_k = a\tau + b$). The obtained proportionality coefficients a are shown in Table 2.2. Since the obtained coefficients are substantially different, we proceeded as follows: for a fixed value of V_D we used the a coefficient obtained from the linear fit in the region (V_D,$V_D + \Delta E$). This conversion gives an energy scale that corresponds to E_k up to an additive constant. This constant could be extracted from the fitting coefficient b. In practice, it has been chosen following physical arguments. This will be explained in Chapter 3.
Table 2.2 also shows the result of the fit with the curve

$$E_D(\tau) = \frac{C^2}{(\tau + \tau_0)^2} \ , \tag{2.5}$$

where the constants τ_0 and C have been taken as fitting parameters. The parameter τ_0 is the time in which the electrons travelled through the PEEM before being time dispersed in the drift tube by the drift voltage V_D.

	Fit 1	**Fit 2**	**Fit 3**
Linear coefficient a (eV/ns)	-0.46±0.01	-0.34±0.01	-0.26±0.01
Fit with $E_D(\tau) = \frac{C^2}{(\tau+\tau_0)^2}$	$\tau_0 = (99.1 \pm 0.4)\,\text{ns}, \quad C = (522 \pm 2)\,\sqrt{\text{eV}}\,\text{ns}$		

Table 2.2: Linear fit with the curve $E_k = a\tau + b$ of the regions Fit 1, 2 and 3 marked in Figure 2.7 (b). Only the coefficient a is relevant for our purposes. We also give the result of the fit with the curve (2.5). The constants τ_0 and C have been taken as fit parameters.

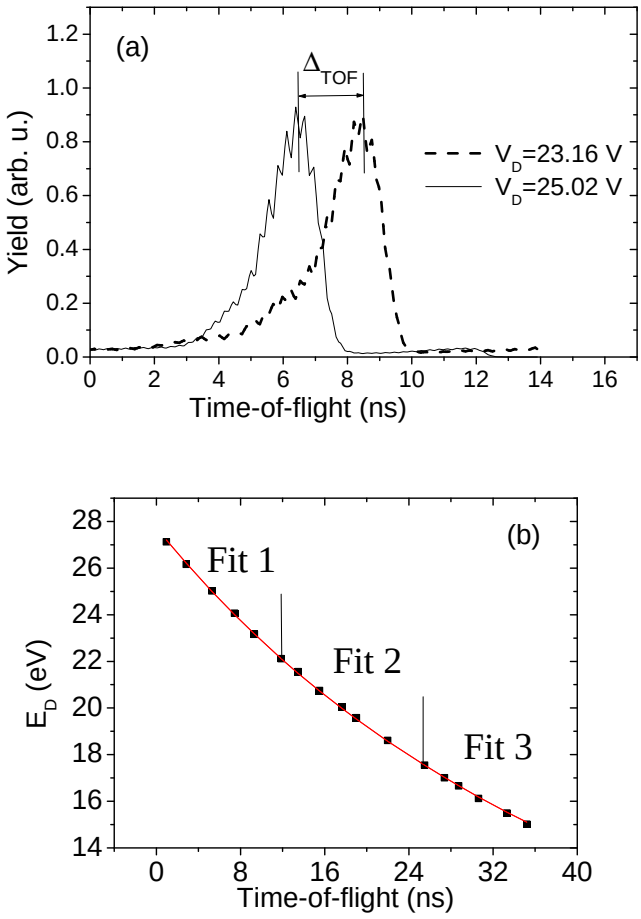

Figure 2.7: (a) $J(\tau)$ curves from a homogeneous sample recorded at different drift voltages of $V_D = 23.16\,V$ and $V_D = 25.02\,V$, respectively. The excitation source was the blue laser. The time-of-flight scale has an offset, but is always the same in every measurement. The position of the marked peak for different drift voltages has been recorded to obtain the calibration curve in (b). (b) Calibration curve for the conversion between TOF and kinetic energy.

Chapter 3

Theoretical Background

In this Chapter we give a survey over the theoretical concepts which constitute the basis to understand the experimental results presented in Chapter 4. We used TOF-spectromicroscopy to study the electron emission from Cu and Ag samples induced by photon illumination. In particular, the used photon sources were:

- the Hg UV-lamp (pressure-broadened many-line spectrum, photon energy cut-off at $\hbar\omega \approx 5.8\,\mathrm{eV}$);
- the fundamental of the fs-laser, called in the following *red laser* (photon energy range $\hbar\omega = 1.5 - 1.7\,\mathrm{eV}$);
- the frequency doubled fs-laser, called in the following *blue laser* (photon energy range $\hbar\omega = 2.9 - 3.3\,\mathrm{eV}$).

Element	**Surface**	ϕ_m (eV)
Ag	polycrystalline	4.26
	(100)	4.64
	(110)	4.52
	(111)	4.74
Cu	polycrystalline	4.65
	(100)	4.59
	(110)	4.48
	(111)	4.98
	(112)	4.53

Table 3.1: Work function ϕ_m of Ag and Cu for polycrystalline material and different crystal orientations. (Data from [Mic77].)

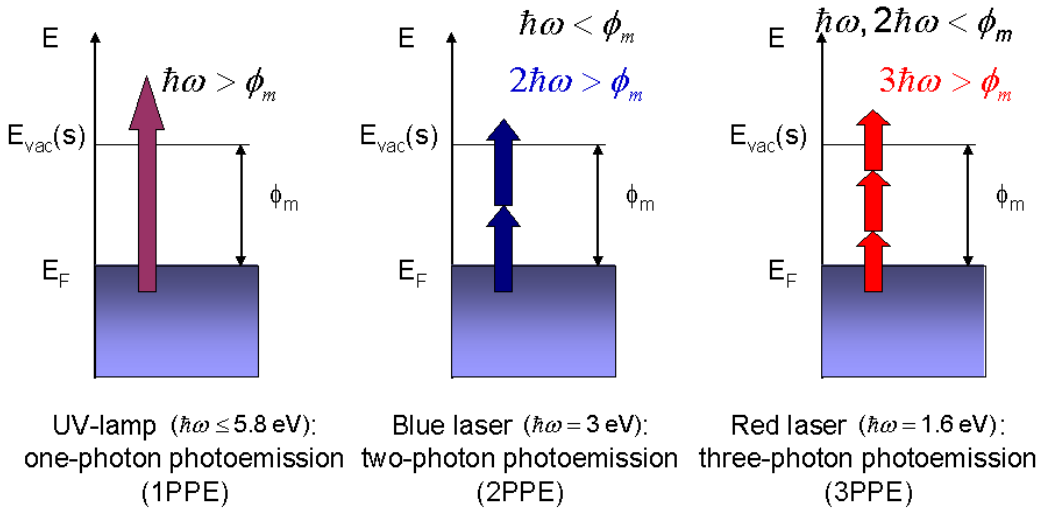

Figure 3.1: Schematic representation of the different nPPE mechanisms occurring if the sample is illuminated with the UV lamp, the blue fs-laser or the red fs-laser, respectively. The arrows indicate the transition of an electron into a state above the vacuum level $E_{vac}(s)$, following the absorption of 1, 2 or 3 photons.

Table 3.1 shows the work function (ϕ_m) of Cu and Ag, for different crystal orientations. The data are taken from [Mic77]. If such noble metals are illuminated with the UV lamp, electrons will be emitted by regular, one-photon photoemission (1PPE), since $\hbar\omega_{UV} > \phi_m$. On the other hand, if one uses the red or the blue fs-laser, $\hbar\omega_{blue/red} < \phi_m$. In this case, nonlinear photoemission can be generated through a multiphoton process nPPE, where n is the minimum number of photons at a given energy $\hbar\omega$ for which $n\hbar\omega > \phi_m$ [Mon97]. Clearly, for the blue laser $n = 2$, while for the red laser $n = 3$ or even higher, depending on the crystal orientation (see Figure 3.1)

If the sample surface is not homogeneous, a laser with frequencies in the optical region may excite localized collective modes on the surface roughnesses. These collective excitations are synchronous with the laser field and give rise to strongly enhanced near zone fields, which affect the photoemission. It will be shown in Chapter 4 that, given the present experimental conditions, the dominant electron emission mechanism remains nPPE. However, the collective excitations cause an enhancement of the photoemission intensity and influence its dynamics. Since most of the present experiments have been performed using the blue laser as excitation source, we will concentrate our attention on the theoretical description of 2PPE.

This Chapter is organized as follows: in § 3.1 we review the basic concepts used in photoemission electron spectroscopy. In § 3.2 we give an overview on the optical response of metal surfaces. In particular, it is pointed out that collective electron modes can be directly optically excited only in small metal particles or surface inhomogeneities. Such modes are commonly called Localized Surface Plasmons (LSP's). In § 3.2.4 we describe the enhancement of the near zone fields at the surface of small metal particles resulting from the excitation of LSP's in the particles themselves. This enhancement is one of the factors responsible for the strong enhancement of the 2PPE signal from rough metal surfaces with respect to homogeneous surfaces. This is discussed in § 3.3. Other possible electron emission mechanisms that could be induced by the excitation of LSP's are discussed in § 3.5. In § 3.6 we give a brief summary of the presented theoretical results.

3.1 Photoemission electron spectroscopy: the basic concepts

The *local vacuum level* of a finite-size sample $E_{vac}(\mathrm{s})$ is defined as the energy of an electron at rest outside the surface of the solid at a point where the distance between the electron and the surface is larger than the interatomic distance but smaller than the size of the crystal surface [Cah03]. This vacuum level differs from the energy of an electron at rest at infinite distance from the surface $E_{vac}(\infty)$. In a metal the difference between these two levels is due to the contribution of surface dipoles, which arise because the actual charge distribution in cells near the surface of a finite crystal differs from that of the bulk (see for example [Ash98]). Thus, $E_{vac}(\mathrm{s})$ is a local characteristic of the surface and depends on the atomic, chemical and electronic structure of the outer atomic layers of the solid. In particular, it depends on the crystallographic face and possible adsorbate layers.
The *local work function* of a metal ϕ_m is defined as the difference between the Fermi energy E_F (i.e. , the energy of the electron in the highest occupied level of the neutral ground state of the solid) and the local vacuum level $E_{vac}(\mathrm{s})$.
In photoemission electron spectroscopy (PES), photons with energy $\hbar\omega$ impinge on the sample surface and photoelectrons are emitted. The photoelectrons are then collected by a detector which records energy resolved spectra. If $\hbar\omega > \phi_m$ (like for example in Ultraviolet Photoemission Electron Spectroscopy, shortly UPS, where UV light is used) then photoelectrons are emitted by regular (one-photon) photoemission. On the other hand, if $\hbar\omega < \phi_m$

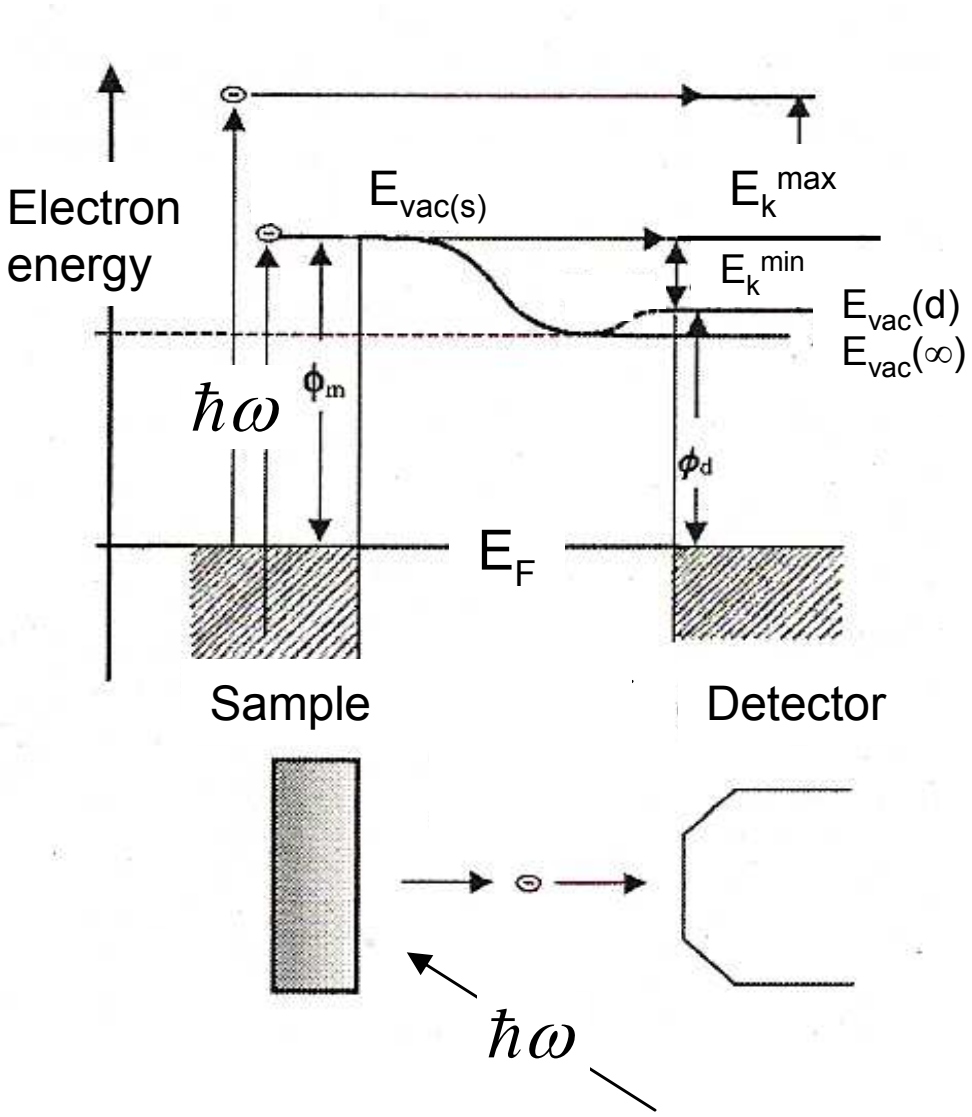

Figure 3.2: Energy diagram of a metal surface and a photoelectron detector in equilibrium (from [Cah03]). If the sample and the detector are electrically in contact (zero sample bias), the Fermi level E_F is aligned across the system. E_{vac}(s) and E_{vac}(d) are respectively the vacuum level of the surface and of the detector; ϕ_m and ϕ_d the corresponding work function. The vacuum level at infinity $E_{vac}(\infty)$ lies below E_{vac}(s) and E_{vac}(d). The maximal and minimal detectable kinetic energy of photoelectrons excited by photons $\hbar\omega$ are indicated by E_k^{max} and E_k^{min}.

photoelectrons can be emitted by successive absorption of two (or more) photons.

To make clear which physical quantities can be measured in PES, one has to keep in mind that the detector plays an important role. In fact, it is characterized by its own work function, that influences the kinetic energy of the photoelectrons. Figure 3.2 illustrates this concept. It shows the energy diagram of a metal surface in equilibrium with the electron detector. The electrons photoemitted from the Fermi level of the metal by photons $\hbar\omega$ have the maximal possible kinetic energy. The detector measures this energy as E_k^{max}. The minimal detectable kinetic energy is denoted as E_k^{min}. It corresponds to electrons that have just enough energy to escape from the solid. Such electrons may originate from an occupied state with energy $\hbar\omega$ below E_{vac}(s) or be secondary electrons excited through inelastic scattering with higher energy electrons (see § 3.5.1).

The two energies E_k^{max} and E_k^{min} are related to the vacuum level of the detector E_{vac}(d), which we assumed to be lower than E_{vac}(s). If this is not the case it is sufficient to apply a negative bias voltage to the sample, or equivalently to apply a positive voltage to the detector. This shifts the two halves of the scheme in Figure 3.2 accordingly.

E_{vac}(d) can be considered constant during the experiment. Thus, a change in E_k^{min} in the spectra corresponds to a change in the local vacuum level at the sample, i.e., to a variation in the local work function ϕ_m, which is given by $\phi_m = E_k^{min} + \hbar\omega - E_k^{max}$.

In § 3.3 we describe in detail a two-photon photoemission process. For the moment, let us assume the photoemission to proceed through a subsequent absorption of two photons with energy $\hbar\omega$, with $\hbar\omega < \phi_m$ and $2\hbar\omega > \phi_m$. Clearly, all the above considerations still hold, if one replaces $\hbar\omega$ in a regular photoemission process with the energy $2\hbar\omega$ absorbed by an electron by two-photon photoexcitation.

In our two-photon photoemission experiments the time-of-flight detector was kept at the positive drift voltage $V_D \approx 25\,V$. This corresponds in Figure 3.2 to a shift of $E_{vac}(d)$ and of the Fermi level of the detector by $-25\,eV$, i.e. towards lower energies in the chosen scale. In turn, it increases E_k^{max} and E_k^{min} accordingly. The mentioned choice assures that $E_{vac}(d) < E_{vac}(s)$ on the given scale.

Figure 3.3 shows a typical 2PPE spectrum recorded from a Cu homogeneous surface with photon energy $\hbar\omega = 3.3\,eV$. In Chapter 2 we described how the energy scale in our 2PPE spectra could be obtained from the registered TOF spectra with exception of an additive constant. We now fix this constant by

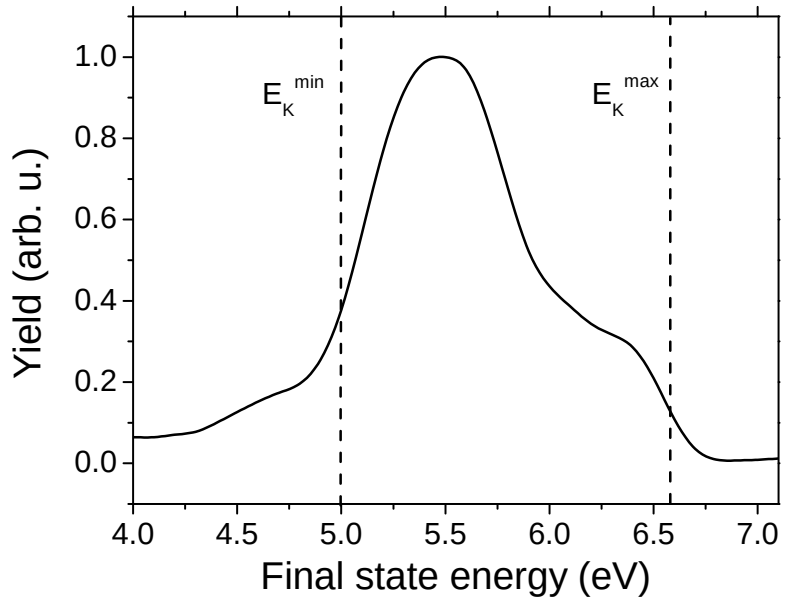

Figure 3.3: Typical 2PPE spectrum recorded with the TOF-PEEM from a homogeneous Cu surface. The photon energy was $\hbar\omega = 3.3\,\mathrm{eV}$. E_k^{max} and E_k^{min} are the maximal and minimal kinetic energy measured by the detector. The *final state energy* scale has been obtained by fixing $E_k^{max} = 2\hbar\omega = 6.6\,\mathrm{eV}$.

choosing, as usual in 2PPE spectroscopy:

$$E_k^{max} = 2\hbar\omega \tag{3.1}$$

and term the obtained energy scale as *final state energy* (E_{fin}). This is namely the kinetic energy of the detected electrons with respect to the Fermi energy of the sample. As in regular one-photon photoemission, the local work function of the sample is given by:

$$\phi_m = E_k^{min} + 2\hbar\omega - E_k^{max}\,. \tag{3.2}$$

In the chosen energy scale, one has:

$$\phi_m = E_k^{min}\,. \tag{3.3}$$

At this point it should be noticed that (3.2) has a restricted validity. To understand this, let us consider the electron emission from a small spherical particle with radius R lying on a poorly conducting medium. Wertheim

et al. [Wer83] reported that under such conditions, the positive unit charge created after the photoemission of one electron may remain on the metal particle during the time relevant to photoemission ($t \approx 10^{-15}$ s). The resulting Coulomb attraction due to this excess unit positive charge **increases** the apparent binding energy of the photoemitted electron by $\sim e^2/R$. This corresponds to a shift of E_k^{max} towards lower final state energies. Nevertheless, the position of E_k^{min} is not affected by the mentioned Coulomb attraction. In fact, E_k^{min} corresponds by definition to those electrons that have just enough kinetic energy to escape from the solid, and depends only on $E_{vac}(s)$.

On the other hand, the same positive charge **increases** the local work function (i.e. $E_{vac}(s)$) of the sphere by $\sim e^2/R$ [Wer83, Woo81][1]. On the final state energy scale, this shifts the position of E_k^{min} towards higher final state energies.

Figure 3.4 shows the typical 2PPE spectrum of a Cu homogeneous surface taken with photon energy $2\hbar\omega = 6.6\,\text{eV}$ and plotted in the final state energy scale determined by (3.1). It is compared to the simulated 2PPE spectrum from a small Cu spherical particle with radius R lying on a poorly conducting substrate. The latter spectrum is plotted on the final state energy scale of the homogeneous surface. We have chosen R such that $e^2/R \approx 0.2\,\text{eV}$. The primed quantities E'^{max}_k and E'^{min}_k indicate the discussed shifts of E_k^{max} and E_k^{min}, respectively.

Let us now evaluate the work function of the small spherical particle. Using (3.2), we obtain $\phi'_m = (5.2 + 6.6 - 6.4) = 5.4\,\text{eV}$. On the other hand, (3.3) gives $\phi'_m = 5.2\,\text{eV}$, which is the correct value.

On the basis of the above considerations, the energy scale of the spectra presented in this work have been fixed as follows. We used the 2PPE spectrum of a homogeneous metal surface to determine the final state energy scale through (3.1), and plotted all the spectra in this scale. Within this choice, equation (3.2) is not always valid to estimate the correct value of the local work function of the sample. On the other hand, equation (3.3) has a more general validity and will be used for this purpose.

Lateral variations of the local work function of the sample ϕ_m cannot be studied by spatially integrating PES alone. In fact, PES is a spatial integrating technique and is normally used to study homogeneous samples. On the other hand nonlinear photoemission (here, 2PPE) TOF-PEEM (see Table 2.1) is of advantage to study structured or inhomogeneous samples. It allows, for example, a quantitative determination of ϕ_m in different regions of the sample.

[1]The decrease of the work function of a spherical metal particle with respect to the corresponding metal plane surface, due to the different contribution of the mirror image forces [Woo81] will not be discussed here.

In fact, lateral variations of ϕ_m give different intensities in a PEEM image. To determine ϕ_m of a particular region of interest it is sufficient to choose the corresponding region Δ(x,y) in the image and to plot the curve $J_{\Delta(x,y)}(\tau)$ (i.e., the corresponding $J_{\Delta(x,y)}(E_{fin})$). Equation (3.3) gives the desired value of ϕ_m.

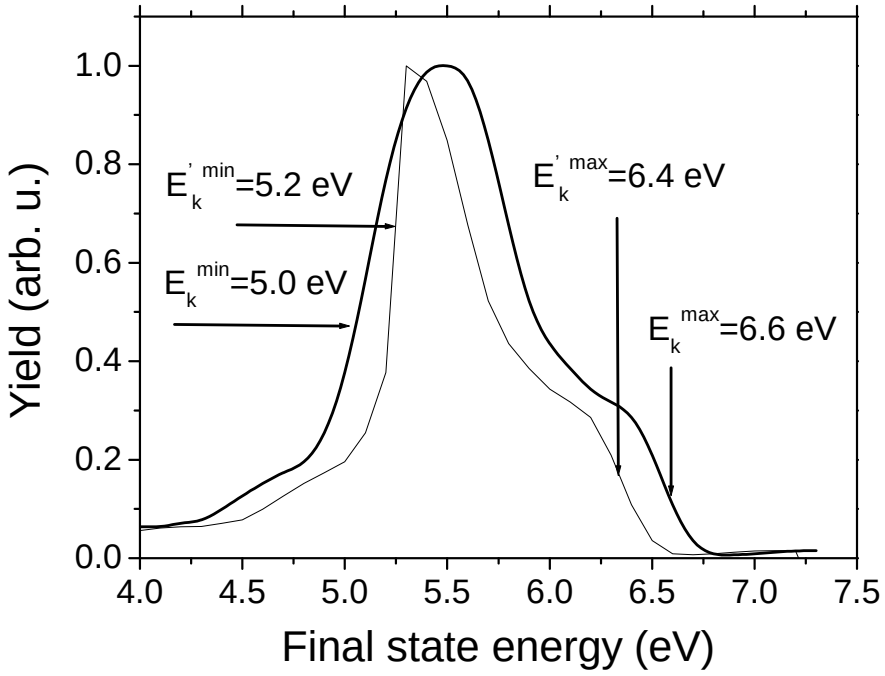

Figure 3.4: Typical 2PPE spectrum of a Cu homogeneous surface (thick line) taken with photon energy $2\hbar\omega = 6.6\,\mathrm{eV}$, plotted on the final state energy scale determined by (3.1). By definition $E_k^{max} = 6.6\,\mathrm{eV}$ and consequently $E_k^{min} = 5.0\,\mathrm{eV}$. Equations (3.2) and (3.3) give for the local work function $\phi_m = 5.0\,\mathrm{eV}$. Thin line: simulation of a 2PPE spectrum from a small Cu spherical particle with radius R on a poorly conducting substrate. It was assumed that $e^2/R \approx 0.2\,\mathrm{eV}$. The spectrum is plotted on the final state energy scale of the homogeneous surface. The shift of E'^{max}_k and E'^{min}_k with respect to E_k^{max} and E_k^{min} is discussed in the text. In this situation, only equation (3.3) gives the correct value for the work function $\phi_m = 5.2\,\mathrm{eV}$.

3.2 Optical response of metal surfaces

The irradiation of a metal surface with light in the optical region may excite electron collective modes on the surface, called surface plasmons. Following [Sha96] we distinguish between:

1. surface plasmon waves (SPW's)
2. localized surface plasmons (LSP's).

SPW's propagate laterally along the metal surface and cannot be directly optically excited on a homogeneous surface, but only by coupling to an evanescent radiation field [Ott68] or by a field impinging on a grating or on a surface with random roughness [Rae88, Bea69]. On the other hand, LSP's are optically excited in small metal particles or roughness features that are smaller than the wavelength of the incident light.
In this section the concepts of SPW and LSP are discussed. In particular, the excitation of LSP's in surface roughness features, in first approximation treated as small metal particles, is presented in detail.

3.2.1 Surface plasmon waves

In the vicinity of a metal surface, electron charges can perform coherent fluctuations which correspond to the already mentioned SPW's. Figure 3.5 shows the charges and the electric field of SPW's propagating along the x-direction at the interface between a metal and vacuum[2].
The frequency of these longitudinal oscillations depends on the wave vector k_x according to a dispersion relation $\omega(k_x)$, which can be calculated using Maxwell's equations. In particular, for a plane surface of a semi-infinite metal with dielectric function $\varepsilon = \varepsilon_1 + \imath\varepsilon_2$ adjacent to a non-absorbing medium ε_m (like air or vacuum), it holds [Rae88]:

$$\tilde{k}_x = \frac{\omega}{c}\sqrt{\frac{\varepsilon(\omega)\varepsilon_m(\omega)}{\varepsilon(\omega)+\varepsilon_m(\omega)}} \tag{3.4}$$

Since ε has an imaginary part, also $\tilde{k}_x$ will be, in general, complex. Its imaginary part determines the internal absorption, and will not be discussed here. The real part k_x is given by:

$$k_x = \frac{\omega}{c}\sqrt{\frac{\varepsilon_1(\omega)\varepsilon_m(\omega)}{\varepsilon_1(\omega)+\varepsilon_m(\omega)}} \tag{3.5}$$

[2]Note that in this idealized view the screening inside the metal has been neglected.

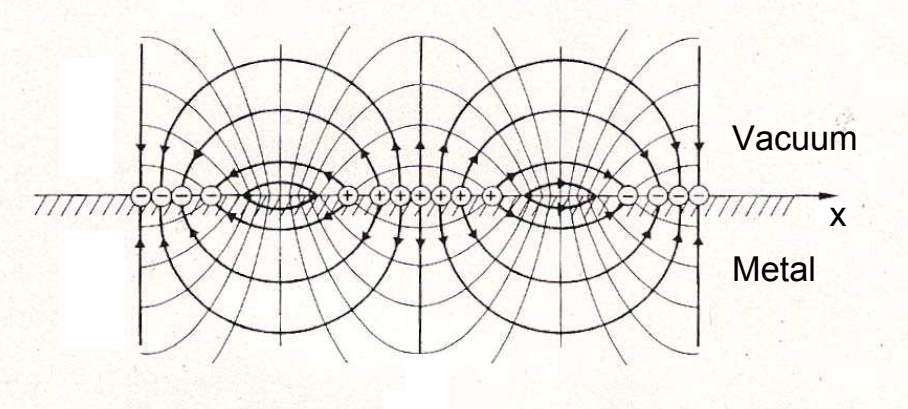

Figure 3.5: Schematic view of the potential (thin lines) and the electric field (thick lines) induced by a SPW at the interface between metal and vacuum, adapted from [Des93].

The explicit form of $\varepsilon(\omega)$ can be found only by using a physical model for the electrons in the metal. A simple classical calculation for a homogeneous and isotropic medium in the Drude model gives (see Appendix B):

$$\varepsilon_1(\omega) = 1 - \frac{\omega_p^2}{\omega^2}\,. \tag{3.6}$$

The frequency ω_p is the plasma frequency:

$$\omega_p = \sqrt{\frac{4\pi n e^2}{m}} \tag{3.7}$$

where n is the electron density, and m the electron mass. Inserting equation (3.6) into (3.5) with $\varepsilon_m = 1$[3], gives for the dispersion relation:

$$k_x(\omega) = \frac{\omega}{c}\sqrt{\frac{\omega^2 - \omega_p^2}{2\omega^2 - \omega_p^2}}\,. \tag{3.8}$$

Figure 3.6 shows the theoretical dispersion curve $\omega = \omega(k_x)$ of a free electron metal with electron density n of aluminium, according to equation (3.8). For large k_x, or

$$\varepsilon_1 \longrightarrow -\varepsilon_m \tag{3.9}$$

[3]We consider the case where the adjacent medium is vacuum, being valid for our experiment.

the value of ω approaches the limit value

$$\omega_{SPW} = \frac{\omega_p}{\sqrt{1+\varepsilon_m}}, \tag{3.10}$$

which is often called the SPW resonance.
In general SPW's cannot be directly excited with light. This is due to the fact that their dispersion relation lies to the right of the line $\omega = ck$ denoting an electromagnetic wave, as is clearly visible in Figure 3.6.

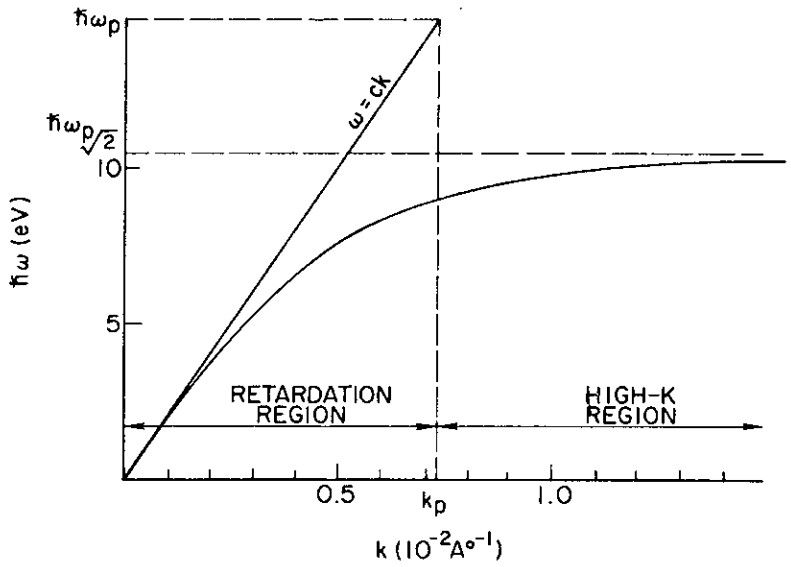

Figure 3.6: SPW dispersion curve for a free electron metal with the electronic density of Al and $\varepsilon_m = 1$, from [End70]

3.2.2 Localized surface plasmons

If the surface is not homogeneous, but presents features which are smaller than the wavelength of the incoming electromagnetic radiation in vacuum, then LSP's can be excited at the surface. This is due to breaking of wave vector conservation by the surface [Voi01]. In a more correct quantum mechanical description, the wave vector is no more a good quantum number

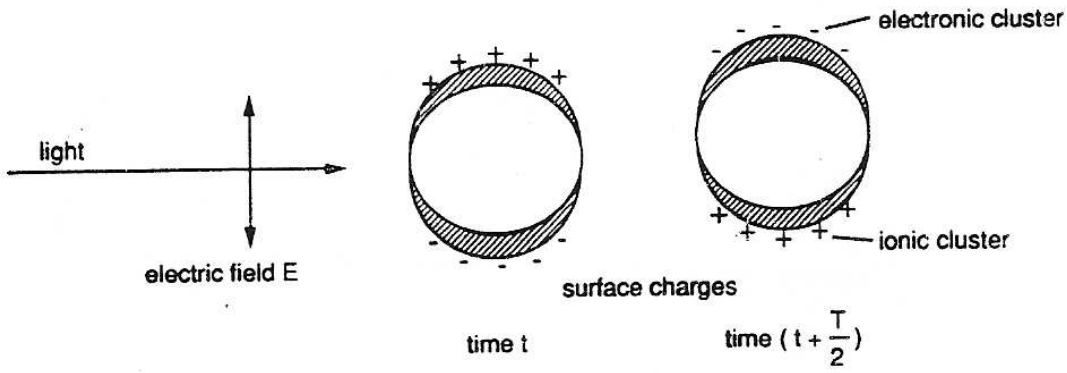

Figure 3.7: Excitation of a dipolar LSP by the linearly polarized electric field E with period T, from [Kre93].

because the wave functions of the electrons in a well have to be used instead of the Bloch waves in the bulk. As a consequence, photon absorption and consequently LSP excitations become possible [Kaw66, Per81, Hac86].
We first consider a *spherical metal particle* of radius R embedded in a homogeneous medium with real dielectric constant ε_m. The optical response of such a sphere, i.e., its dielectric function

$$\varepsilon(\omega) = \varepsilon_1(\omega) + \imath\varepsilon_2(\omega) \tag{3.11}$$

can again be easily calculated with classical electrostatic calculations in the limit $\lambda \gg R$. This is called *quasi-static regime* because only the time dependence of the electric field $\mathbf{E}$ is considered but not its spatial variation ($\mathbf{E}(\mathbf{r}, t) \cong \mathbf{E}(t)$), see Figure 3.7.
The metal is considered as a collection of positive ions immersed in the valence electron gas. Within this approximation, and in the quasi-static regime, the internal field $E_i(\omega)$ produced inside the sphere in presence of the external field $E_0(\omega)$ can be written as [Kre93]:

$$E_i(\omega) = E_0(\omega)\frac{3\varepsilon_m}{\varepsilon(\omega) + 2\varepsilon_m} \ . \tag{3.12}$$

From (3.12) it is clear that the sphere shows an enhanced response to the external field whenever $|\varepsilon + 2\varepsilon_m|$ has a minimum, i.e, when:

$$|\varepsilon_1(\omega) + 2\varepsilon_m|^2 + |\varepsilon_2|^2 = \text{Min.} \tag{3.13}$$

For small $\varepsilon_2(\omega)$, i.e. small damping, condition (3.13) is satisfied for:

$$\varepsilon_1(\omega_{LSP}) = -2\varepsilon_m \ . \tag{3.14}$$

Using (3.6) for ε_1, one finds for the resonance frequency ω_{LSP}:

$$\omega_{LSP} = \frac{\omega_p}{\sqrt{1+2\varepsilon_m}} \ . \tag{3.15}$$

The same expression for the resonance frequency ω_{LSP} can be found, as a limit case, in the context of the more detailed Mie Theory [Mie08]. This theory is an exact electrodynamic calculation (i.e., not in the quasi static regime) valid for every spherical metal particle. It considers the dielectric function as an unknown parameter, that summarizes all the information on the electron dynamics. This parameter is used to evaluate (or fit) the optical absorption and scattering of an external electromagnetic field from a spherical metal particle. The main results of the Mie theory are exhaustively presented in [Str41]. A periodic electromagnetic wave incident on a metal sphere gives rise to a forced oscillation of free and bound charges, synchronous with the applied field. These forced charge movements produce a secondary field both inside and outside the sphere. The resultant field at any point is then the vector sum of the primary and the secondary fields. Figure 3.8 shows the electric and magnetic lines of force of the secondary field excited by the first four partial (spherical) waves in which the primary (incident) electromagnetic field can be expanded.
On the other hand, every material body closed by a bound surface can be characterized by a set of characteristic frequencies ω_{free}, corresponding to the *natural modes* of the body itself, i.e. to the system of standing waves that build up in the body because of its closed surface. Clearly, whenever the frequency ω of the incident wave approaches a characteristic frequency ω_{free}, resonance phenomena will occur. Such resonances are the classical analog of the modern concept of LSP's [Kre70].
Generally speaking, in order to detect experimentally an LSP resonance, the extinction coefficient σ_{ext} is measured through optical experiments. This quantity is defined as the sum of absorption and scattering coefficients and is defined appropriately in § 3.2.4. Here it is just important to notice that in a typical optical experiment the fields *far away* from the sample are measured, where *far away* means at a distance which is much larger than the linear dimensions of the studied structure and the light wavelength. These fields are called **far fields**. They consist of outgoing electromagnetic waves, that are transverse. On the other hand, the field close to the studied structure, called **near zone** (NZ) **field**, may be distorted with respect to the far field.

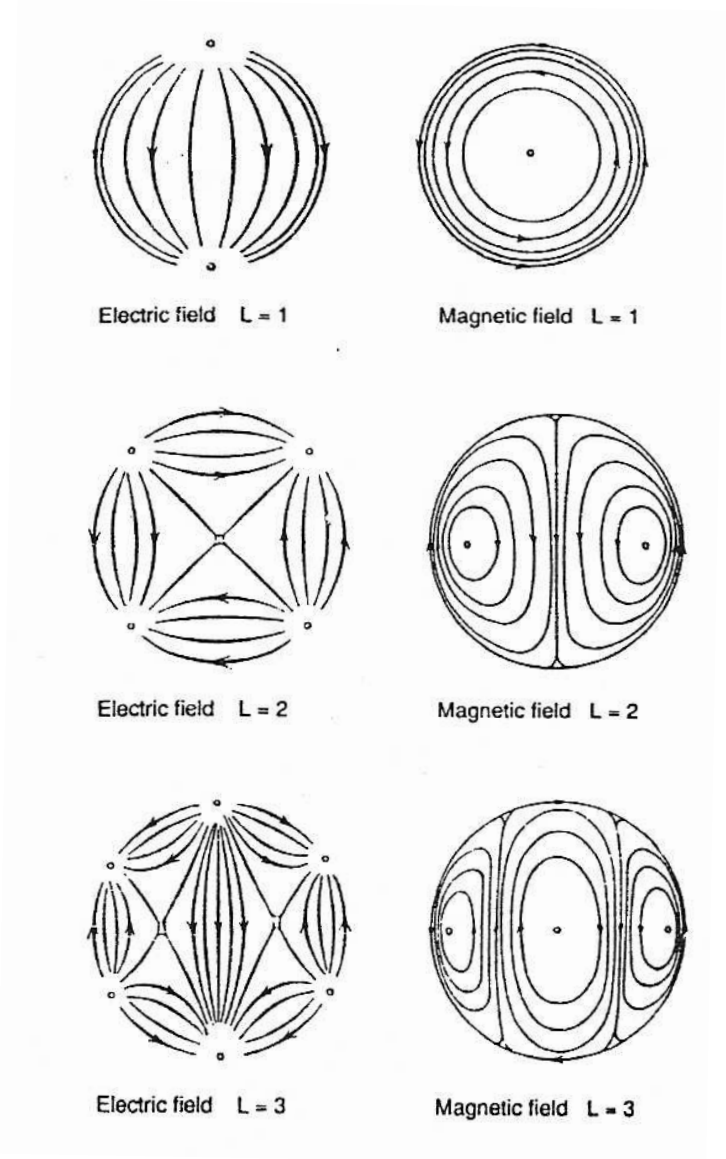

Figure 3.8: Electric and magnetic fields far away from a metal sphere, of the $L = 1, 2$ and 3 electric partial waves, i.e. the electric dipole, quadrupole and octupole modes. Note that these patterns do not correspond to the near-zone field of a particle but rather to the far field observed in Mie scattering, from [Str41].

Their behavior in the vicinity of the LSP resonance is discussed in detail in § 3.2.4.
Considering only the far field behavior and working in the quasi-static regime, the Mie theory gives for the extinction coefficient of a small metal sphere immersed in a non-absorbing medium with dielectric constant ϵ_m:

$$\sigma_{ext}(\omega) = 9\frac{\omega}{c}\varepsilon_m^{3/2}V\frac{\varepsilon_2(\omega)}{[\varepsilon_1(\omega)+2\varepsilon_m]^2+\varepsilon_2(\omega)^2}\ , \tag{3.16}$$

where $V = (4\pi/3)R^3$ is the volume of the sphere. Equation (3.16) is valid independently on the model used to calculate $\varepsilon(\omega)$, like for example the Drude model used to obtain (3.6). As expected, it has a maximum when (3.13) holds, i.e. at the frequency ω_{LSP} of (3.15), that is per definition a characteristic frequency of the free electron gas in the metal sphere.
Let us now summarize the approximations used to obtain (3.15) and make some considerations about its validity:

- we are dealing with a spherical metal particle with radius R embedded in a non-absorbing medium with constant dielectric function ε_m;
- we assumed for the magnetic permeability $\eta(\omega) = 1$. This is a good approximation for frequencies in the optical region [Kre93];
- we are in the quasi-static regime, i.e, $\lambda \gg R$: the external field is assumed to be only time dependent;
- the implication between (3.13) and (3.14) holds only if ε_2 is small or does not vary much in the vicinity of the resonance. This is well fulfilled by alkali metals like sodium, but not, for example, by gold.
- the Drude model for metals was used to obtain (3.15): this result is valid only for free-electron metals. On the other hand, condition (3.13) and equation (3.16) have a more general validity. When the Drude approximation is not valid, it is possible, for example, to measure the extinction coefficient σ_{ext} through optical experiments and use (3.16) to find the dispersion relation $\varepsilon(\omega)$.
- in the calculations of the resonance frequency ω_{LSP} and the extinction cross section (3.16) only the dipole far fields are considered. This is suitable for the usual optical experiments with detectors at large distances. However, we pointed out that in the vicinity of the sphere, the NZ fields may be extremely distorted. The NZ fields play a decisive role in the determination of the photoemission properties of metal clusters (see § 3.3).

Under these assumptions the resonance frequency ω_{LSP} does not depend explicitly on the particle radius R. It is also called the *dipole* localized plasmon frequency, because it is obtained from the first term of the expansion of the external field in spherical waves ($L = 1$ in Figure 3.8). The dipole oscillation of the free electron gas within the above mentioned approximations is depicted in Figure 3.7.
In the size range $10\,\text{nm} < R < 100\,\text{nm}$ the approximation $R \ll \lambda$ does not hold anymore and the so called *extrinsic size effects* due to the retardation of the field across the particle become relevant. This causes a red-shift of the dipole resonance. Moreover, the higher modes ($L \geq 2$) come into play and give rise to higher-order resonances in the absorption and extinction cross section. Figure 3.9 shows schematically the dependence of the position of the dipolar resonance for spherical metal particles as function of the radius R. Note that for particles with $R \leq 3\,\text{nm}$ there are deviations from the constant behavior predicted above due to quantum size effects. We will not further discuss these effects (*intrinsic size effects*) since we are mainly interested in metal particles with larger radii.
To conclude, we give a short list of all factors that do influence the position of the dipolar resonance ω_{LSP} in small metal particles or do introduce higher-order resonances:

Shape: if the particles have irregular shapes very large shifts (generally towards the red) and splitting of the resonance occur [Kre85].

Dimensions: as in the case of spherical particles (Figure 3.9), and depending on the size, intrinsic or extrinsic size effects are present.

Metal/medium interface: the physical and chemical properties of the medium influence the resonance position. Moreover, the contact area between medium and metal particles plays an important role [Hil01].

Particle density: electromagnetic coupling among densely packed particles can give rise to a variety of band shifts and splittings, depending on the sample topology [Höv97].

The reason for the dependence of ω_{LSP} from the above mentioned factors is clear. As underlined, LSP excitation occurs whenever the frequency of the incoming electromagnetic field ω approaches one of the free-oscillation frequencies (natural modes) ω_{free}. Such frequencies depend, of course, on the boundary conditions at the particle's surface, .i.e. on its shape, dimensions and moreover on the electromagnetic interactions between different particles or with the substrate.

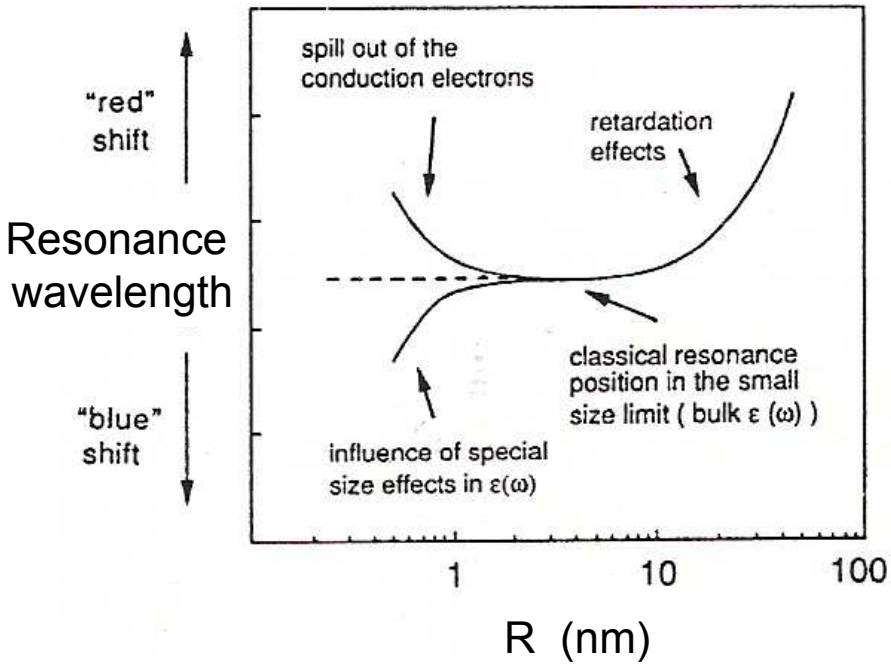

Figure 3.9: Schematic dependence of the position of the dipolar plasmon resonance in a metal sphere as function of its radius R, from [Kre93].

3.2.3 Localized surface plasmons in Cu and Ag metal nanoparticles

In Table 3.2 we evaluate the frequencies ω_p, ω_{SPW} and ω_{LSP} for different metals, assuming $\varepsilon_m = 1$, and using equations (3.7), (3.10) and (3.15), derived for a free-electron metal. Since the alkali metals (Na, K) can be modelled with good precision as free-electron metals, one expects a good agreement between the data in Table 3.2 and experiments. This is actually the case: for example, the measured dielectric function of K [Smi69] gives the value $\omega_p = 3.9\,\text{eV}$ which is reasonably close to the free electron value of $4.3\,\text{eV}$. A complete agreement with the experimental data is achieved by taking into account core electron polarization effects in the theoretical calculations [Kre93].

In contrast to alkali metals, Cu and Ag do not behave as free-electron metals in the investigated spectral region of the plasma resonance peak. Thus, the behavior of the dielectric function of noble metals like Ag and Cu cannot be even roughly estimated with the free-electron model. For example, in

Metal	$\hbar\omega_p$ (eV)	$\hbar\omega_{SPW}$ (eV)	$\hbar\omega_{LSP}$ (eV)
Na	6.0	4.2	3.4
K	4.3	3.1	2.5
Cu	10.8	7.6	6.2
Ag	9.0	6.3	5.2

Table 3.2: Evaluation of the resonance energies $\hbar\omega_p$, $\hbar\omega_{SPW}$ and $\hbar\omega_{LSP}$ in the free-electron approximation for different alkali and noble metals, with the assumption $\varepsilon_m = 1$ and using (3.7), (3.10) and (3.15).

[Hag75] the observed value of the bulk plasma frequency of Ag is 3.76 eV, that is indeed much smaller than the free-electron value of 9.0 eV.
The different behavior of the noble metals is due to the influence of the electrons in the filled d bands, whose onset is at 2 eV and 4 eV below E_F for Cu and Ag, respectively. Figure 3.10 shows the real and imaginary part of the dielectric function of bulk Ag and Cu. The imaginary part ε_2 shows the characteristic free electron behavior ($1/\omega^3$, see Appendix B) below 2 eV in Cu and 4 eV in Ag. The onset of interband absorption produces drastic changes in ε_2.

LSP in Ag particles. At excitation energies below 4 eV, interband transitions in Ag are still not effective. Liebsch [Lie93] introduced a theoretical model to take into account the influence of the Ag $4d$ electrons in the calculation of the resonance frequency ω^*_{LSP} in Ag particles in the limit where extrinsic size effects are still not present. The main idea of this approach is to consider the modification of the fields in the particles due to the mutual polarization of the *sp* and d electron densities. In this context the dielectric function of Ag can be decomposed into a large negative contribution of the *sp*-band electrons (free-electron term) and a *bound* contribution $\varepsilon_d(\omega)$ that is real and has a value of +5 to +6 in the resonance region, well below the onset of interband transitions involving the filled $4d$ states. The *sp*-band has free-electron character near E_F, whereas the electrons in the occupied $4d$ band constitute a polarizable medium. The latter reduces the energy of the

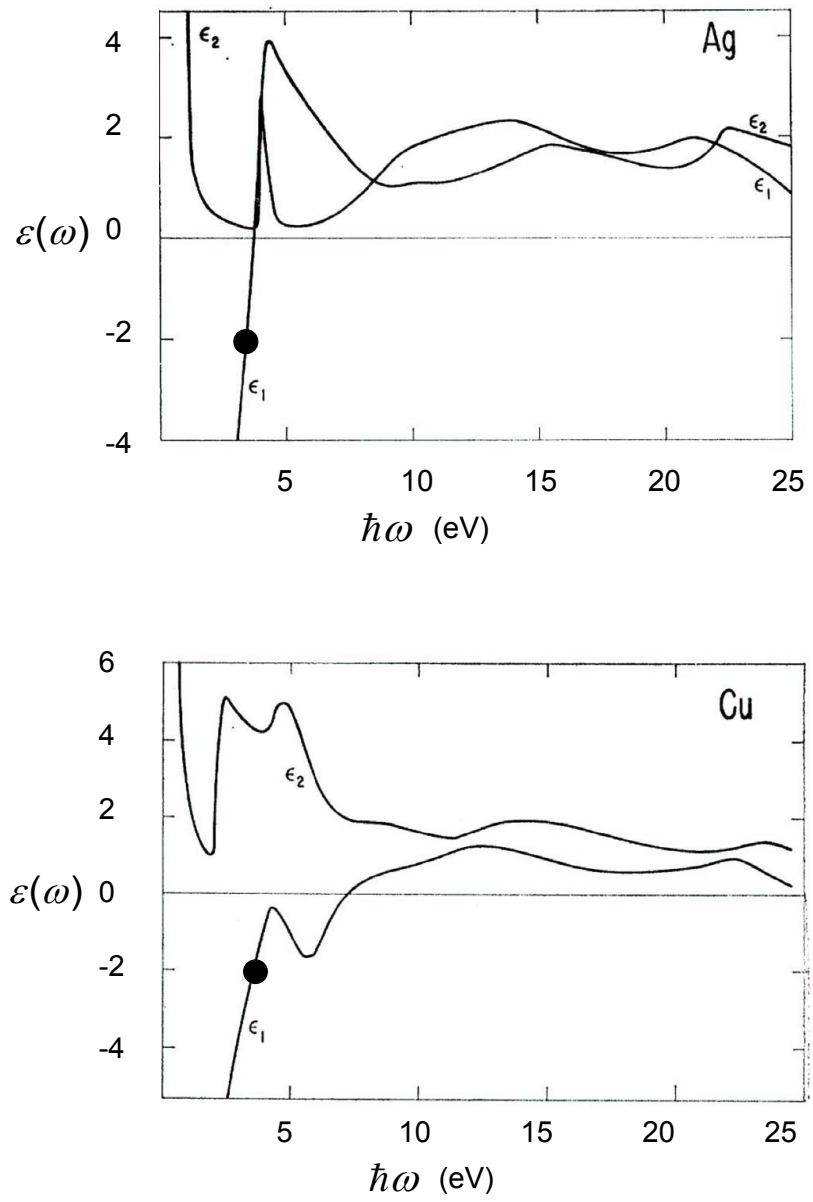

Figure 3.10: Spectral dependence of the real and imaginary part ε_1 and ε_2 of the dielectric function of bulk Ag (top) and bulk Cu (bottom), obtained from reflectance measurements in [Ehr62]. The circles denote the LSP resonance condition for spherical particles in vacuum (cf. equation (3.15)).

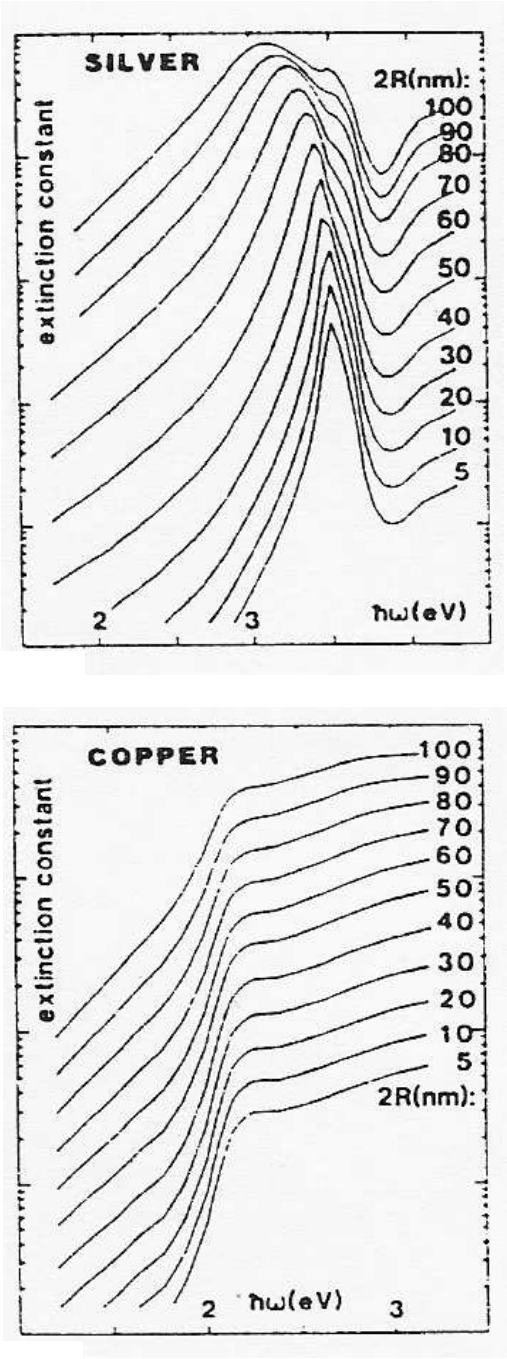

Figure 3.11: Comparison between the calculated extinction spectra of Ag and Cu spheres in vacuum for different values of the radius R, from [Kre93].

LSP resonance in the large particle limit to

$$\hbar\omega^*_{LSP} = \frac{\hbar\omega_p}{\sqrt{2 + \Re\varepsilon_d}}\,, \tag{3.17}$$

where $\Re$ indicates the real part. This yields for Ag:

$$\hbar\omega^*_{LSP}(\mathrm{Ag}) = 3.5\,eV\ , \tag{3.18}$$

well below the unscreened value $\hbar\omega_{LSP} = 5.2\,\mathrm{eV}$ of Table 3.2, and in good agreement with the measurements presented in [Tig93]. With decreasing particle size the Ag dipolar resonance is blue-shifted, in contrast to simple-metal nanoparticles. This can be explained in terms of a reduced *s-d* interaction in the surface region, where the *s*-electrons spill out into the vacuum. The relative contribution of the surface of a sphere scales with R^{-1}: thus, the screening is reduced with decreasing radius. This behavior is evident from the extinction spectra of Ag spherical particles with different radii R shown in Figure 3.11.

LSP in Cu particles. Due to the contribution of interband transitions the energy of the LSP excitation in Cu spherical particles is shifted from the free-electron value of 6.2 eV (Table 3.2) to the value [Kre93]:

$$\hbar\omega^*_{LSP}(\mathrm{Cu}) = 2.1\,eV\ . \tag{3.19}$$

In contrast to Ag, the LSP resonance does not coincide with the minimum of ε_2 (see Figure 3.10). The calculated extinction spectra for spherical Cu particles with different radii R are compared to the spectra for Ag in Figure 3.11. Clearly, Ag spheres in vacuum have a better developed LSP than Cu. The presence of an embedding medium may though change this situation: if the medium has an opportune dielectric constant, this may markedly enhance the LSP resonance by shifting it away from the interband transition region [Kre93].

3.2.4 Near zone fields on rough noble metal surfaces

Rough metal surfaces illuminated with light with frequency in the optical range behave differently from the corresponding homogeneous surfaces. The main difference consists in the fact that LSP's may be excited only in surfaces with roughness features smaller than the wavelength of the incident light. In this Section we analyze the influence of such collective excitations on the near zone (NZ) fields generated at the roughness features themselves. This is very

interesting because photoemission from rough metal surfaces is governed by the NZ field behavior, as we will see in § 3.3.
As a first approximation, let us assume the surface roughness features to be spherical particles and consider the NZ fields at their surfaces. The effect of LSP excitation on the far fields is normally expressed in terms of the extinction efficiency Q_{ext}. Given a metal particle illuminated by an incident plane wave, the scattering efficiency Q_{sca} gives a measure of the ability of the particle to extract power from the incident wave and redirect it as scattered power over all solid angles. On the other hand, the absorption efficiency Q_{abs} is a measure of the ability of the particle to absorb power from the incident wave, i.e. it represents the ratio between the absorbed and the incident power for a given geometrical cross section of the particle. The extinction efficiency is defined as:

$$Q_{ext} = Q_{abs} + Q_{sca} \,. \tag{3.20}$$

It is related to the extinction coefficient σ_{ext} through the relation:

$$Q_{ext} = \frac{\sigma_{ext}}{G} \,, \tag{3.21}$$

where G is the particle cross-sectional area projected onto a plane perpendicular to the incident beam (for example, $G = \pi R^2$ for a sphere of radius R).
From this definition it is clear that $Q_{ext} = 1$ means that all rays of the incident plane wave are either absorbed or deflected by reflection and refraction. Actually, it is often the case that $Q_{ext} > 1$. For example, $Q_{sca} > 1$ means that a small metal particle can act as a "field intensifier", i.e. the strength of the fields about the sphere can be greater than that of the incident wave. The origin of this effect can be understood in terms of a coherent superposition between the incident electromagnetic wave and the field produced by the synchronous oscillations induced in the particle electrons.
In § 3.2.2 the extinction coefficient σ_{ext} predicted by the Mie theory within the quasi-static approximation for a spherical metal particle was given. It was pointed out that the LSP resonance occurs whenever σ_{ext} has a maximum. This simply means that the enhancement of the far-fields is maximal at LSP resonance.
To give a measure of the intensity of the NZ electric field at the surface of a metallic sphere of radius R, Messinger *et al.* [Mes81] introduced the quantity Q_{NZ}, given by:

$$Q_{NZ} = \frac{r^2}{\pi R^2} \int_0^{2\pi} \int_0^{\pi} \mathbf{E_S} \cdot \mathbf{E_S^*} \sin\theta \, d\theta \, d\phi \Big|_{r=R} \,, \tag{3.22}$$

where $\mathbf{E_S}$ is the scattered electric field and r the distance from the center of the sphere. Q_{NZ} is the near-field form of Q_{sca} and decreases asymptotically to Q_{sca} in the limit $r >> R$. Q_{sca} is the most convenient quantity to measure the ability of a metal sphere to convert an incident electric field into far field scattered intensity. Analogously, Q_{NZ} gives a measure of the ability of the sphere to convert an incident electric field into NZ field intensity. As before, $Q_{NZ} > 1$ expresses an enhancement of the local NZ field, as compared with the squared field amplitude of the incoming wave.
In [Mes81] the quantities Q_{ext}, Q_{sca} and Q_{NZ} are calculated for Cu, Ag and Au spherical particles as a function of the radius R $(0 - 300\,\text{nm})$ and the wavelength of the incident light λ $(200 - 1200\,\text{nm})$. Figure 3.12 shows the extinction, far field scattering and absorption efficiencies (scale on the left) compared to the NZ field scattering efficiency (scale on the right) for Ag spheres with radius $R = 22\,\text{nm}$ and $R = 100\,\text{nm}$ immersed in water. It clearly shows that the maximum in Q_{NZ} occurs in correspondence of the maxima of Q_{sca}, Q_{abs} and Q_{ext}, i.e. in correspondence with the excitation of LSP's. For $R = 22\,\text{nm}$ (upper panel) one single maximum at $\lambda = 400\,\text{nm}$ occurs, where $Q_{NZ} \approx 1000$: this means that the **intensity**[4] of the NZ field is 1000 times larger than the electric field-intensity of the incoming wave. For $R = 100\,\text{nm}$ (lower panel) further maxima occur, which correspond to the excitation of multipole modes in the spheres. Note, however, that Q_{NZ} is actually larger than one for a wide wavelength region. This means that the excitation of LSP's is in principle not needed in order to have an enhancement of the NZ electric field. The occurrence of a LSP resonance assures that the electric NZ field assumes its maximum.
Figure 3.13 shows the extinction, far field scattering and absorption efficiencies compared with the NZ field scattering efficiency for Cu spheres with radius $R = 22\,\text{nm}$ and $R = 100\,\text{nm}$ immersed in water. For the spheres with $R = 100\,\text{nm}$ the peak of Q_{NZ} is noticeably displaced in wavelength from the Q_{ext} and Q_{sca} peaks. Thus, it is not necessary for the maximum of the NZ field enhancement to coincide with the excitation of the LSP, defined as the maximum of Q_{ext}.
The NZ field differs from the incoming plane wave and from the scattered far fields not only in its intensity, but also in its **spatial dependence** and **polarization**. In the far field scattered from a metal sphere the electric field decreases with $1/r$ (r is the distance from the center of the sphere). In the NZ field of the sphere, however, the incident plane wave is significantly distorted in order to satisfy the boundary conditions at the surface. On a perfect conductor, for example, a (static) electric field must be normal to

[4]Notice that this is defined as the squared field amplitude.

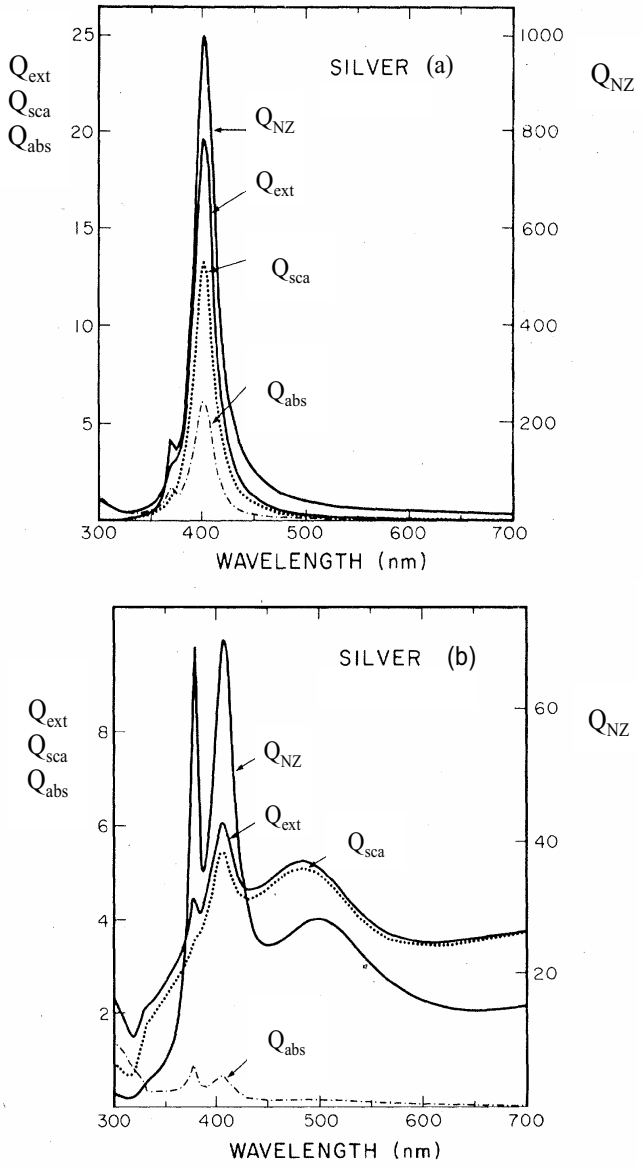

Figure 3.12: Calculated extinction, far field scattering and absorption efficiencies (scale on the left) compared with the NZ field scattering efficiency (scale on the right) for Ag spheres with radius $R = 22\,\text{nm}$ (a) and $R = 100\,\text{nm}$ (b) immersed in water, from [Mes81].

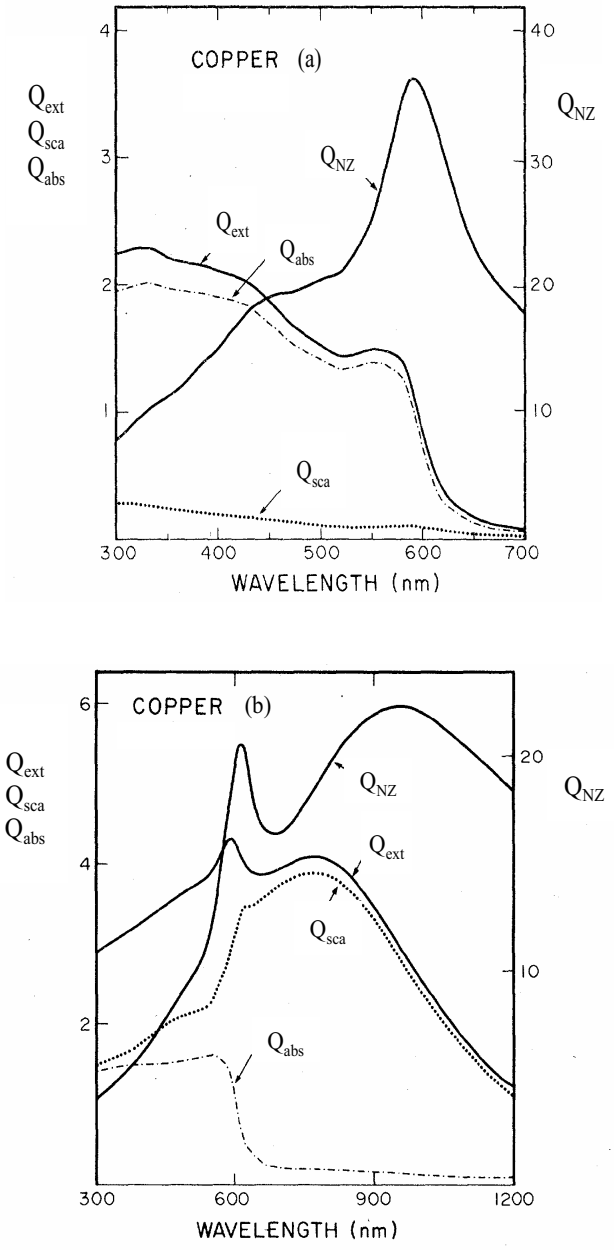

Figure 3.13: Calculated extinction, far field scattering and absorption efficiencies (scale on the left) compared with the NZ field scattering efficiency (scale on the right) for Cu spheres with radius $R = 22\,\text{nm}$ (a) and $R = 100\,\text{nm}$ (b) immersed in water, from [Mes81].

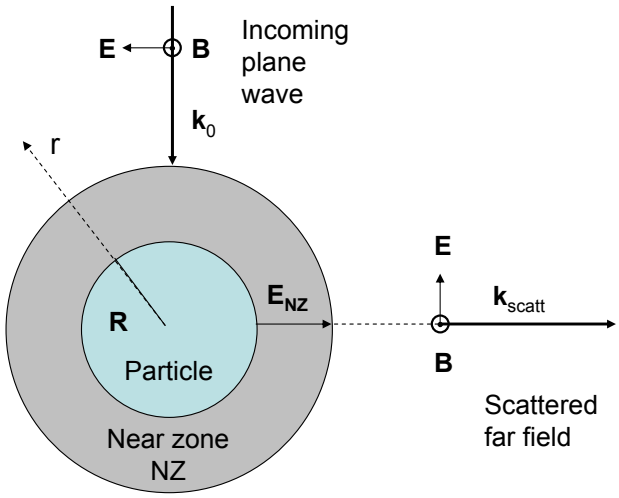

Figure 3.14: Schematic representation of the different spatial behavior of the incoming electromagnetic wave, the scattered far-field wave and the NZ field. The incoming and the scattered far-field waves are transversal waves in vacuum, and thus do not possess components of **E** and **B** along the propagation direction **k**. The gray shade indicates the NZ region, where the NZ fields arise. In the case of an ideal metallic sphere in vacuum, the (static) NZ field E_{NZ} has only the radial component E_r, which is not present in the incoming and scattered waves.

the surface, i.e. radial ($E_{NZ} \equiv E_r$). Messinger *et al.* [Mes81] have isolated the radial contribution Q_r from Q_{NZ} for Ag spheres with radius $R = 22\,\text{nm}$ and $R = 100\,\text{nm}$ immersed in water. For both sizes, Q_r shows the same dependence as Q_{NZ} on the incoming light wavelength ($300\,\text{nm} < \lambda < 700\,\text{nm}$) and constitutes more than 70% of Q_{NZ}. These results indicate that metallic spheres convert a large fraction of the plane-wave fields to E_r in the NZ field of the sphere. It further implies that the polarization state of the NZ field significantly differs from the one of the incoming and far-field scattered waves, being transversal waves in vacuum.

Also in real experiments, the NZ fields contain radial components which are not present in the far fields (see Figure 3.14). This results in fields which increase faster than r^{-1} as one moves from the far field to the surface of the sphere, i.e. with a stronger spatial dependence than the scattered far-field wave. This fact explains why normally Q_{NZ} is larger than Q_{sca}: the

integrated NZ field intensity contains these additional field components which appear only in the NZ field region.
It is now worthwhile to notice that the presented approach is quite general, and allows to evaluate the NZ field-intensity enhancement for a large interval of sphere radii, namely from 0 to 300 nm[5]. One of the more interesting results is actually the fact that for relatively large values of R, Q_{NZ} is enhanced (i.e. > 1) over a wide spectral range ($300\,\text{nm} < \lambda < 700\,\text{nm}$ in Figures 3.12 (b) and 3.13 (b)). This is most probably due to the increasing importance of retardation effects for larger particles.
On the other hand, for particle radii within the quasi-static regime, the LSP resonance and its width do not depend on the particle size. Within this approximation it is possible to give an estimation of the NZ field enhancement, by assuming the NZ field to be maximal whenever a LSP is excited. This approximative ansatz is treated, for example, by Shalaev [Sha02]. In particular, the author estimates the ratio between the LSP **resonant** NZ field amplitude at the surface of a spherical metal particle E_1 and the field amplitude E_0 of the incoming wave by:

$$\frac{E_1}{E_0} \sim Q_f \sim \frac{4\pi}{V}\alpha(\omega_{LSP}) \ , \tag{3.23}$$

where Q_f is the quality factor of the LSP resonance, V is the sphere volume and $\alpha(\omega_{LSP})$ the value of the polarizability at the resonance frequency ω_{LSP}. Equation (3.23) may be further simplified by calculating the polarizability of a metal sphere immersed in an external field and evaluating this quantity when the LSP resonance occurs (equation (3.14)).
For noble metal spheres with a radius between 5 and 50 nm, Shalaev reports values of Q_f in the order of 10 to 100. In particular, the maximum value $Q_f \approx 50$ is reported for Ag spheres at the resonance wavelength $\lambda_{LSP} = 400\,\text{nm}$.
Up to now we described the NZ field behavior at the surface of metal spheres. To summarize, the NZ field is enhanced with respect to the incoming wave and possesses a different polarization and a stronger spatial dependence. An accurate solution for the NZ fields of LSP-resonant particles of arbitrary shape is still a theoretical challenge. Analytical solutions for the NZ fields are known only for particles with a very simple shape, like that of a sphere or an ellipsoid [Bar83]. The NZ field enhancement may be quantified in the easier case of small spheres (i.e. , when the quasi-static approximation holds) through the quality factor $Q_f(\omega_{LSP})$ of the LSP resonance.

[5]Note, however, that such a macroscopic approach can be used for particles with linear dimensions down to a minimum of 2 nm [Kot01]. For smaller particles, quantum size effects must be taken into account [Bra93].

An ideal surface consisting of small metal spheres far enough spaced not to interact with each other, and not interacting with the substrate, would be as well characterized by the resonance wavelength ω_{LSP} and the corresponding quality factor $Q_f(\omega_{LSP})$. On the other hand, as explained in § 3.2.2, the dipolar interaction between particles and with the substrate shifts the resonance value and broadens its width. Clearly, the description of the optical response of a physically rough surface is rather complicated. A possible approach, described in [Sha02, Sha00], is to model the surface roughness features as small polarizable elements of a fractal. It is known [Mos85] that metal surfaces formed by condensing an atomic beam onto a low temperature substrate have a fractal character. Figure 3.15 shows a picture of a typical fractal aggregate of Ag colloidal particles deposited on a plane, obtained with an electron microscope. Note that voids are present at all scales, from the minimum (about the size of a single particle) to the maximum (about the size of the whole cluster). The size of an individual particle is about 10 nm, whereas the size of the cluster is about 1 μm.

Figure 3.16 shows the calculated field distributions at the surface of such an

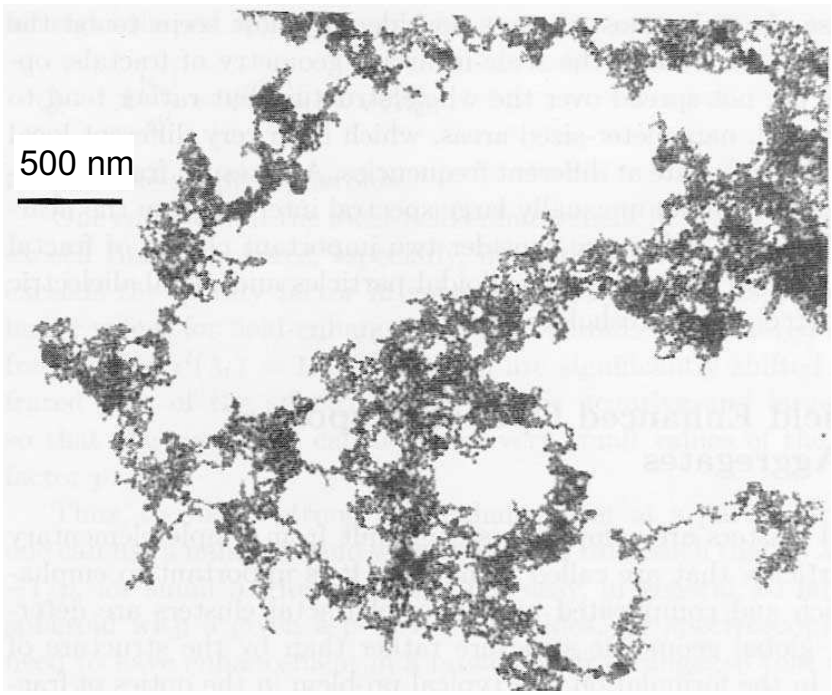

Figure 3.15: Electron micrograph of a fractal Ag colloidal aggregate, from [Sha00].

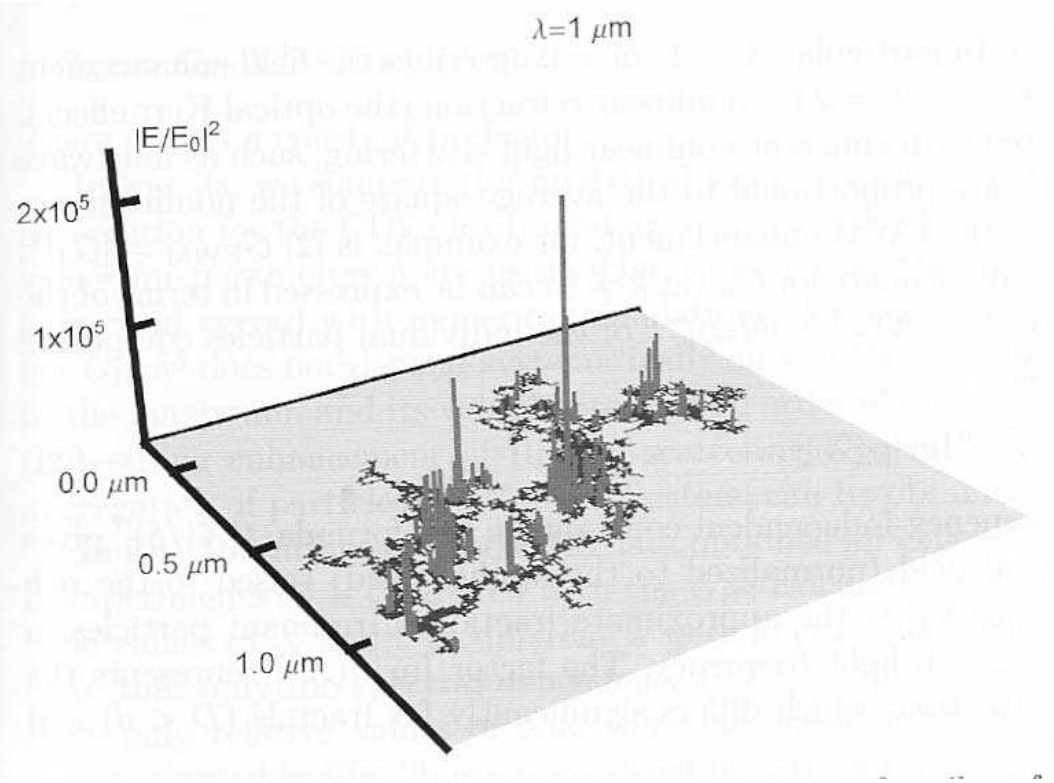

Figure 3.16: Calculated field distributions at a wavelength of 1 μm on the surface of an Ag fractal aggregate deposited on the plane. Note the occurrence of *hot-spots*, from [Sha00].

Ag fractal aggregate deposited on a plane, excited by light with wavelength $\lambda = 1\,\mu$m. Roughly speaking, such fractal structures behave as a collection of non-interacting prolate nanospheroids, with all possible values of the aspect ratio. The calculations show that the largest fields are extremely localized: the local field intensity in such *hot-spots* can exceed the applied field up to 10^5, while the average enhancement is of the order of 10^2 to 10^3. A special feature of fractals is that they actually provide enhancement within a large spectral interval, typically from the near UV to the far infrared. This is a direct consequence of two factors, namely that optical excitations tend to be localized in fractals, and that in a fractal there is a large variety of different local geometry structures which resonate at different frequencies.
If one replaces a typical fractal structure with a $3D$ compact structure of particles, the above mentioned localization of the optical excitation does not take place. Instead, in most normal modes excited in the structure, every

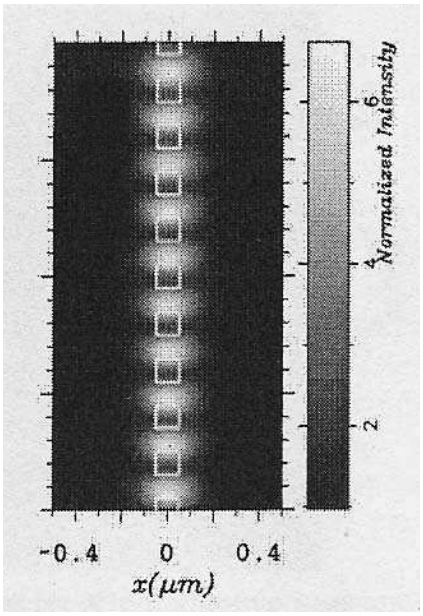

Figure 3.17: Numerical simulation of the behavior of an array of $100 \times 100 \times 40\,\mathrm{nm}^3$ Au particles illuminated with light with wavelength $\lambda = 633\,\mathrm{nm}$. The white squares indicate the position of the Au nanoparticles. The bright spots corresponding to high NZ field values are located not on top of the particles but localized between them, revealing the excitation of a collective mode in the chain, from [Kre99].

particle contributes to the excitation and all the resonances depend on the shape of the object and lie typically within a narrow spectral interval. An example of this behavior is given in [Kre99]. There, Krenn *et al.* studied the NZ field behavior of an array of $100 \times 100 \times 40\,\mathrm{nm}^3$ Au particles spaced by 100 nm and deposited on an ITO substrate. The NZ field was measured using a photon scanning tunnelling microscope. The main result obtained is that the NZ field is not maximum on the top of the single Au particles, but is squeezed and localized between them (see Figure 3.17). This reveals the excitation of an electromagnetic collective eigenmode in the chain, which of course depends on the shape of the analyzed structure. This mode is set up by dipolar coupling between the individual particles and was observed at the same wavelength of the LSP resonance of a single particle.
In recent years, many studies of the electromagnetic interaction among metal nanoparticles of diameter D prepared in ordered arrays with spacing d have been presented [Mai02, Mai03, Lam00, Lin01]. As already anticipated, such arrays are characterized by collective dipole resonances lying in a narrow

spectral range. If $d \geq \lambda$, the resonance frequencies and their lifetime are influenced predominantly by far field dipolar interactions with a d^{-1} distance dependence. On the other hand, for closely spaced nanoparticles ($d < \lambda$) the dominant interaction is given by the high NZ fields and shows a d^{-3} distance dependence.

3.3 Theory of two-photon photoemission

As already pointed out, two-photon photoemission (2PPE) is the dominant electron emission mechanism in the experiments performed with the blue laser (photon energy $\hbar\omega \approx 3\,\text{eV}$) on Cu and Ag samples (work function range: $4.2\,\text{eV} \leq \phi_m \leq 5\,\text{eV}$). In this section we analyze the main differences between 2PPE from smooth and rough metal surfaces.
According to the three-step model for photoemission [Ber64b], the electron energy distribution curves measured in a spectroscopy experiment are determined by the product of three factors:

- the electron distribution probability $P(E,\omega)$ per unit time and volume, following photon excitation. The general expression for the distribution probability function following 2PPE can be written as a sum of two terms [Sha96]:

$$P^{(2p)}(E,\omega) = P^{(c)}(E,\omega) + P^{(s)}(E,\omega)\ , \tag{3.24}$$

  where the first term is due to two sequential (cascade) excitations, while the second is due to simultaneous, i.e. true two-photon excitations.

  Basically, **simultaneous excitations** are coherent, i.e. they do not populate intermediate hot electron states (see § 3.4 and § 3.5). In a coherent process the electrons never populate the intermediate state, thus the photoemission can proceed through virtual states, which can always satisfy the symmetry, energy, and momentum constraints imposed by the detection geometry and energy bandpass [Oga96]. On the contrary, **cascade processes** are incoherent and proceed through the creation of a hot electron population, which evolves in time due to elastic and inelastic collisions before a second photon is absorbed.

- The electron transmission function $t(E)$, that describes the transport of the optically excited electrons towards the surface.

- The electron escape function $T(E)$, that takes into account that the electrons, before escaping into vacuum, have to travel through the surface barrier. This is possible only if they posses a component k_n of the

total momentum $\mathbf{k}$ along the surface normal which is greater than the critical value $k_c \propto (E_F + \phi_m)$.

From the considerations in § 3.2, it is clear that the presence of roughness features on the surface drastically influences the emission of electrons from the surface itself. In fact, on homogeneous surfaces the excitation of SPW's is prevented at all optical frequencies, while the presence of small surface inhomogeneities allows the excitation of LSP's. In turn, the excitation of LSP's causes an enhancement of the NZ field intensity and a modification of its spatial dependence and polarization that directly influence the probability $P(E, \omega)$.
In the following we present a theoretical description of 2PPE in the threshold region from smooth and rough surfaces that is based on [Sha96]. This approach allows to find expressions for the quantities $P^{(2p)}(E, \omega)$, $t(E)$, and $T(E)$. The subscript S will be used to label the quantities calculated for *smooth surfaces*, while R stays for *rough surfaces*. Here we can anticipate that:

- in smooth films, direct (i.e. k-conserving) transitions give the dominant contribution to the two-photon excitation probability $P_S^{(2p)}(E, \omega)$, while in rough surfaces excited with photons whose energy range lies in the LSP resonance (or close to it), the most important contribution to $P_R^{(2p)}(E, \omega)$ comes from indirect transitions induced by the strong spatial dependence of the NZ fields associated with the LSP's. These high NZ fields lead to enhanced photoemission which is alternatively interpreted as non-radiative decay of the LSP into a one-electron excitation.

- The transmission function in the threshold region is approximately the same for smooth and rough surfaces [Sha96].

- The escape function from a rough film $T_R(E)$ is larger than $T_S(E)$.

We now give quantitative expressions for $P_S^{(2p)}(E, \omega)$, $P_R^{(2p)}(E, \omega)$, $T_R(E)$ and $T_S(E)$ together with qualitative arguments to explain their differences.

3.3.1 Two-photon photoemission from smooth films

The excitation probability $P_S^{(2p)}$. The effects of an external electromagnetic field on the electrons in a metal can be taken into account by introducing in the Hamiltonian the operator:

$$\tilde{V} = \frac{e}{2mc}[\tilde{\mathbf{A}} \cdot \mathbf{p} + \mathbf{p} \cdot \tilde{\mathbf{A}}] \ , \tag{3.25}$$

where $\mathbf{A}$ is the vector potential, $\mathbf{p}$ the linear momentum operator and the tilde indicates the periodic time dependence of the fields. The near threshold region is defined by the condition:

$$|\hbar\omega^{'} - 2V_G| \ll \hbar\omega^{'} \tag{3.26}$$

where $\hbar\omega^{'} = 2\hbar\omega$ is the total photon energy and V_G is the energy gap between two conduction bands.
In the present experiments, the photon momentum of the incident light q is negligible with respect to the electron momentum k. In fact for $\hbar\omega^{'} \approx 6\,\mathrm{eV}$ one has $q \approx 3 \cdot 10^5\,\mathrm{cm}^{-1} \ll k_F$, where k_F is the momentum of electrons at the Fermi level that is of the order of $10^8\,\mathrm{cm}^{-1}$ for most metals. This implies that photoemission is dominated by direct transitions ($\Delta k = 0$). Moreover, it allows to work in the so-called *dipole approximation*, where the spatial variation of the exciting field in (3.25) is ignored.
Figures 3.18 and 3.19 show the calculated band structures of Ag and Cu, respectively (from [Ber64a]). They show clearly that with a photon energy of $\hbar\omega \approx 3\,\mathrm{eV}$, no direct transitions are possible in both metals from initial states with energy E_i (lying in the light blue shadowed area) to real intermediate states with energy $E_m = E_i + \hbar\omega$ (lying in the gray shadowed region). Thus, the excitation in smooth surfaces or films will occur via virtual (non resonant) intermediate states with the same momentum as the initial one. This implies that the cascade term $P^{(c)}(E,\omega) = 0$ in (3.24). In this case we can write [Sha96]:

$$\begin{aligned} P_S^{(2p)} &= P_S^{(2p)(s)}(E,\omega) = \\ &= \frac{2\pi}{v\hbar}\sum_{if}\left|\sum_m \frac{V_{im}V_{mf}}{P_{im}}\right|^2 \delta(E_f - E_i - 2\hbar\omega)\delta(E - E_f)\ , \end{aligned} \tag{3.27}$$

where v is the sample volume, V is the operator in (3.25) without spatial dependence, $P_{im} = \hbar\Gamma_{im} + i[\hbar\omega - E_m + E_i]$ and $\mathbf{\Gamma}$ is the relaxation operator. Since we are working in the dipole approximation, we can write:

$$\left|\sum_m \frac{V_{im}V_{mf}}{P_{im}}\right|^2 \propto I^2(\omega)\left|\sum_m \frac{\mathbf{e}\cdot\mathbf{R}_{im}\mathbf{e}\cdot\mathbf{R}_{mf}}{P_{im}}\right|^2 \tag{3.28}$$

where $\mathbf{R}_{jk} = \langle j|\mathbf{r}|k\rangle$ is the dipole matrix element of the respective transition, and $I(\omega)$ is the intensity of the light wave with polarization vector $\mathbf{e}$ and photon energy $\hbar\omega$.
Note that for resonant transitions it holds ($\Re$ denoting the real part):

$$\Re(P_{mi}^{-1}) \approx \delta(E_m - E_i - \hbar\omega)\ . \tag{3.29}$$

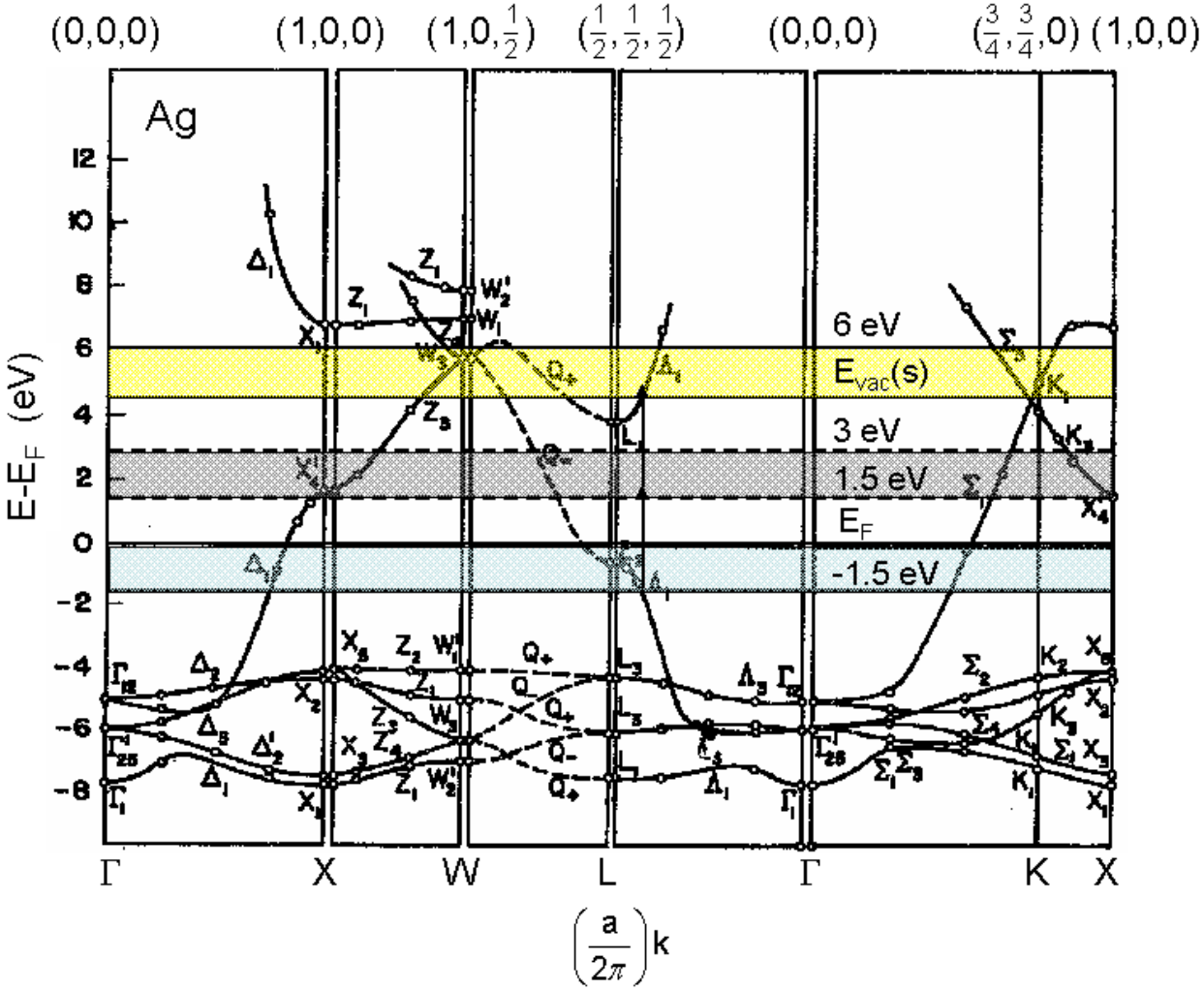

Figure 3.18: Calculated band structure of Ag, from [Ber64a]. For the vacuum level of the sample it was assumed $E_{vac}(s) = 4.5\,\text{eV}$. The light blue shaded area indicates the region below E_F corresponding to electrons which may be photoemitted after absorption of two photons with energy $\hbar\omega = 3\,\text{eV}$. The gray shaded area between 1.5 eV and 3 eV above E_F shows the energy interval corresponding to the intermediate states. The yellow shaded area shows the energy interval of the photoemitted electrons in vacuum. Clearly, there are no direct transitions ($\Delta k = 0$) that can proceed through real intermediate states. The two plotted arrows show one possible (intraband) direct transition proceeding through a virtual intermediate state.

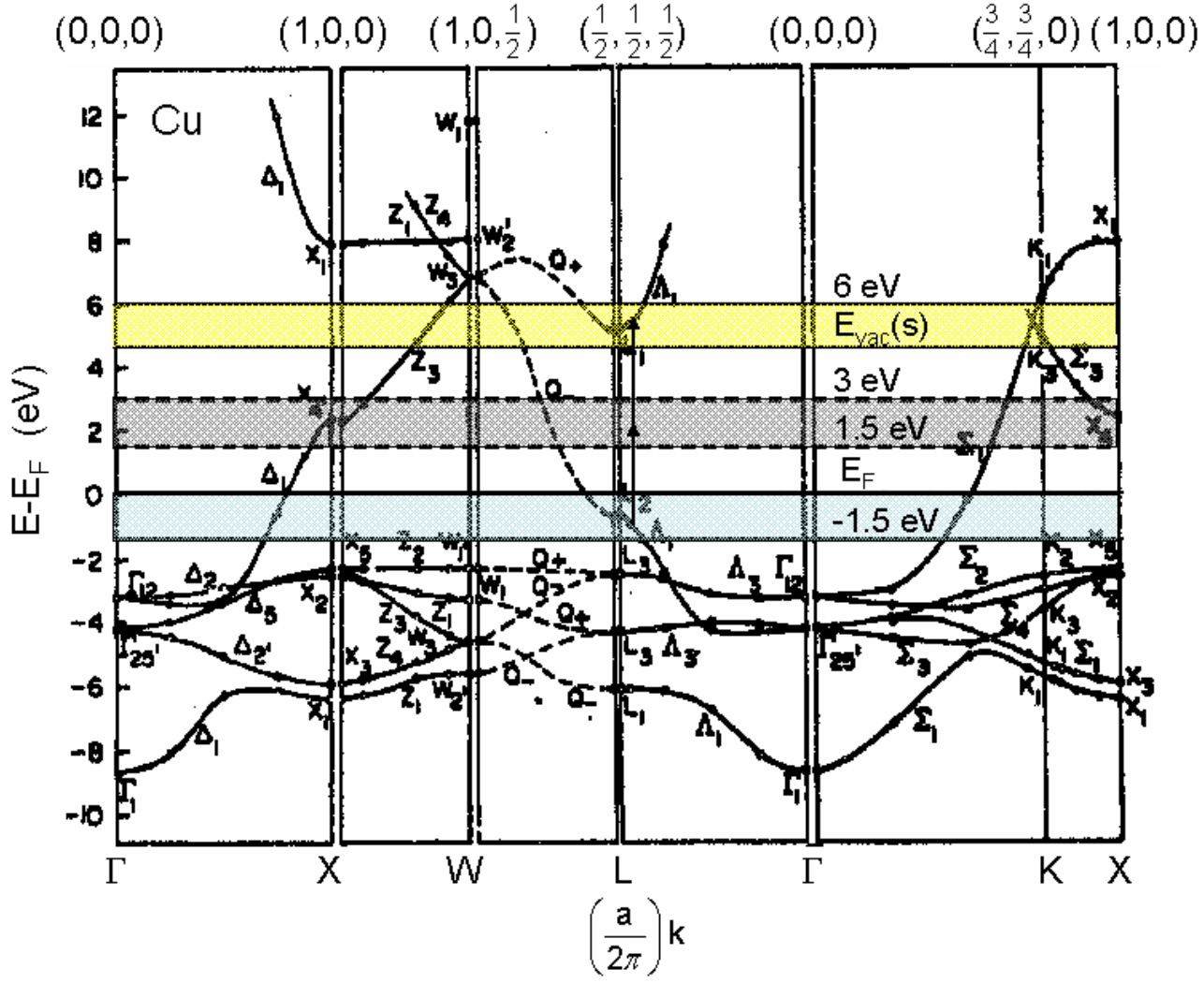

Figure 3.19: Calculated band structure of Cu, from [Ber64a]. As in Figure 3.18, it was assumed $E_{vac}(s) = 4.5\,\text{eV}$. The shaded areas have the same meaning as in Figure 3.18. The band structures of Cu and Ag are actually very similar, apart from the position of the filled d-bands, which in Ag are approximately 4 eV below E_F, while for Cu approximately 2 eV. With a photon energy of $\hbar\omega = 3\,\text{eV}$, also in Cu it is clear that direct transitions ($\Delta k = 0$) can not proceed through real intermediate states. The two plotted arrows show one possible (intraband) direct transition proceeding through a virtual intermediate state.

On the other hand, for virtual, non resonant transitions it is:

$$P_{im} \approx -\hbar\omega \ . \tag{3.30}$$

To summarize, from (3.27) together with (3.28), (3.29) and (3.30) one has:

- the probability $P_S^{(2p)}$ is proportional to the squared intensity of the laser beam.
- a simultaneous two-photon transition can be interpreted as a two-step process $|i\rangle \rightarrow |m\rangle \rightarrow |f\rangle$ through the virtual intermediate level $|m\rangle$. If the virtual level is close to a real state of the solid, the resulting transition probability is extremely enhanced: mathematically, this is given from the delta factor in (3.29). With the photon energy $\hbar\omega \approx 3\,\mathrm{eV}$ this is not the case in silver and copper, where (3.30) holds.
- the matrix elements $\mathbf{e}\cdot\mathbf{R}_{im}$ and $\mathbf{e}\cdot\mathbf{R}_{mf}$ depend on the polarization of the incoming light.

The escape function $T_S(E)$. The escape function from smooth surfaces can be approximated by the form [Cad78]:

$$T_S(E) = \frac{1}{2}\left[1 - \left(\frac{E_F + \phi_m}{E + \hbar\omega'}\right)^{1/2}\right] \ . \tag{3.31}$$

Tho total photoemission yield $J_S^{(2p)}$. The total photoemission yield $J_S^{(2p)}$, defined as the number of photoelectrons escaping per unit time through a surface unit area is given by:

$$\begin{aligned} J_S^{(2p)} &= (R_s/2)P_S^{(2p)}t\int_{E_F+\phi_m-\hbar\omega'}^{E_F} T_S(E)dE \\ &\equiv (R_s/2)tP_S^{(2p)}T_S \ . \end{aligned} \tag{3.32}$$

3.3.2 Two-photon photoemission from rough surfaces

The excitation probability $P_R^{(2p)}$. As underlined in § 3.2.4, the excitation of LSP's in the roughness features of a surface produces enhanced NZ fields (see also [Mar91, Mar96]). In [Sha96] the dipolar NZ field close to a surface roughness is written as:

$$E_\gamma^{(NZ)} = E_{\beta'}^{(0)} r^{-3}(\delta_{\gamma\beta} - 3n_\gamma n_\beta)\alpha_{\beta\beta'} \ . \tag{3.33}$$

Here the indices γ, β and β' are used to indicate a generic cartesian component of the respective vectors, $\alpha_{\beta,\beta'}$ is the (β,β') component of the polarizability tensor of the roughness feature and $\delta_{\alpha,\beta}$ is the three dimensional identity matrix. Moreover, $\mathbf{r}$ is the position vector with origin at the center of the roughness feature and $\mathbf{n} = \mathbf{r}/r$. To obtain (3.33), the surface roughness features have been modelled as small[6] polarizable elements of a fractal. The strong spatial dependence ($\propto r^{-3}$) in (3.33) includes Fourier components with high values of $\mathbf{q}^{(NZ)}$ that can be comparable with the electron momentum $\mathbf{k}$. This breaks translational symmetry and, as a consequence, eliminates the momentum conservation requirement valid for optical transitions in smooth metal surfaces [Plu82]. The operator describing the interaction of an electron with NZ photons (assuming only dipolar excitations in the roughnesses) can be written as [Sha96]:

$$V_R \approx (e\hbar/m\omega)E^{(NZ)}\nabla \ , \tag{3.34}$$

with

$$E^{(NZ)} \approx (\alpha/r^3)E^{(0)} \ . \tag{3.35}$$

The electron distribution probability following two-photon excitation of a rough surface reads:

$$\begin{aligned} P_R^{(2p)} &= P_R^{(2p)(c)} + P_R^{(2p)(s)} = \\ &= \left\langle \frac{2\pi^2}{v\hbar} \sum_{imf} \left[\frac{2}{\hbar\Gamma_{mm}} + \pi \sum_{m'} \left(\frac{V_{im'}V_{m'f}}{V_{im}V_{mf}} \right) \delta(E_{m'} - E_i - \hbar\omega) \right] \right. \\ &\quad \times (V_{im}V_{mf})^2 \delta(E_m - E_i - \hbar\omega) \\ &\quad \left. \times \delta(E_f - E_i - 2\hbar\omega)\delta(E - E_f) \right\rangle \ . \end{aligned} \tag{3.36}$$

The angular brackets indicate averaging over the rough surface and imply the summation over all the roughness features. The term $P_R^{(2p)(c)}$ takes into account the contribution to two-photon excitation from two-step cascade processes. They come into play because of the allowed indirect transitions ($\Delta k \neq 0$), which proceed through **resonant** excitation of intermediate **real states**, as depicted in Figure 3.20 for the case of Ag. The band structure presented in Figure 3.20 is the calculated band structure for bulk Ag [Ber64a]. It is known that surface roughnesses with linear dimensions $R_0 > 2\,\mathrm{nm}$ may be treated in the so called *small solid approach* where a bulk-like description

[6] With *small* we mean here that their linear dimensions are smaller than the photon wavelength.

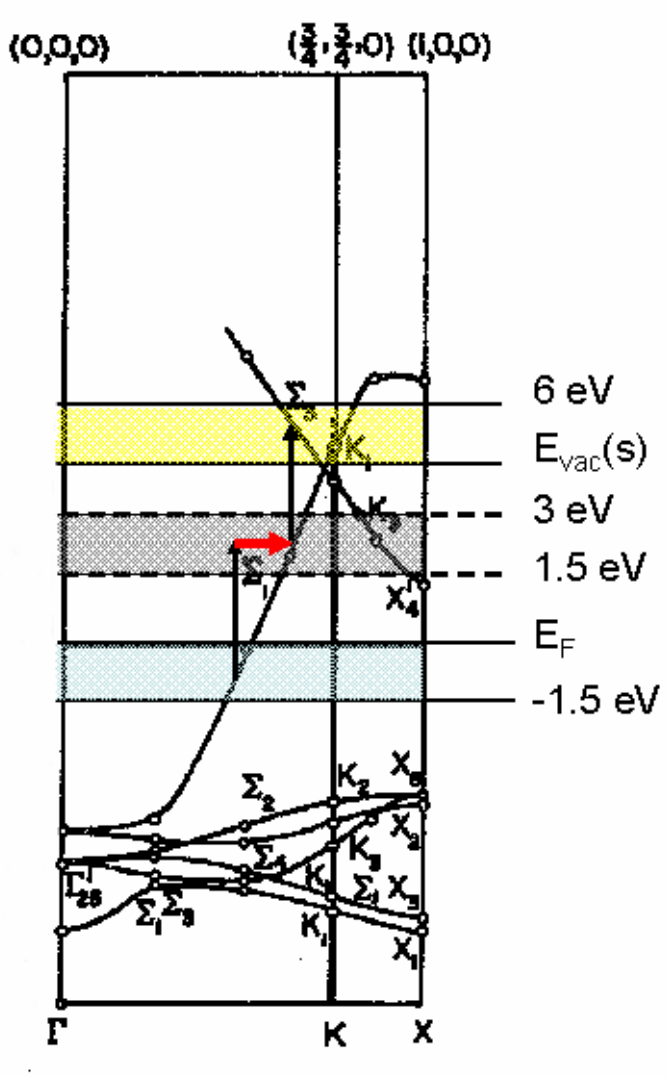

Figure 3.20: Band structure of bulk Ag along $\Gamma - K - X$, from [Ber64a]. The black arrows indicate direct transitions ($\Delta k = 0$) excited by the photon energy $\hbar\omega = 3\,\mathrm{eV}$. The red (horizontal) arrow indicates a change in the electron momentum $\Delta k \neq 0$ that is allowed in two-photon transitions in rough surfaces, due to the strong spatial dependence ($\propto r^{-3}$) of the NZ field[Sha96]. The two-photon transition shown in the figure is an indirect transition which proceeds through a real intermediate state. The intermediate state may relax before the second photon is absorbed.

is used [Voi01]. This is certainly valid for our nanoparticles, that are at least one order of magnitude larger.
The enhancement of the two-photon excitation probability in rough films is given by the term:

$$\frac{P_R^{(2p)}}{P_S^{(2p)}} \approx f(R_s)Q_f^3(R_s)\left(\frac{a}{R_s}\right)^2\left[\frac{2V_G}{\hbar\Gamma_{mm}}+\left(\frac{R_s}{a}\right)^3\right] , \tag{3.37}$$

where R_s is the light penetration depth, Q_f the quality factor of the dipolar LSP resonance, f is the volume fraction filled by roughness features, and a is the lattice constant. The main assumption used to obtain (3.37) is that the roughness size distribution $\rho(R_0)$ has the form:

$$\rho(R_0) \propto R_0^{-d} \tag{3.38}$$

where the index d is connected to the fractal dimension of the rough surface, and $R_{min} < R_0 < R_{max}$ is the size range of the roughness features. Averaging in (3.36) over the rough surface, i.e. over the random position of the polarizable roughness features and their sizes, brings to expression (3.37). Here it is clear that the main contribution to the photoemission signal is given by the roughness features with size $R_0 \approx R_s$[7]. For $R_0 \approx R_s$, Q_f assumes its maximum value $Q_f(R_s)$. This also explains the dependence of f on R_s. In particular it holds:

$$f(R_s) = \frac{1}{v}\int_{R_{min}}^{R_s} \rho(R_0)R_0^3 dR_0 , \tag{3.39}$$

with v the considered volume.
Let us now make some important observations about (3.37):

- the product fQ_f^3 expresses the enhancement of the excitation probability due to the high intensity of the NZ fields. In particular, we recall from § 3.2.4 that the quantity Q_f is proportional to the local field enhancement at the surface roughness:

$$Q_f \propto \frac{E_1}{E_0} , \tag{3.40}$$

  where E_1 is the local field at the surface and E_0 the electric field of the incoming wave. The approximation used to obtain (3.37) is valid when the excitation of the roughness features is homogeneous, i.e. when $R_0 \lesssim R_s$. With increasing R_0, Q_f drops. As anticipated, the maximum value of Q_f is reached at $R_0 \approx R_s$.

[7]For the light penetration depth R_s, see Appendix D.

- the term $(a/R_s)^2$ originates from the Fourier decomposition of the spatial term r^{-3} in (3.33). It gives the fraction of spatial harmonics with $\Delta k \approx a^{-1}$ that result in resonant nonvertical transitions;

- the term in square brackets normally exceeds the first, and gives the number of indirect transitions that contribute to the excitation. Note, in particular, the presence of the factor $1/\Gamma_{mm}$ that arises from $P_R^{(2p)(c)}$. It is proportional to the lifetime τ_{mm} of the intermediate state $|m\rangle$ through which the two-photon cascade excitation proceeds.

To summarize, the two-photon excitation probability from rough surfaces is enhanced both by the high values of the NZ fields and by their strong spatial dependence, which is actually responsible for indirect electron transitions, which may be neglected in smooth films.
The description of two-photon excitation as a two-step process, where the first photon creates a non-equilibrium distribution which is probed by the second one, is justified whenever the sum frequency of the two photons is far away from ω_{LSP} [Tim04]. At the present experimental conditions ($2\hbar\omega \approx 6\,\mathrm{eV}$) this is the case, since $\hbar\omega_{LSP}$ for Ag and Cu nanoparticles lies between 2 eV and 4 eV.

The escape function $T_R(E)$. In Appendix C we give an analytical expression for the escape function $T_R(E)$ and show that in the threshold region it holds $T_S < T_R$. Here we give a qualitative explanation for this behavior that can be divided into two main points.

- In order to escape from the metal to the vacuum, the component of the total electron momentum $\mathbf{k}$ along the surface normal (k_n) must be larger than a critical value $k_{n,c}$, given by:

$$k_{n,c}^2 = \frac{2m}{\hbar^2}(E_F + \phi_m) \ , \tag{3.41}$$

  Clearly, not for all photoexcited electrons it holds: $k_n \geq k_{n,c}$. Thus, there will be a critical angle θ_c between the surface normal and $\mathbf{k}$ inside of the metal, that discriminates between the electrons which may escape into vacuum (for $\theta \leq \theta_c$) or not (for $\theta > \theta_c$). θ_c defines the so-called escape cone, see Figure 3.21 (left). It is simply given by:

$$\sin(\theta_c) = \sqrt{\frac{k^2 - k_{n,c}^2}{k^2}} \ , \tag{3.42}$$

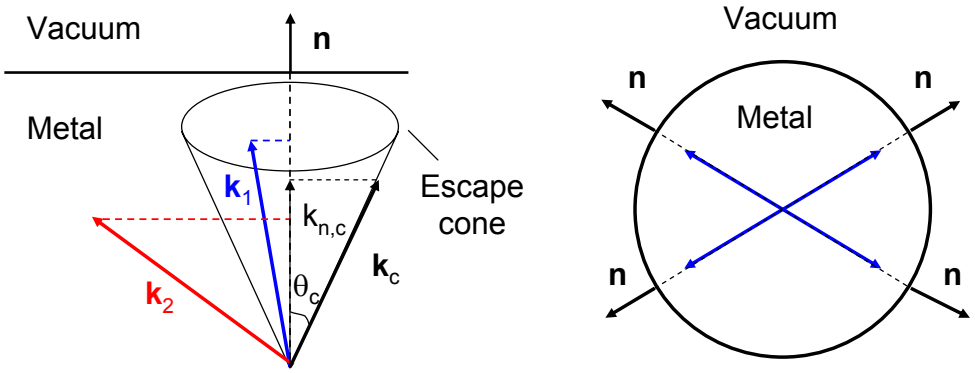

Figure 3.21: Difference in the critical angle θ_c for electron escape from a smooth planar surface and a spherical metal particle. From a planar surface (left) an electron with momentum $\mathbf{k}$ may escape into vacuum only if the component k_n of its momentum along the surface normal $\mathbf{n}$ is larger than the critical value $k_{n,c}$ given in (3.41). The blue arrow (k_1) indicates the momentum of an electron that satisfies this condition, while the red arrow (k_2) indicates an electron that cannot escape into vacuum. This electron is reflected by the surface barrier and will loose its energy through scattering with other electrons in the metal. If the photoexcitation occurs from the center region of a sphere (right), all the momentum directions are equivalent and $\theta_c = 360^\circ$.

In the case of a smooth surface, where an electron absorbs two photons with energy $\hbar\omega$, θ_c assumes the value:

$$\sin(\theta_c) = \sqrt{\frac{2\hbar\omega - \phi_m}{2\hbar\omega}} \ , \tag{3.43}$$

which gives for $\phi_m = 4.7\,\mathrm{eV}$ and $2\hbar\omega = 6\,\mathrm{eV}$ the value $\theta_c \approx 27^\circ$.

The situation is completely different if the electrons are photoexcited in a sphere. If we assume that the electrons are emitted from the center region of the sphere, it is clear that $\mathbf{k}$ is always directed along the surface normal. Thus, here we have $\theta_c = 360^\circ$, as depicted in Figure 3.21 (right).

- The model of a sphere in vacuum with electrons escaping from its center region was taken as an ideal case. It should make clear that on surface

roughnesses $\theta_{c,max}$ is in general larger than on a planar surface. Even if for geometrical reasons in surface roughnesses $\theta_{c,max} < 360^{\circ}$, there is another mechanism which increases the value of $T_R(E)$. In fact, if a photoexcited electron is not oriented along a favorite direction for photoemission, elastic collisions with the boundary of the roughness feature may redirect it so that finally $k_n \geq k_{n,c}$. This enhances the total escape probability T_R.

The total photoemission yield $J_R^{(2p)}$. In analogy with (3.32) we can define the total photoemission yield $J_R^{(2p)}$ as the number of photoelectrons escaping from a rough surface per unit time and surface area:

$$J_R^{(2p)} = (R_s/2)tP_R^{(2p)}T_R \ . \tag{3.44}$$

3.4 Two-photon photoemission in experiments

Generally, 2PPE experiments are performed by directing onto the sample two laser beams with photon energy $\hbar\omega_1$ and $\hbar\omega_2$ such that:

$$\begin{aligned} \hbar\omega_{1,2} &< \phi_m \\ \hbar\omega_1 + \hbar\omega_2 &> \phi_m \ . \end{aligned}$$

An appropriate choice of the frequencies $\omega_{1,2}$ makes it possible to study the properties of the unoccupied electronic states between E_F and $E_{vac}(s)$. There are two typical modes of data acquisition in a 2PPE experiment, which are complementary to one another (see Figure 3.22):

Two-photon photoemission spectroscopy (2PPS). Energy resolved 2PPE spectra are recorded at a particular time-delay between the pulses 1 and 2, commonly called *pump* and *probe* pulse. These spectra contain information about the electronic structure and the dynamics of electronic excited states between E_F and $E_{vac}(s)$ [Asp83, Sha78]. An appropriate tuning of the pump and probe frequencies allows to investigate, for example, the presence of Shockley surface states just above E_F and image potential states just below $E_{vac}(s)$ [Wei02].

Time resolved two-photon photoemission (TR-2PPE). Electrons are recorded at a fixed kinetic energy as a function of the time delay between pump and probe pulses. This allows to measure the time evolution of the energy levels populated by the pump pulse [Hai95]. This evolution

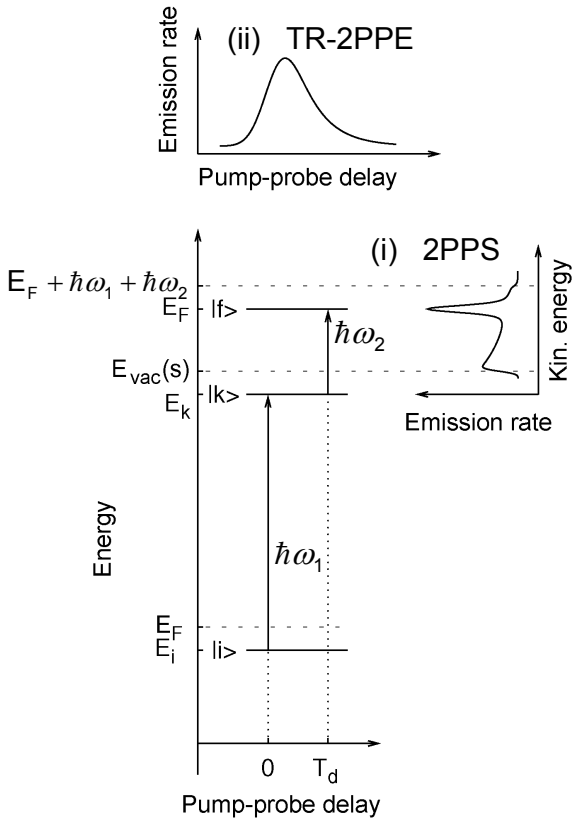

Figure 3.22: Schematic representation of a 2PPE experiment with pump photons $\hbar\omega_1$ (in this case $=3\hbar\omega_2$) and probe photons $\hbar\omega_2$ (from [Wei02]). (i) 2PPS mode: energy resolved spectra are recorded by fixed pump-probe delay; (ii) TR-2PPE mode: electrons with a fixed kinetic energy are recorded for different time delays between pump and probe pulses.

is caused by many different relaxation mechanisms. Figure 3.23 shows the typical time scales for various dynamical processes at metal surfaces [Pet97]. It makes clear that laser sources with pulse widths in the order of 10 fs or smaller allow the study of the dynamics of non-equilibrium charge carrier distributions in solids, governed by electron-electron (e-e) scattering. Note that the electron-phonon (e-p) coupling becomes relevant at longer time scales of the order of 1 ps.

Combination with spatially resolving techniques. 2PPS and TR-2PPE are used to study mainly homogeneous surfaces. Recently, a few authors [Mer00, Leh00, Sch01a, Ken01] started to study structured sam-

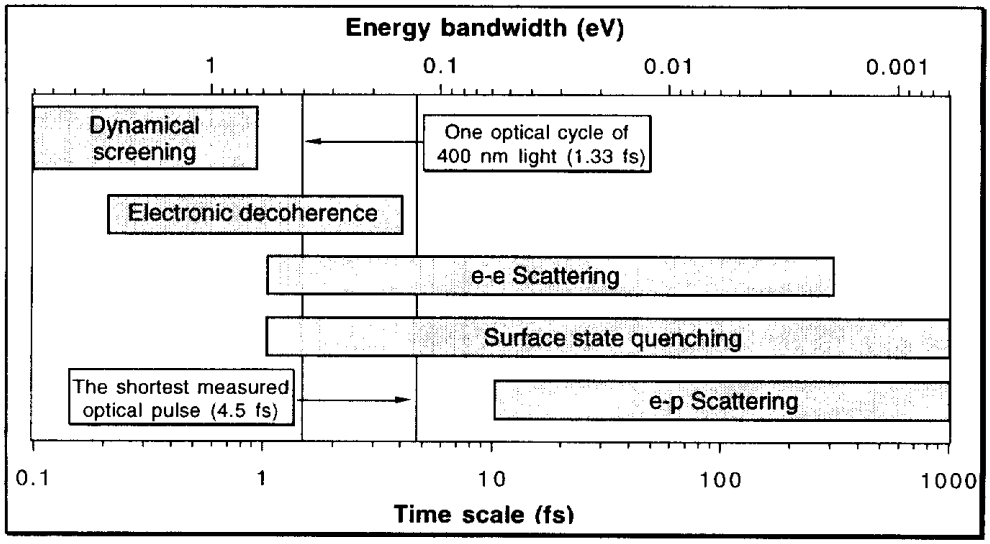

Figure 3.23: Typical time scales for various dynamical processes at metal surfaces, from [Pet97]. The energy bandwidth increases with decreasing time due to the uncertainty principle $\Delta E\ \Delta t \geq \hbar/2$.

ples, like Ag or Au nanoparticles on different substrates (highly oriented pyrolytic graphite, indium tin oxide), and managed to distinguish between sample and substrate contribution to the photoemission using different theoretical/experimental arguments. On the other hand, parallel to these experiments, Schmidt *et al.* [Sch01b, Fec02] employed a PEEM to observe the electron emission spatially resolved. The experiments revealed small regions of strongly enhanced electron emission, termed "hot-spots". In these earlier experiment it was not possible to measure the electron energy distribution spectra. Our newly developed experimental technique (TOF-spectromicroscopy, see § 2.2.2) introduces in this context a clear advantage, since it combines the lateral resolution of an imaging electron microscope (namely, the PEEM) with nPPS.

Note that in our experiments we use only one laser beam. In this case the pump and probe pulse coincide and have the same photon energy (for the blue laser $\hbar\omega \approx 3\,\mathrm{eV}$). Thus, no time delay is present, and the energy necessary to produce two-photon photoemission has to be absorbed by an electron within the duration of the laser pulse ($\leq 200\,\mathrm{fs}$).

3.5 Other possible electron emission mechanisms following optical excitation

3.5.1 Secondary-electron emission

In § 3.3 we distinguished between simultaneous and cascade 2PPE processes. Briefly, simultaneous excitations are coherent and proceed through virtual intermediate states. They constitute the main excitation mechanism in Ag and Cu homogeneous surfaces illuminated by laser light with photon energy $\hbar\omega \approx 3\,\mathrm{eV}$. On the other hand, cascade excitations play a key role in 2PPE from Ag and Cu rough surfaces. In a cascade process, real intermediate states $|i\rangle$ are occupied after the absorption of a pump photon. The population of such intermediate states gives rise to a non-equilibrium electron distribution, commonly called *hot electron* distribution. The hot electrons may subsequently relax (i.e. thermalize) via different mechanisms before the absorption of a probe photon. This relaxation produces secondary electrons which populate the states between $|i\rangle$ and E_F, and may contribute to the 2PPE spectrum.
The dominant relaxation mechanism in the femtosecond scale is given by e-e scattering (see Figure 3.23). In free-electron metals, the lifetime τ_{e-e} of an excited electron with energy E (above E_F) depends on the available phase space for scattering with electrons in the Fermi sea and is given in first approximation by [Kno96]:

$$\tau_{e-e} \simeq \tau_0 \left[\frac{E_F}{E - E_F}\right]^2 , \tag{3.45}$$

where τ_0 is a constant depending on the free electron's mass and charge and on the density of the electron gas in the metal.
Figure 3.24 shows the additional contributions to the 2PPE signal given by secondary electrons generated through e-e scattering. The Figure shows three alternative channels for secondary electron emission. An electron may loose part of its energy (through e-e scattering) after the absorption of the pump and the probe pulse, and before escaping into vacuum. This decay channel is also typical in 1PPE processes [Hen91] (where of course only one photon with enough energy is absorbed), and will be termed *true secondaries channel*. Alternatively, the inelastic scattering process may occur in the intermediate state. The two other possibilities thus constitute the *intermediate state secondaries channel*. Here, the electron has been scattered before absorbing the second photon. Owing to energy conservation, the primary electron transfers its energy loss to an electron from the Fermi sea. The

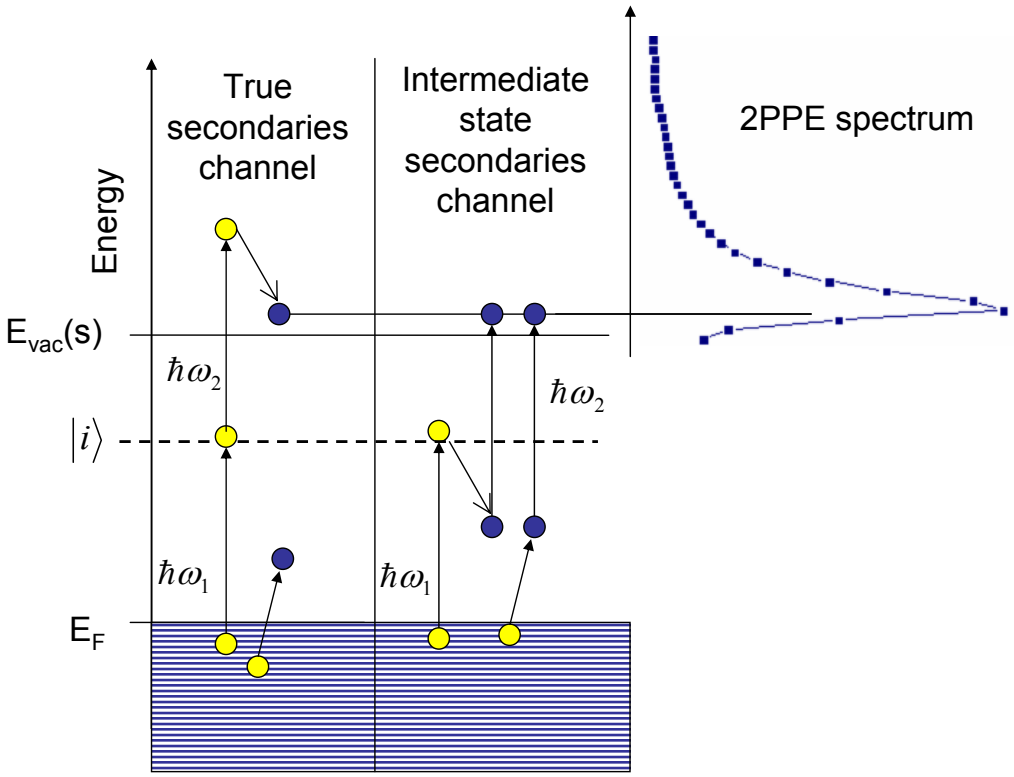

Figure 3.24: Contribution of secondary electron emission to the 2PPE signal. Two different channels are depicted. In the *true secondary channel* (left), an electron scatters with a second electron from the Fermi sea after the absorption of two photons. In the *intermediate state secondaries channel* (right), an electron excited by the first photon (pump-photon $\hbar\omega_1$) into an intermediate state $|i\rangle$, scatters inelastically with an electron from the Fermi sea. The inelastically scattered electron or the excited secondary electron absorb the second photon (probe-photon $\hbar\omega_2$) and is then photoemitted. As indicated, in both channels the main contribution from secondary electrons to the 2PPE spectrum is given at low final state energies.

second photon can subsequently lift one of the electrons above the vacuum level. In principle, both scattering partners are indistinguishable. By introducing a "spin label"to one of the electrons (e.g. by optical spin orientation [Sch86b, Sch86a]) one can experimentally gain information on the two paths of the intermediate state secondaries channel.
Figure 3.24 makes clear that in all considered cases, the main contribution from secondary electron emission is given at low final state energies closely above $E_{vac}(s)$.

3.5.2 Thermionic emission

Photoexcitation produces a nascent **nonthermal** electron distribution, which thermalizes to a Fermi-Dirac distribution through e-e scattering, before significant energy transfer can occur to the phonon bath [Pet97]. After thermalization, the electron subsystem may be characterized by a temperature T. When T is small, the tail of the energy distribution does not reach the vacuum level. In this case photoemission may occur after absorption of an additional photon by the heated electrons.
However, a sufficiently strong heating may lead to photoemission without absorption of a second photon (see Figure 3.25). This electron emission mechanism is called by some authors *thermionic emission*. It has been observed experimentally for example in [Ken01]. There, Au nanoparticles deposited on graphite have been illuminated with photon energies 1.77, 2.14 and 2.47 eV. For all of the three energies, the laser fluence was very high (1 $\mathrm{mJ{\cdot}cm^{-2}}$). Our parameters are rather comparable to those of Fann *et al.* [Fan92], where a "smearing"of the Fermi edge that can be fitted by a slightly heated electron gas (625 K at maximum) was observed in a 30 nm thick polycrystalline gold film.
The temperature of the electron gas is mainly influenced by two factors: the laser fluence and the electron-phonon coupling constant τ_{e-ph}. From this point of view, small metal particles and rough surfaces are expected to show a more pronounced heating of the electron gas with respect to a homogeneous surface. Two facts favor electron heating in nanoparticles:

- the excitation of LSP's in surface roughness features acts like a "focusing mechanism"for the incoming radiation. For the same laser fluence, the electrons of a surface roughness may absorb more photons than the electrons of a homogeneous surface of equal lateral size;

- electron-phonon coupling is much more ineffective in small metal particles than in the bulk material. Fedorovich *et al.* [Fed00] demonstrated

that this is due to the fact that the main mechanism of electron-lattice energy exchange operating in bulk materials does not work in small metal particles. In the latter case, electrons loose their energy mainly in surface collisions. The reduction of the electron-lattice energy exchange in small metal particles has been corroborated experimentally in [Gor91], where it is shown that e-ph coupling is reduced by two orders of magnitude in 10 nm radius Au particles in comparison to Au bulk material.

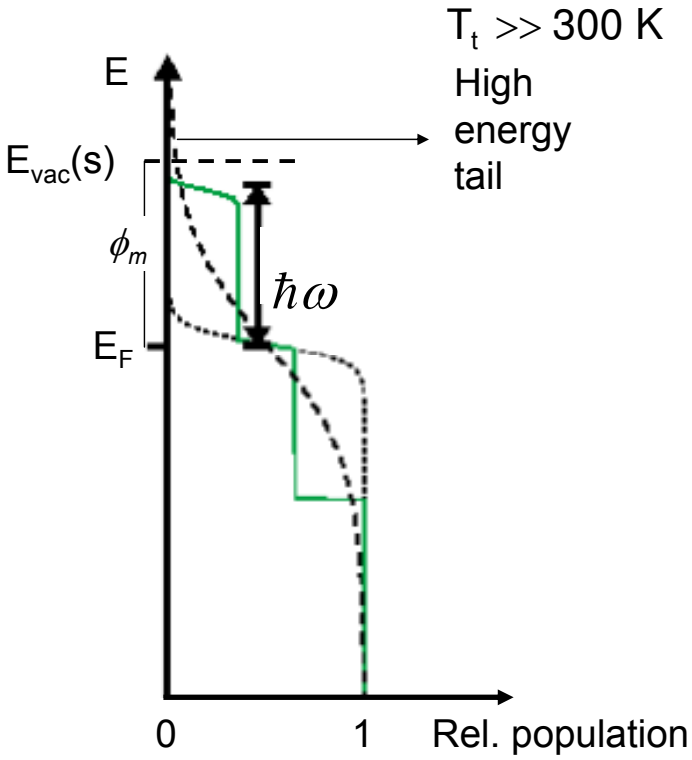

Figure 3.25: Laser heating of a confined electron gas in a nanoparticle. The dotted line reflects the electron population before the phototransition. After photoexcitation (photon energy $\hbar\omega < \phi_m$) and thermalization trough e-e scattering, the electron system can be characterized by a transient temperature T_t. If T_t is high enough, the high energy tail of the electrons may posses an energy higher than $E_{vac}(s)$. In this case, thermionic emission occurs. To illustrate the effect, both temperature are strongly exaggerated.

3.5.3 Field emission

The term field emission indicates the extraction of electrons from a solid[8] by tunnelling through the surface potential barrier. This is normally achieved by applying a very high negative potential to the metal. If the local electric field E is sufficiently high (E has to reach approximately 2 to 3 $\mathrm{V{\cdot}nm^{-1}}$), electrons may tunnel directly from the valence band through the reduced potential barrier into vacuum. For a given applied potential, the electron emission is enhanced at sharp protruding objects, where the resulting electric field is amplified. The field amplification increases with decreasing radius of curvature of the surface.

In principle, the same emission mechanism can also be obtained by illuminating the metal with sufficiently intense laser light. In this case, the electric field $\mathbf{E}$ of the incoming wave may temporarily ($\mathbf{E}$ is time- and space-dependent) lower the surface potential barrier and allow electrons to tunnel through it.

Figure 3.26 shows the energy diagram of a sample illuminated by laser light with photon energy $\hbar\omega$ and an electron detector kept at a positive bias potential U_D with respect to the sample itself. This corresponds to our experimental conditions, where U_D is the drift potential applied to the PEEM's drift tube ($U_D \approx 25\,\mathrm{V}$). The dotted line in the Figure represents the sample surface barrier in the field-free case. When a sufficiently intense laser illuminates the surface, the potential barrier is temporarily lowered. The resulting transient effective potential is represented by a continuous line. The quantitative behavior of the surface potential close to the metal/vacuum interface is shown in Figure 3.27 (from [Mül56]). In this case of cold field emission, tunnelling occurs at the Fermi energy.

In our case the lowered surface barrier may be tunnelled by electrons excited by one or two photons to a state with energy closely below $E_{vac}(s)$. This results in a wider recorded spectrum, i.e. a shift of E_k^{min} towards lower energies.

In § 3.2.4 it was pointed out that the excitation of LSP in surface roughnesses produces an enhanced NZ field in the vicinity of the roughness features themselves. The presence of sharp inhomogeneities on the surface may further amplify the local fields, so that the lowering of the potential barrier of surface roughnesses may be significantly higher than for a homogeneous surface. As the tunnelling probability increases exponentially with the width of the barrier, the experimental fingerprint of this process is a very strong dependence of E_k^{min} from the laser power, or, more precisely, from the local field amplitude at a roughness feature.

[8] In the following only field emission from metals is considered.

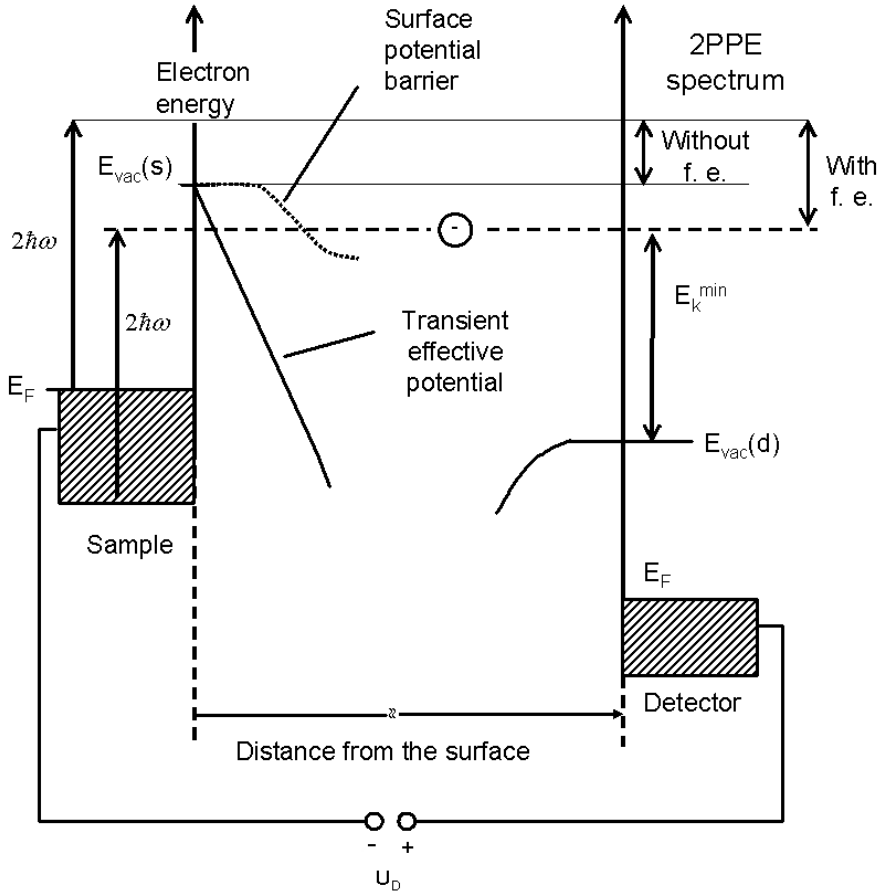

Figure 3.26: Energy diagram of a sample connected to a detector kept at a positive bias potential U_D. Dotted line: surface potential barrier (static) of the sample. Continuous line: transient effective surface potential caused by the temporary lowering of the potential barrier induced by a strong laser field. The transient effective potential may be tunnelled by electrons excited by one or two photons with energy closely below $E_{vac}(s)$ (dashed line). The fingerprint of this mechanism is a very strong dependence of E_k^{min} from the laser power. The shift of E_k^{min} towards lower energies in presence of field emission (f. e.) is shown.

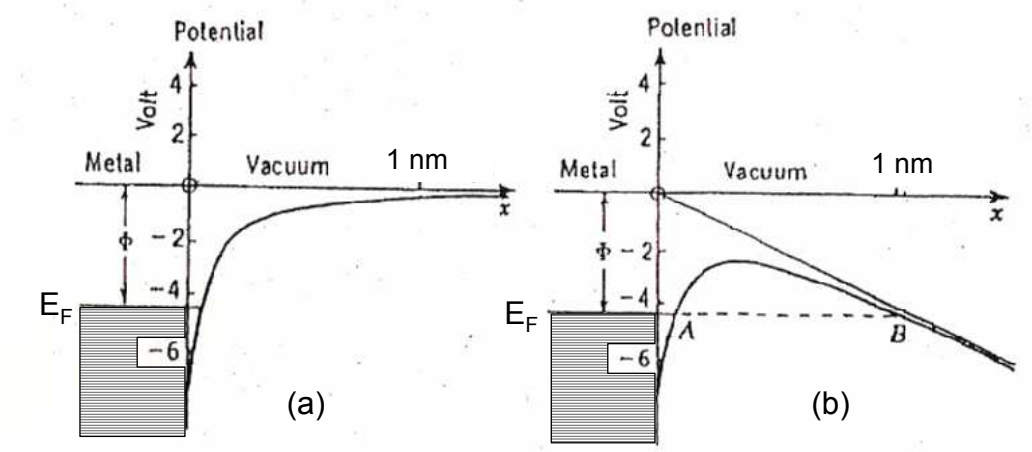

Figure 3.27: Quantitative scheme for the process of cold field emission. (a) Potential barrier of a metal surface; (b) potential above a metal surface with an external field of 4 $\mathrm{V{\cdot}nm^{-1}}$, from [Mül56].

3.6 Summary and further considerations

Small metal particles on a substrate and, similarly, metal surfaces presenting roughness features with linear dimensions smaller than the photon wavelength react to illumination with light in the optical frequency range quite different from homogeneous metal surfaces. The main reason for this different behavior is that plasmon excitation is forbidden at all frequencies on flat surfaces. The plasmon resonances of particles with dimensions down to 2 nm can be evaluated using a macroscopic approach. The complete description of the material is hereby enclosed in the complex dielectric function $\varepsilon(\omega)$. The electromagnetic scattering properties of metal nanoparticles can be described in such a way by solving Maxwell's equations.
Within this picture, originally presented by Mie [Mie08], light with frequencies in the optical range excites charge oscillations in small metal particles, which are synchronous with the incident electromagnetic field. These synchronous modes cause an enhanced optical response in the particles themselves.
The effects of such an optical enhancement are usually expressed in terms of the extinction efficiency Q_{ext} or the related scattering efficiency Q_{sca}. The latter gives a direct measure of the ability of a metal particle to extract power from the incident wave and redirect it as scattered power over all solid angles. These quantities are experimentally accessible through optical

experiments, where the measured quantities are actually the fields far away[9] from the irradiated particles (**far fields**). The fact that there are regions where $Q_{sca} > 1$ (and correspondingly $Q_{ext} > 1$) can be physically interpreted by saying that the irradiated metal particle acts as a *field intensifier*. This means that the field amplitudes close to the particle are larger than those of the incident wave. Moreover, if the light frequency is close to a characteristic frequency (eigenmode) of the confined electron system, then a resonance occurs. Such a resonance is easily identifiable as a maximum in the extinction spectra measured as a function of the light frequency. It corresponds to the modern concept of localized surface plasmons (LSP's).
The fields close to an irradiated metal particle (**near zone fields**) are distorted with respect to the far fields due to the boundary conditions at the surface of the metal particle. An accurate solution of the NZ fields of plasmon resonant particles of arbitrary shape is still a theoretical challenge. Analytical solutions for the fields are known only for particles with very simple geometries. However, one can in general conclude that the near zone fields may differ from the far field (scattered photons) and the field of the incoming laser beam in basically two points:

Intensity. In § 3.2.4 we reported theoretical calculations from Messinger *et al.* [Mes81] that allow to estimate the ability of a metallic sphere with radius R between few nm and about 300 nm to convert the field of the incident plane wave into near zone field intensity. This ability is quantified through the near zone scattering coefficient Q_{NZ}, given in (3.22). A comparison between Q_{NZ} and Q_{ext} makes clear that the maximum enhancement of the NZ field normally occurs at the LSP resonance. However, the NZ field may be substantially enhanced even far away from the LSP resonance. Moreover, it is often the case that $Q_{NZ} \gg Q_{sca} > 1$, i.e. the NZ field is more enhanced than the scattered far field, and both are larger than the field of the incoming plane wave.

Spatial dependence and polarization. In the far field scattered from a metal sphere the electric field decreases with $1/r$ (r is here the distance from the center of the sphere). On the other hand, in the NZ field of the sphere, the incident plane wave is significantly distorted in order to satisfy the boundary conditions at the surface. For example, for a perfect conductor the static electric field must be normal to the surface, i.e. radial. In turn, the NZ fields contain radial components which are not present in the far fields. This results in fields which increase

[9] Far away means here that the distance of the detector from the sample is much larger than the particle linear dimensions and the light wavelength.

faster than r^{-1} as one moves from the far field towards the surface of the sphere [Mes81]. Equation (3.33) gives an expression for the NZ field derived from Shalaev *et al.* [Sha96] for a physically rough surface modelled as a fractal distribution of small polarizable elements. In the light of the above considerations, the resulting r^{-3} dependence of the NZ field for dipolar excitations in the elements is not surprising.

In conclusion, the NZ field behavior at the surface of small metal particles can be expected to directly influence the photoemission from the particles themselves. The "experimentum crucis"to prove this theoretical conclusion is the measurement of the electron energy distribution curves for photoemission from nanoparticles and from smooth surfaces of the same material under identical experimental conditions. This is the main subject of Chapter 4.
In a semiclassical (wave-mechanical) picture the electromagnetic response of the material leads to an enhancement of the dielectric displacement vector in the nanoparticle, governed by its dielectric function. In this picture the LSP can be considered as a *photon in matter* with the special property of spatial confinement to a small volume. Suggestively, one can think that the electrons in the particle absorb one or more photons from the NZ field and are consequently photoemitted. Alternatively, the process can be interpreted as a non-radiative decay of one or more LSP's into one-electron excitations. We will retain the term photoemission in accordance with previous work in the literature. It is clear, however, that the quantum mechanical operator that describes the electron emission from a plasmon-resonant nanoparticle will considerably deviate from the common dipole operator of low-energy photoemission. The strong field gradient in the vicinity of the surface gives rise to non-vertical transitions [Sha96] and the polarization properties can be substantially different from a free electromagnetic wave. This fact leads to a violation of the symmetry selection rules in the optical transition [Hor78, Kos63]. A non-radiative decay channel for the LSP into a single electron-hole excitation will be governed by the Coulomb operator, like in an Auger transition.
Since the NZ fields at the surface of small particles differ from the plane incoming wave, one expects a marked difference between the 2PPE signal from rough and homogeneous surfaces. This difference is expressed in §3.3 in term of the ratio (3.37) between the two-photon excitation probability from a rough and a smooth surface, respectively. This quantity shows that the probability to excite a photoelectron through 2PPE is larger in rough surfaces because of the enhanced NZ field intensity (expressed through the quality factor of the LSP resonance, Q_f) and their strong spatial dependence, which allows otherwise forbidden electronic indirect transitions ($\Delta k \neq 0$) to

take place.

Chapter 4

Experimental Results and Discussion

In this Chapter we present the experimental results obtained using mainly the 2PPE TOF-Spectromicroscopy technique described in Chapter 2. The presentation is organized as follows: in § 4.1 we determine the spatial and energy resolution of the experimental technique. In § 4.2 and § 4.3 we investigate respectively the 2PPE behavior of Cu surface inhomogeneities and of Ag nanoparticle films deposited on Si(111).

The 2PPE spectra of the Cu and Ag nanoclusters reveal the same qualitative differences from the spectra of the corresponding homogeneous and clean metal surfaces. In particular, they show an enhanced photoemission yield (up to 70 times higher) and present a different overall shape, characterized by differences around the Fermi level onset and a steeper intensity increase at lower final state energies. These differences are discussed in § 4.4 in terms of the excitation of localized surface plasmons in the clusters and a resulting modification of the near-zone electromagnetic field, which in turn influences the 2PPE and its dynamics. Moreover, it is shown that a positive unit charge (photohole) resides on the clusters during the time scale relevant for the two-photon photoemission process.

In § 4.5 we discuss the effects of the laser polarization on 2PPE. In § 4.6 we present the results of an experiment which gives a direct evidence that the NZ field behavior influences 2PPE. Finally, § 4.7 deals with 3PPE from Ag nanoparticle films deposited on Si(111).

4.1 Determination of the spatial and energy resolution

We briefly recall that a measurement with the TOF-PEEM setup generates the 4D-data set $J = J(\mathrm{x,y},\tau)$, that can be analyzed with the software after the measurements. Table 2.1 shows the different possibilities for the data analysis, namely the Microspectroscopy and the Spectromicroscopy modes. Shortly:

- in the spectromicroscopy mode, energy resolved images are generated from the data. In the following we determine the spatial resolution $\tilde{\Delta}_s$ that can be achieved in this mode. This quantity depends on the selected energy/TOF interval $\Delta\tau$. Since our spectra are relatively narrow ($\approx 2\,\mathrm{eV}$), we expect this dependence to be quite weak. To support this hypothesis we evaluate $\tilde{\Delta}_s$ for different values of $\Delta\tau$;

- in the microspectroscopy mode, which is actually the mostly used mode in this work, the energy distribution curves of the electrons emitted from the area of interest $\Delta(x, y)$ are generated. In the following we determine the energy resolution $\tilde{\Delta}_E$ achieved with this modus. It should be independent from the selected area of interest $\Delta(x, y)$: this is confirmed by the experimental data.

4.1.1 Spatial resolution in the spectromicroscopy mode

To determine the spatial resolution in the spectromicroscopy mode we prepared a test sample consisting of a 130 nm thick Ag film evaporated in situ on a Si(111) substrate. The substrate was cleaned by chemical etching with HF and by heating cycles in situ followed by Ar ion sputtering.
Figure 4.1 (a) and (b) show two energy resolved TOF-PEEM images of the same region $\Delta(x, y)$ of this sample taken with s-polarized laser light. The two images are respectively generated from the energy intervals $\Delta\tau_a$ and $\Delta\tau_b$ marked in Figure 4.1 (c). Several bright spots can be seen in the images. The arrows on one of them indicate the position where the line scans of Figure 4.2 were taken (solid line from (a), dashed line from (b)).
From Figure 4.2, we derive a spatial resolution of 100 nm. The resolution was defined following the Rayleigh criterion: the FWHM of the knife-edge curve Gaussian fit derivative, which is equivalent [De 98] to the distance of the 12% and 88% intensity points marked by dots in one of the two interpolation lines shown in the Figure. Note that in the ideal case such a resolution test should be performed on a infinitely sharp feature of a perfectly flat surface.

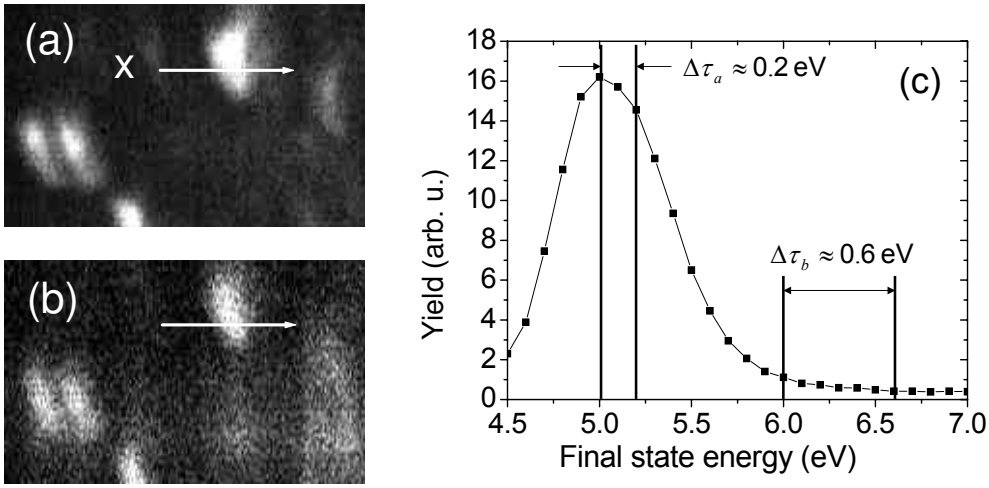

Figure 4.1: (a),(b) Energy resolved TOF-PEEM images of the Ag/Si(111) sample excited by s-polarized photons (field of view 6×4 μm^2). (c) Energy distribution curve of the electrons in the $\Delta(x, y)$ region imaged in Figure (a) and (b). The energy intervals for which Figure (a) and (b) have been generated are marked with $\Delta\tau_a$ and $\Delta\tau_b$, respectively.

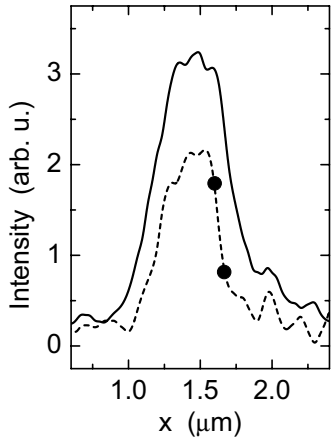

Figure 4.2: Line scans along the arrows drawn in Figure 4.1 (a) and (b). Solid and dashed lines are used for the line scans from (a) and (b), respectively.

The clear lack of an ideal pattern in Figure 4.1 (a) and (b), may result in an underestimation of the actual resolution. The value of $\tilde{\Delta}_s = 100\,\text{nm}$ should be taken as an upper limit for the spatial resolution, that may actually be better than estimated.
Both line profiles in Figure 4.2 bring approximatively to the same value of $\tilde{\Delta}_s$. In general the spatial resolution of a PEEM does depend on energy and energy range of the photoelectrons [Sch02c]. For very narrow energy

distributions the present microscope is capable of about 20 nm resolution [Zie98]. However, the bright patterns in Figures 4.1 (a) and (b) are connected with 3D nanostructures on the surface. The corresponding field deformation leads to a deterioration of the resolution [Nep02]. This is most likely the limiting factor for the lateral resolution in the images.

4.1.2 Energy resolution in the microspectroscopy mode

To determine the energy resolution $\tilde{\Delta}_E$ in the microspectroscopy mode we used a polycrystalline Cu sample prepared and cleaned in situ. The sample preparation procedure and its characterization are described in detail in § 4.2.1.
Figure 4.3 shows the 2PPE energy distribution spectrum of a $(10 \times 10)\,\mu m^2$ homogeneous region of the sample. (Throughout this work we will refer to the intensity as yield.) The Fermi level onset in the spectrum is the result of the absorption of two photons $\hbar\omega$ by the electrons at E_F. It is

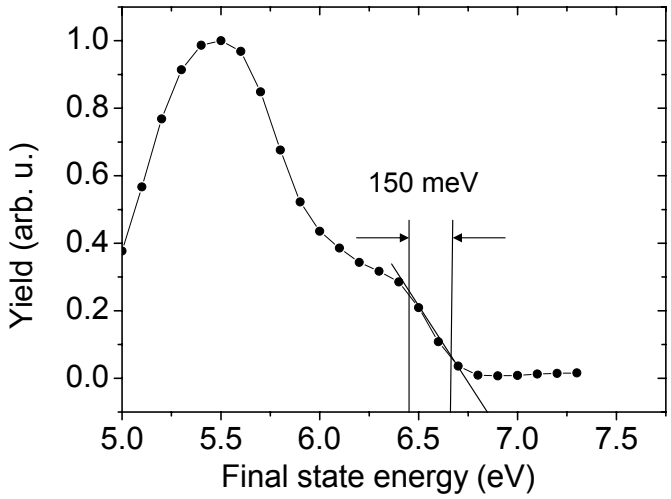

Figure 4.3: 2PPE energy distribution spectrum of a clean and homogeneous Cu surface, taken with s-polarized light at the photon energy $\hbar\omega = 3.3\,eV$. The evaluation of the width of the Fermi level onset to 150 meV allows to give an upper limit for the energy resolution. The Fermi level onset in the 2PPE spectrum at about 6.6 eV is the result of the photoemission of electrons at E_F after absorption of two photons $\hbar\omega$.

visible as a step-like enhancement of the intensity within a small energy interval. From the width of this edge we estimate the energy resolution to be $\tilde{\Delta}_E \approx 150\,\text{meV}$. The width has been evaluated using the distance between the points corresponding to 12% and 88% on the linear fit of the Fermi level onset shown in the Figure.
The value of 150 meV has to be seen as an upper limit for the energy resolution: in giving the intrinsic instrument energy resolution one should take into account the spread of the Fermi function at room temperature ($\approx 25\,\text{meV}$) and the bandwidth of the laser (for a pulse width of $\Delta t = 200\,\text{fs}$ one has $\Delta E \approx \hbar/\Delta t \approx 3\,\text{meV}$).
We conclude observing that we actually recorded different spectra corresponding to different regions of interest $\Delta(x, y)$. The upper limit for the energy resolution is not significantly influenced by this choice.

4.2 Observation and characterization of Cu surface inhomogeneities with two-photon photoemission

We now present the results of 2PPE TOF-Spectromicroscopy studies on a copper sample. The presence of inhomogeneities on the surface gives rise to an enhanced photoemission yield, as expected in the case of excitation of LSP's in the inhomogeneities themselves. Such single surface inhomogeneities, characterized by an enhanced two-photon photoemission yield have been termed in literature as *hot-spots* [Sch01b, Aes95, Fec02]. The spatially resolved energy distribution from hot-spot-like inhomogeneities is compared to the well-know energy distribution from the homogeneous Cu surface.

4.2.1 Sample preparation and characterization

The experiment has been performed in ultrahigh vacuum (UHV). The surface preparation was carried out in-situ starting from a polished, highly pure polycrystalline copper sample and following the procedure described in [Prz04]. Briefly, the mechanically polished Cu sample was inserted in vacuum and first cleaned by Ar^+ bombardment and heating cycles at 1200 K (indirect heating with the resistive filament behind the sample). Then, recrystallization was obtained through indirect heating with a power of 15 W for 20 h. After recrystallization, the described cleaning procedure was repeated once more.
Cleanness and geometrical order of the surface were checked by means of

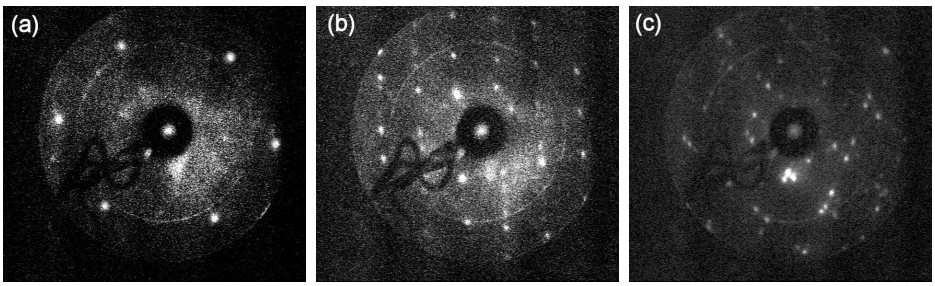

Figure 4.4: Example of LEED patterns obtained from the Cu sample after recrystallization. (a) Hexagonal pattern typical for a Cu(111) surface; energy 50 eV. (b) Pattern of a Cu(110) surface; energy 130 eV. (c) Pattern with pronounced superstructures; energy 82 eV.

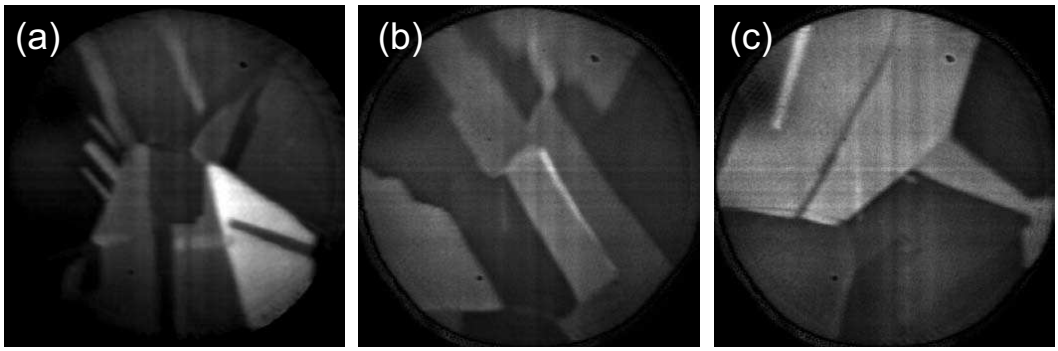

Figure 4.5: PEEM images of three different 500μm wide regions of the clean copper sample taken with the deep-UV lamp as excitation source. Due to their different work function, different crystallites are imaged by the PEEM with different gray levels.

low energy electron diffraction (LEED). Successive investigation with LEED showed the presence of large areas (several μm diameter) with low indexed Cu surfaces as well as domains with pronounced superstructures. Examples of obtained LEED patterns are shown in Figure 4.4.

Such a polycrystalline sample is advantageous for UV-PEEM experiments because the grains of the polycrystal can be imaged with high contrast. In fact, since crystallites with different surface orientations have different work functions, the total photoemission yield depends on the surface crystal orientation. The resulting difference in the intensity of the photoemission signal emerging from copper crystallites with different surface orientations is imaged by the PEEM as different gray levels.

Figure 4.5 (a), (b) and (c) show PEEM images of 500μm wide regions of the clean copper sample taken with the deep-UV lamp. Since its photon energy (cut off at 5.8 eV) is higher than the copper work function ($4.5 - 5$ eV depending on the crystal orientation, see Table 3.1) electrons are emitted from the sample surface through one-photon photoemission (1PPE). Different crystallites are clearly visible in these images.

After the experiments on the clean surface, cesium was deposited on the sample. The high reactivity of Cs makes the evaporation of pure Cs from a conventional source very difficult. In view of this problem, we used a specifically designed Alkali Metal Dispenser from SAES [SAE] . The Cs dispenser is a covered-boat containing Cs salts and reducing agents. When the dispenser is resistance-heated to a proper temperature in vacuum, high purity Cs vapor is generated. The specified activation current (4.7 A) was applied

to the dispenser for 10 minutes and then increased by 0.3 A for evaporation of Cs on the sample.

4.2.2 Results

Figure 4.6 (a) shows again the PEEM image of a 500 μm wide region of the sample taken with the deep-UV lamp (Figure 4.5 (a)). In the image the region R with size $90 \times 60\,\mu$m is marked. Figure 4.6 (b) shows a zoomed PEEM image of the region R, taken by illuminating the sample with the UV lamp for 180 s and afterwards with the s-polarized blue laser for 10 s. It shows a hot-spot located on the rim of a rectangular shaped crystallite. The spot appears 20 times brighter than the adjacent areas (note that the hot-spot is

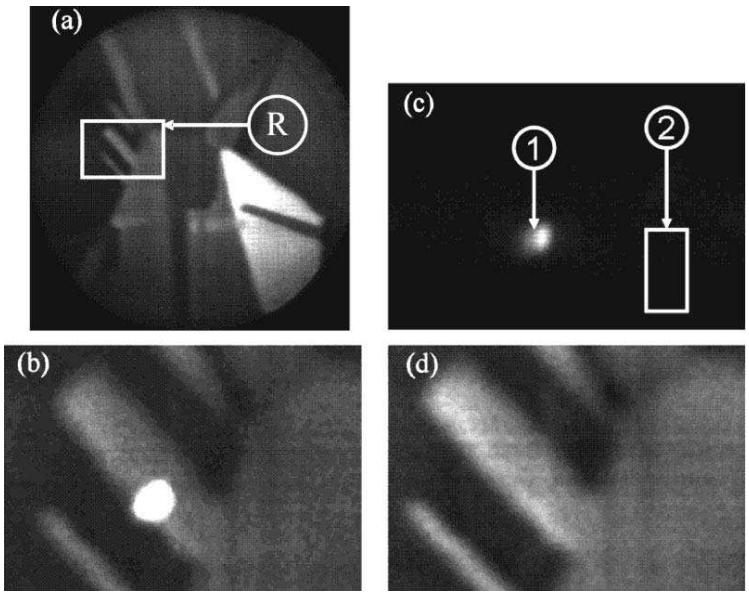

Figure 4.6: (a) UV-PEEM image of a copper surface with different crystallite orientations ($500 \times 500\ \mu m^2$). Region R ($90 \times 60\,\mu m^2$) has been marked. (b) Superposition of UV and blue laser (s-polarized) PEEM images of region R. (c) Energy integrated TOF-PEEM image of region R taken by illumination with the laser only. The regions marked with 1 (bright spot) and 2 (homogeneous surface) are taken as Δ(x,y)-regions of interest to obtain the spectra shown in Figure 4.7. (d) Same as (b) but with UV light only.

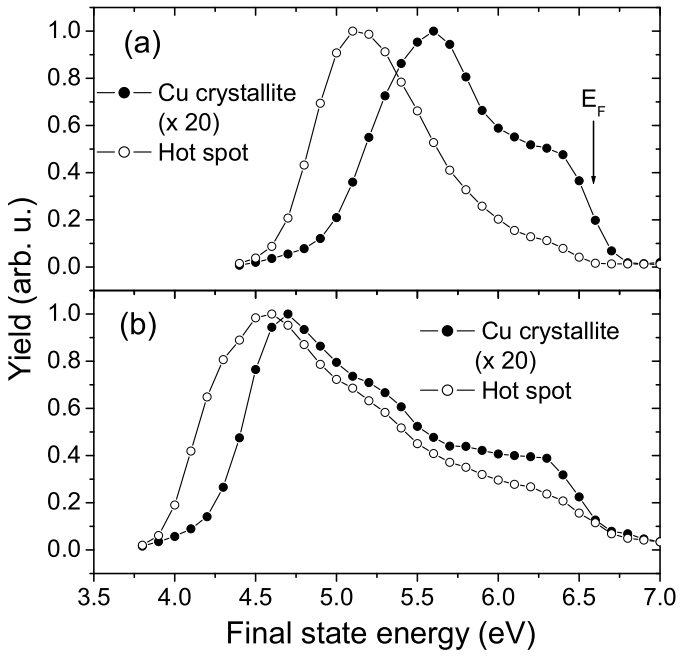

Figure 4.7: (a) Electron spectra of region 2 (homogeneous Cu crystallite, filled circles) and region 1 (hot-spot, empty circles) marked in Figure 4.6 for excitation by s-polarized laser light ($\hbar\omega = 3.3\,\mathrm{eV}$). The spectra are normalized to their maximum. (b) Same after lowering the work function via cesium deposition (1 min Cs exposure).

overexposed in (b)). Figure 4.6 (c) shows an energy integrated TOF-PEEM image[1] of the region R illuminated with the laser exclusively. Only the small spot with strongly enhanced emission yield is visible. Its spatial intensity distribution allows to estimate its diameter to about 400 nm. This value has to be seen as an upper limit for the real size of the hot-spot, because the field enhancement at small metal clusters may result in a virtual magnification of up to 50% of the real size [Dür02], that depends strongly on the electron-optical settings [Nep02]. Figure 4.6 (d) shows region R illuminated with the UV lamp. The hot-spot is not visible in this UV-PEEM image.

Figure 4.7 compares the photoelectron energy distribution of region 1 marked

[1]With *energy integrated* we mean that the 2D-plot has been generated in the spectro-microscopy mode by selecting the whole range of photoelectron energies.

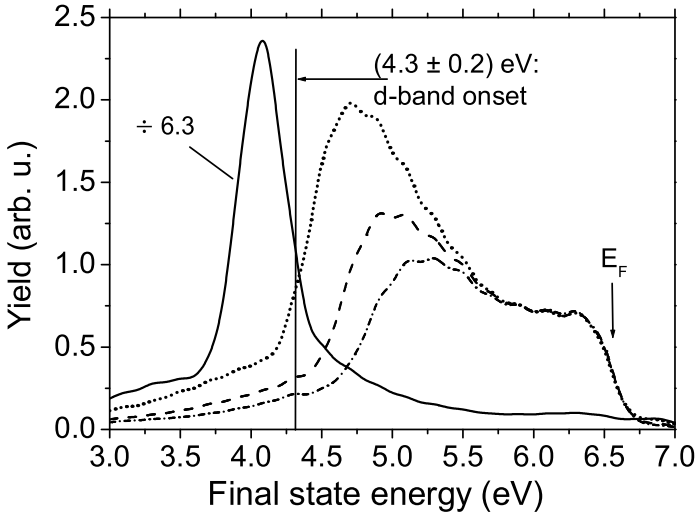

Figure 4.8: 2PPE electron energy distributions of a homogeneous part of the copper surface with different cesium coverages ($\hbar\omega = 3.3\,\mathrm{eV}$). Chain line: 30 s Cs deposition; dashed line: 1 min Cs deposition; dotted line: 2 min Cs deposition; continuous line: 4 min Cs deposition. The latter spectrum has been scaled down by a factor of 6.3.

in Fig.4.6 (c) (hot-spot) to that of region 2 (homogeneous part of the Cu surface). Figure 4.7 (a) displays the data for the clean surface and (b) for the same areas after deposition of cesium (1 min Cs exposure). In both figures the energy distribution spectra are normalized to their maximum. In the non-normalized data, the maximum of the hot-spot spectrum is a factor of 20 more intense than the maximum of the homogeneous surface (before and after cesiation).

Figure 4.8 compares 2PPE electron energy distributions of another homogeneous part of the Cu surface taken at different cesium coverages. The coverage is expressed in time of exposure to the Cs vapor generated from the Cs dispenser (30 s, 1 min, 2 min, 4 min). The fact that the work function difference between the hot-spot and the homogeneous Cu surface remains almost the same after cesiation (Figure 4.7 (b)), suggests that the hot-spot consists of Cu and is not an impurity.

The clean Cu surface exhibited different hot-spots under laser illumination. Figure 4.9 gives another example. In particular, Figure 4.9 (b) shows a PEEM image of the $10 \times 6\mu\mathrm{m}^2$ region of interest marked in (a) with a rectangle.

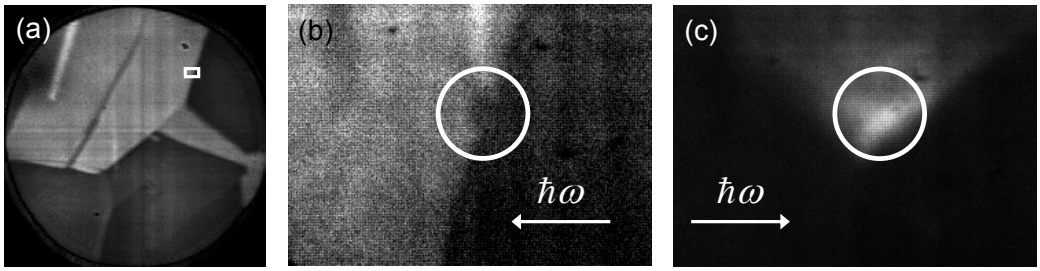

Figure 4.9: (a) UV-PEEM image of a 500 μm wide region of the polycrystalline copper sample taken with a deep-UV lamp as excitation source. (b) Detail image of the $10 \times 6\mu m^2$ region of interest marked in (a). (c) Fs-laser-PEEM image of the same region of the sample under s-polarized laser illumination (photon energy 3.3 eV). The 2PPE yield is strongly enhanced at the inhomogeneity marked with a circle. The arrows in (b) and (c) indicate the photon impact directions.

The image was obtained by illuminating the sample with the deep-UV lamp. Figure 4.9 (c) shows a PEEM image of the same region of the Cu sample, illuminated by s-polarized laser light with a photon energy of $\hbar\omega = 3.3\,\text{eV}$. Although (b) and (c) are taken at identical sample positions, the images look completely different. The laser-excited image shows a bright spot at a position that appears dark in the UV-PEEM image (b). The bright spot in (c) exhibits a caustic-like feature. The comparison makes clear that the 2PPE yield is strongly enhanced in the center of Figure 4.9 (c). According to (b) this area corresponds to a surface inhomogeneity at the border between two copper crystallites with different orientation, marked with a circle. The linear dimension of this inhomogeneity is approximately 400 nm. It should be noted, however, that the apparent sizes of 3D objects on surfaces can be considerably influenced by electron-optical artefacts in PEEM images [Nep02]. In particular, protruding objects give rise to deformations of the homogeneous extractor field that, in turn, can lead to an increase of the image size of the 3D object. Also, caustic-like features can be caused by the local field deformation.

4.2.3 Discussion

2PPE from the homogeneous clean Cu surface. The spectrum of the clean and homogeneous Cu surface in Figure 4.7 (a) agrees with the results found by Ogawa and Petek [Oga96]. The Fermi level onset is visible as step-like enhancement of the intensity within a small energy interval around the

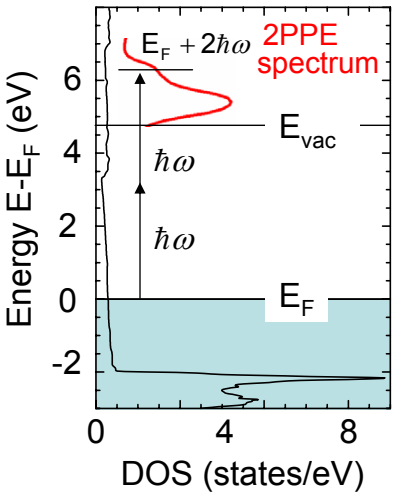

Figure 4.10: Calculated density of states (DOS) of Cu [Fec]. The Fermi level onset in the 2PPE spectrum is the result of the coherent absorption of two photons $\hbar\omega$ (depicted by arrows) from the electrons at E_F.

final state energy of 6.6 eV (see Figure 4.10).
Intense emission sets on at lower final state energy as indicated in the increase of the intensity towards 5.5 eV. The spectrum is terminated at the low-energy side by the work function threshold. Using (3.3) one finds that the work function of the analyzed Cu surface amounts to 5.1 ± 0.2 eV.
The intensity around 5.5 eV final state energy is attributed in [Oga96] to emission from the top of the filled d-bands. A careful analysis of the spectra from the cesiated surface in Figure 4.8 shows that this is energetically not possible. It is well-known that chemisorption of Cs on a Cu surface lowers the local work function through the induced adsorbate dipole[2]. Table 4.1 shows the lowering of the local work function after cesium chemisorption.

Exposure time	**Work function (eV)**
0 s	5.1 ± 0.2
30 s	4.8 ± 0.2
1 min	4.6 ± 0.2
2 min	4.3 ± 0.2
4 min	3.7 ± 0.2

Table 4.1: Lowering of the local work function after cesium chemisorption.

After 4 min of Cs deposition we observe a work function lowering relative to the clean surface of $\Delta\phi_m \approx 1.4$ eV, corresponding to $E'_{vac}(s) = 3.7 \pm 0.2$ eV.

[2] Actually through its component perpendicular to the surface.

Within the experimental error, we still have $E_{vac}(s) > \hbar\omega$. Thus, we can exclude that the photoemission from the 4 min cesiated surface is dominated by one photon photoemission[3]. Moreover, the shape of this spectrum, displaying a dominant peak, suggests another emission mechanism. With a local vacuum level of about 3.7 eV, two-photon photoemission from the filled d-bands is allowed at $\hbar\omega = 3.3$ eV.
Figure 4.11 shows that if the electrons are excited from the filled d-bands 2PPE may be mediated by a direct transition ($\Delta k = 0$) through a resonant **real** intermediate state[4] (full arrows). This results in an enhanced photoemission yield in correspondence of the direct transition (see § 3.3.1) and explains the shape of the spectra in Figure 4.8. Close to the K-point, transitions into real final states through a real virtual state are also possible (dashed arrows).
The above considerations allow us to conclude that the low final state energy signal in the spectra from the clean surface and from the surface with Cs coverage up to 2 min is not due to direct 2PPE from the filled d-bands. It has to be attributed to secondary electron emission, which mainly contributes to the 2PPE spectrum at low final state energies. In particular, the main decay channel for secondary electron generation is the *true secondary channel* described in § 3.5.1. This is dominant whenever 2PPE proceeds through virtual intermediate states, as for the Cu surface with up to 2 min Cs coverage. In fact, in such situations 2PPE proceeds essentially via simultaneous (coherent) excitations (see § 3.3).

2PPE from hot-spot-like surface inhomogeneities. The main differences between the spectrum of a hot-spot-like inhomogeneity and the Cu homogeneous surface are (see Figure 4.7):

(i) the low-energy cutoff (i.e. E_k^{min} in the notation of Chapter 2) of the hot-spot spectrum is shifted by about 0.3 eV towards lower final state energies. According to (3.3) this means that hot-spots are characterized by a lower work function than the homogeneous Cu surface;

(ii) before cesiation, the total photoemission yield from the hot-spot is a factor of 16 enhanced with respect to the homogeneous surface. The total photoemission yield was calculated by integrating the spectra in Figure 4.12 (a), plotted in the original scale and normalized to equal surface areas;

[3]This would be the case if $E_{vac}(s) < \hbar\omega$.

[4]Remember that without work function lowering, 2PPE from a smooth Cu surface proceeds only through **virtual** intermediate states.

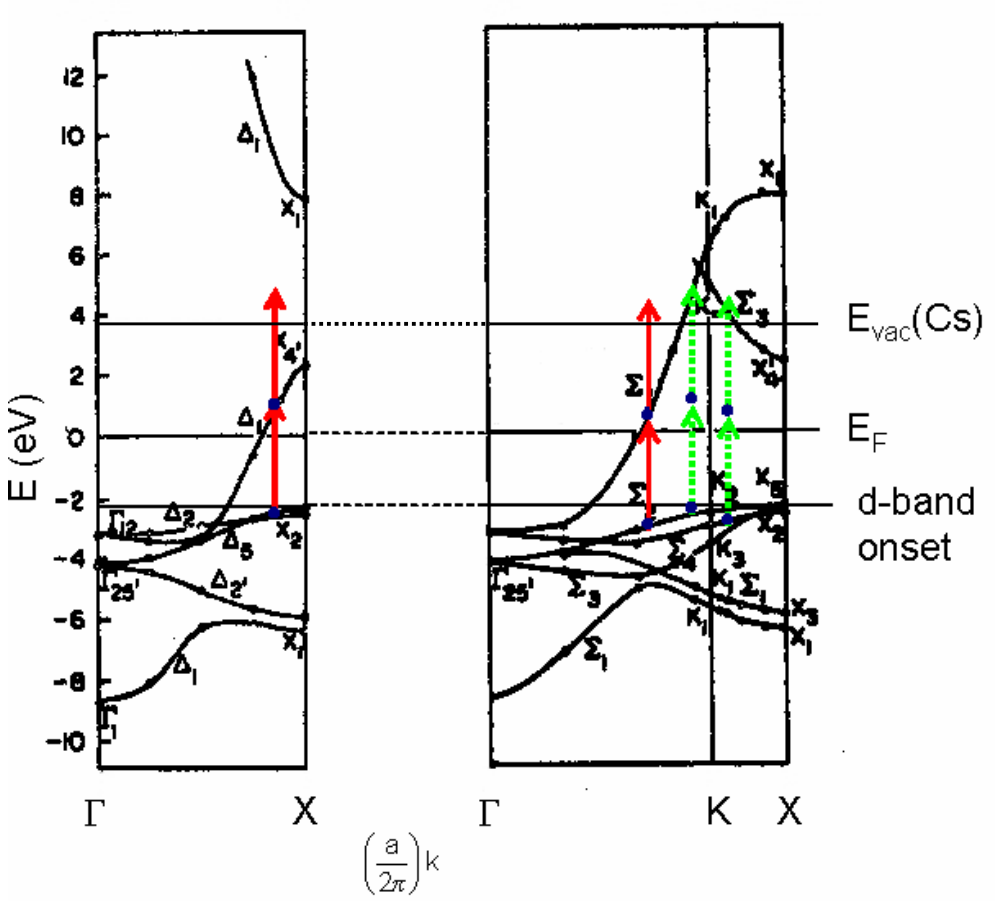

Figure 4.11: Emission from the Cu d-band through real intermediate states (calculated band structure from [Ber64b]). The horizontal lines at $-2.2\,\mathrm{eV}$ and $3.7\,\mathrm{eV}$ indicate the d-band onset and the vacuum level of the Cu sample after lowering the work function by Cs deposition, respectively. The vertical arrows have a length of $3.3\,\mathrm{eV}$ and thus indicate electron transitions after absorption of a photon with $\hbar\omega = 3.3\,\mathrm{eV}$. Two possible direct transition from the d-bands into intermediate real states are denoted (full arrows). The final states for 2PPE are evanescent states at the surface, which couple to the free electron states in the vacuum. Two alternative transitions close to the K-point end up in real states above E_{vac}(Cs) but proceed through virtual intermediate states (dashed arrows).

(iii) before cesiation, the hot-spot spectrum exhibits a Fermi level onset that is several times more intense but slightly broadened and shifted by about $0.1\,\mathrm{eV}$ to lower final state energies as compared with the

homogeneous surface: this can be easily recognized in Figure 4.12 (b);

(iv) the hot-spot spectra exhibit a much steeper increase of intensity towards lower energies than the spectra of the homogeneous surface.

In § 4.3 we will present and discuss the energy distribution curves from Ag nanoparticles deposited on a Si(111) substrate. The qualitative behavior of the hot-spot like Cu inhomogeneities (points (i) to (iv)) is compared with the results from the silver nanocluster film in § 4.4.
In order to facilitate a direct comparison with the Ag results, Figure 4.12 displays the hot-spot spectrum (full line) and the spectrum of the smooth surface (dashed line) on the identical intensity scale. The insert (b) shows the vicinity of the Fermi level onset.

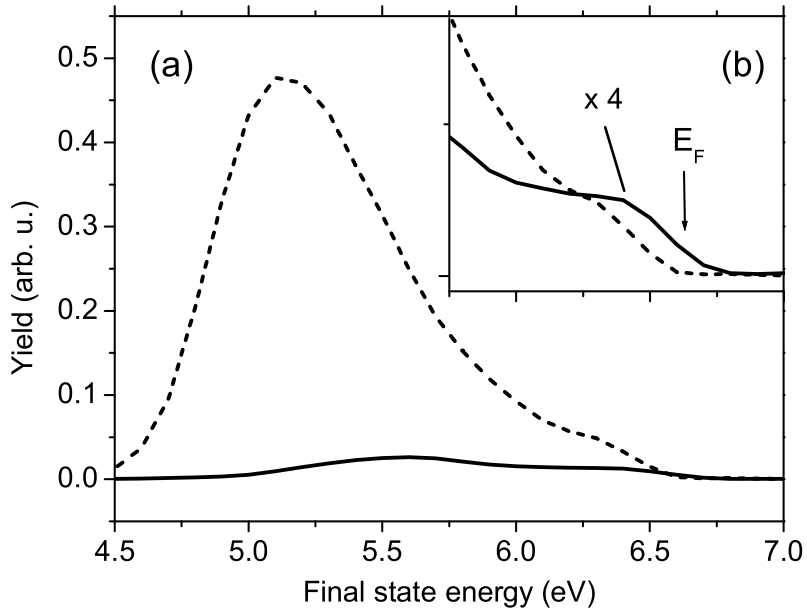

Figure 4.12: (a) Electron energy distribution spectra of region 2 (homogeneous Cu crystallite, continuous line) and region 1 (hot-spot, dashed line) marked in Figure 4.6. Excitation source: s-polarized laser light ($\hbar\omega$ = 3.3 eV). The spectra are presented with the original intensity. (b) Detail of the Fermi level onset of the spectra. The spectrum of the homogeneous Cu crystallite has been expanded by a factor of 4.

4.3 Two-photon photoemission from Ag nanoparticle films on Si(111)

In this Section we present the results of 2PPE TOF-Spectromicroscopy studies on a structured Ag sample. Regions of Ag nanoparticles with different average sizes and one region with a continuous 100 nm thick Ag film were deposited as a stepped wedge on a Si(111) substrate. Upon laser excitation the nanoparticle films exhibit a very high electron emission yield in the images, whereas the uncovered Si surface and the continuous Ag film are dark. We measured the electron energy spectra from the nanoparticle films spatially resolved, and observe that they are remarkably different from spectra of the continuous film, the latter being well-known from literature. The nanoparticle spectra are up to a factor of 70 more intense than the spectrum from the same area of the continuous film. They reveal different widths, overall shape and a shift and broadening of the Fermi edge. These results are discussed in § 4.4 in terms of LSP excitation in the nanoparticles and of its influence on the NZ field behavior.

4.3.1 Sample preparation and characterization

The Ag films were deposited in UHV by electron beam evaporation onto a Si(111) substrate at room temperature. The substrate was prepared by chemical etching with HF, Ar ion sputtering and heating for the removal of the native oxide. The sample consists of regions with different nominal thicknesses, prepared by moving a mask in front of the surface during exposure to the Ag atom beam. The thickness changes from 0 to 100 nm with three intermediate steps: 2, 5 and 20 nm; each step is 20 μm wide. The nominal thickness corresponds to the reading of the quartz balance thickness monitor. We label the regions of different coverage by numbers, with 1 corresponding to 0 nm Ag coverage (i.e. to the bare Si substrate), and with 2 to 5 corresponding to the regions with Ag film nominal thickness of 2, 5, 20 and 100 nm, respectively (see Figure 4.13).

It is well known that on this surface Ag forms 3D clusters at room temperature [Sam89]. The structure of the deposited films was investigated ex situ by atomic force microscopy (AFM). Figure 4.14 (a) to (d) show AFM images obtained from different Ag covered regions (field of view $2 \times 2\,\mu m^2$). They clearly illustrate the nanoparticle structure of the deposited film and its evolution with increasing coverage. The nanoparticles' lateral sizes appear distorted in the AFM images due to a tip convolution effect. Assuming that the grown particles approximately have a hemispherical shape (as observed

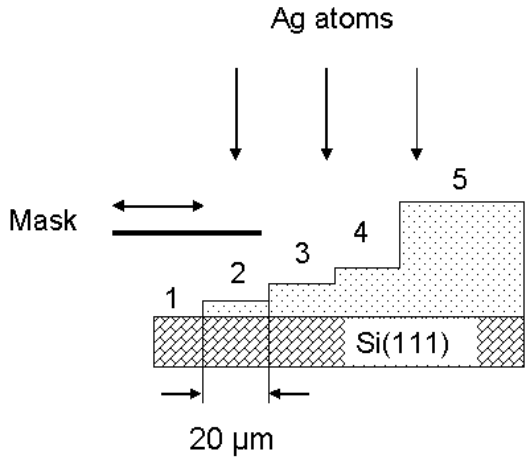

Region	Ag nominal thickness (nm) ±10%	Cluster radius R (nm) ±20%
1	0	0
2	2	20
3	5	25
4	20	40
5	100	—

Figure 4.13: Schematic representation of the sample preparation procedure and structure. Regions 1 to 5 correspond to an Ag film nominal thickness of 0, 2, 5, 20 and 100 nm, respectively. The average radius of the Ag nanoparticles grown in the different regions is given in the table. Region 5 corresponds to the continuous Ag film. Regions 2 to 4 are 20 μm wide.

for the 3D growth of Ag on Si(111) [Gav99]), we can roughly estimate their sizes through the measured height, that should be less affected by experimental errors. In Figure 4.14 (a), at a nominal thickness of 2 nm, only a small amount of Ag nanoparticles can be seen. Their area covers roughly 10 % of the substrate and they are characterized by an average height of about 20 nm corresponding to a radius of approximately $R = 20$ nm. In Figure 4.14 (b), at a nominal thickness of 5 nm, the particles cover approximately 20 % of the surface and have an average height of about 25 nm. Figure 4.14 (c) shows that at a nominal thickness of 20 nm the nanoparticles cover 50 % of the substrate. They become larger (height about 40 nm) and some of them nearly touch each other. Finally, at 100 nm thickness (Figure 4.14 (d)) the coalescence of the particles has lead to the formation of a film that covers more than 80 % of the substrate (continuous Ag film). After preparation the sample was transferred through air to the TOF-PEEM chamber. Before the measurements the surface was cleaned in UHV by mild argon-ion bombardment (5 min at an Ar pressure of $5 \cdot 10^{-7}$ mbar, energy 600 eV, sample current 5 mA).

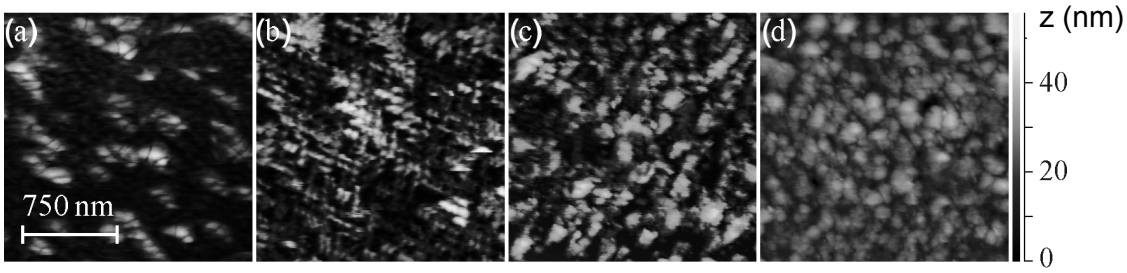

Figure 4.14: AFM images of regions 2 to 5 of the Ag film (field of view $2 \times 2\,\mu m^2$) corresponding to different nominal thicknesses: (a) 2 nm, region 2; (b) 5 nm, region 3; (c) 20 nm, region 4; (d) 100 nm, region 5.

4.3.2 Results

Figure 4.15 shows two PEEM images of the same region of the stepped Ag wedge illuminated with the UV lamp (a) and the p-polarized laser source (b). The step borders are indicated by arrows. In both images the brightness in a given area is proportional to the intensity of electron emission from that area. The Ag nanoparticle film looks essentially different in the electron emission images upon excitation with UV radiation or femtosecond laser pulses. In particular region 5 (the continuous Ag film) appears bright in the UV (a) but dark in the laser-excited PEEM image (b).
The intensity profiles taken from these images along section AB (white line in Fig. 4.15 (a)) are shown in Figure 4.16. The intensity profile from Fig. 4.15 (a), i.e. for UV excitation (plotted as dashed line in Figure 4.16) shows a monotonous increase of the electron emission with increasing Ag coverage from region 1 to 4. This reflects the increasing coverage of the surface with Ag clusters. The Ag continuous layer in region 5 is characterized by a UV photoemission yield which is a factor of 1.3 smaller than for the particle film in region 4. This can be easily explained by taking into account that the escape function of a rough surface T_R is larger than the corresponding quantity of a smooth surface T_S (see § 3.3.2). In addition, the local work function of the particles decreases due to the local fields appearing between the particles themselves and the substrate. The last assumption is proven by the TOF spectra, see below. Concerning the bare Si surface (region 1) it is known to appear very dark in UV-PEEM images. The bright spot in the upper left of Figure 4.15 (a) and (b) is a defect.
The intensity profile from Figure 4.15 (b), i.e. for p-polarized femtosecond laser excitation (full line in Figure 4.16), reveals a non-monotonous change of the electron emission intensity with the nominal film thickness, i.e. , with the

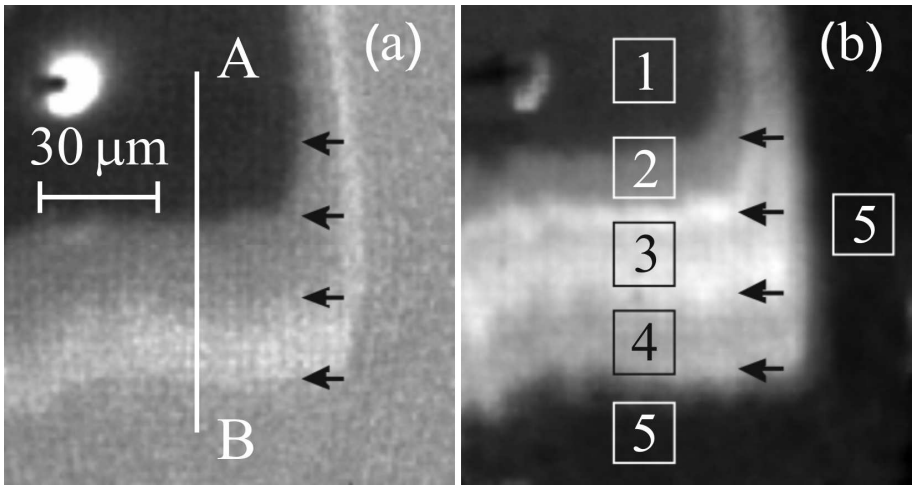

Figure 4.15: (a) PEEM image of a region of the Ag sample for UV light illumination. (b) Same for femtosecond laser illumination ($\hbar\omega = 3.1\,\mathrm{eV}$, p-polarized). Regions with different Ag coverage are labelled with 1 to 5. Their borders are indicated by arrows. The white line AB indicates the position where the intensity profiles were taken (see Figure 4.16). Squares along the line AB mark areas of TOF spectra measurements (see Figure 4.18).

Ag particle areal density and size. Here, the emission from the nanoparticle film is two orders of magnitude more intense than that of the continuous Ag layer. The measured intensity profile exhibits a step-like behavior clearly correlated with the stepped wedge of the Ag coverage profile. The emission intensity shows a maximum at region 3, i.e. at a nominal Ag film thickness of 5 nm (corresponding to a particle radius of approximately $R = 25\,\mathrm{nm}$). The emissivity of the adjacent regions 2 and 4 (nominal thickness 2 and 20 nm) is reduced by factors of 2.5 and 1.7, respectively. The continuous Ag film (region 5) and the bare Si (region 1) are characterized by very low emissivities.

Figure 4.17 compares the line scans taken along the same line in two PEEM images of the region shown in Figure 4.15, illuminated by s- and p-polarized light (s-polarization with full line, p-polarization with dashed line). Neglecting the difference in the total intensity, the two curves show a similar qualitative behavior. Closer inspection reveals, however, that the s-polarized laser light enhances the emission from the smallest particles in region 2 as compared to regions 3 and 4. In the following we will concentrate our attention on the measurements performed with p-polarized light. On the basis of the discussed result, the same considerations hold for the measurements

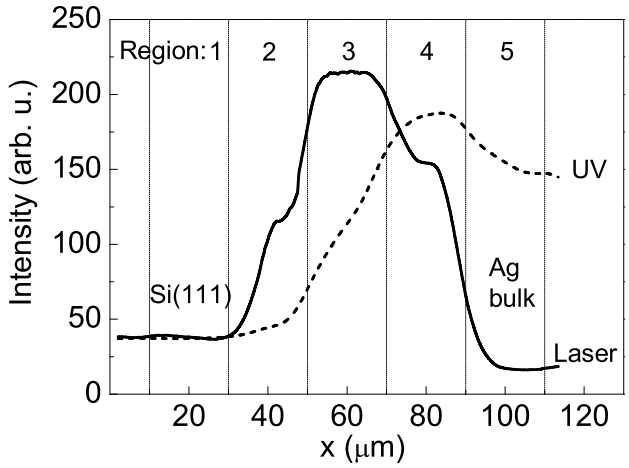

Figure 4.16: Intensity profiles taken from the images in Figure 4.15 (a) (UV illumination, dashed line) and Figure 4.15 (b) (laser illumination, continuous line) taken along AB, see Figure 4.15 (a). The vertical lines indicate the position of the borders between regions 1 to 5.

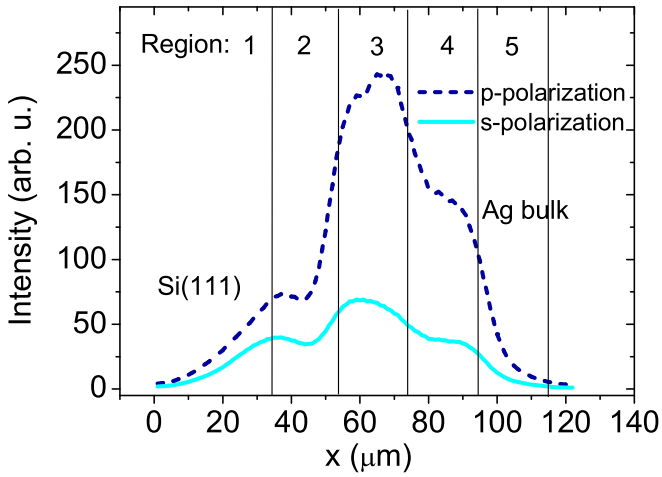

Figure 4.17: Intensity profiles of two PEEM images of the region shown in Figure 4.15, illuminated respectively by s- and p-polarized light. Dashed line: p-polarization, full line: s-polarization.

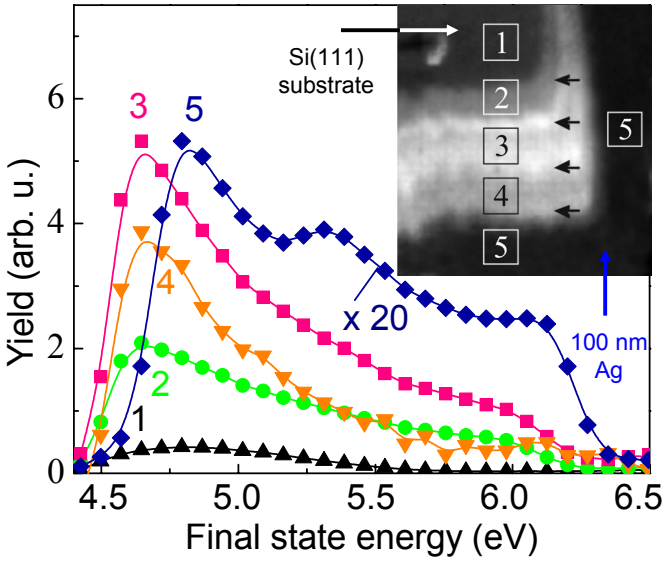

Figure 4.18: Ag-spectra plotted as function of the electron final state energy for the square areas 1 to 5 marked in Figure 4.15 (b) (and shown in the inset) taken with p-polarized femtosecond laser illumination at $\hbar\omega = 3.1\,\mathrm{eV}$. The curves are numbered corresponding to the regions defined in Figure 4.15. Since the intensity from the continuous Ag layer (region 5) is very small, the corresponding spectrum was expanded by a factor of 20.

with s-polarized laser light.

In order to gain further information on the emission enhancement mechanism of the Ag nanoparticle films in the case of laser illumination, we investigated the kinetic energy distribution of the emitted electrons using the TOF-PEEM spectroscopy mode. The spectra corresponding to square areas 1 to 5 marked in Figure 4.15 (b) are shown in Figure 4.18. Note that the intensity scale of the spectrum corresponding to region 5 (continuous Ag layer) has been expanded by a factor of 20.

It should be pointed out that all spectra of Figure 4.18 have been extracted from one measurement, i.e. the 4D-data set $J = J(\mathrm{x,y,}\tau)$ acquired in the TOF modus from the regions 1 to 5 marked in Figure 4.15. This ensures that the absolute intensity scale, energy positions and resolution are perfectly identical in all spectra.

4.3.3 Discussion

2PPE from the continuous Ag film (region 5). The spectrum of the electrons emitted by the continuous Ag film (area 5 in Fig. 4.15 (b)) is plotted in Figure 4.19. It reflects the well known two-photon photoemission spectrum of bulk Ag [Bau02]. In particular, it shows three main features:

- the Fermi level onset E_F, visible as a step-like enhancement of the intensity within a small energy interval around 6.2 eV final state energy;
- a maximum at low final state energies. As for the Cu 2PPE spectrum discussed in § 4.2.3, the maximum is due to true secondary electron emission;
- a shoulder at 5.3 eV final state energy, due to a direct band-to-band transition between the upper and lower sp-band along the [111] (i.e. Λ-) direction [Paw98] (proceeding through a virtual intermediate state, see arrows in Figure 3.18 in Γ-L direction);

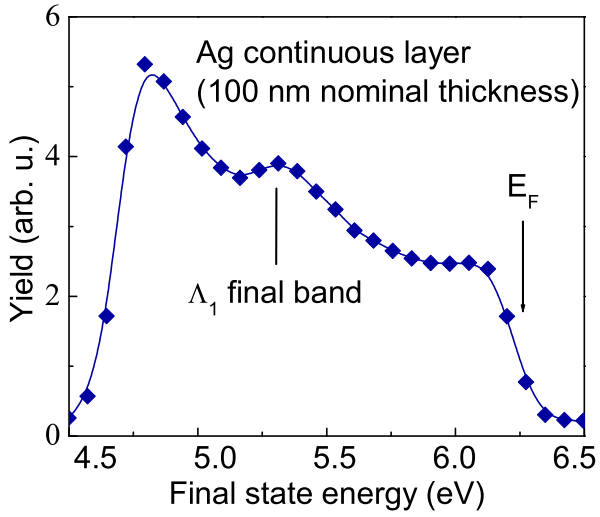

Figure 4.19: Spectrum of the continuous Ag layer (region 5) illuminated by p-polarized laser light with $\hbar\omega = 3.1$ eV photon energy. The Fermi level onset is marked with an arrow, the position of the 2PPE intraband transition to the Λ_1 band by a bar.

2PPE from the Ag nanoparticle films (regions 2 to 4). The spectra of the Ag nanoparticle films reveal qualitative and quantitative differences. They exhibit a much stronger and pronounced low energy peak (for region 3 it is 20 times higher than for the continuous layer). The low-energy cut off of the nanoparticle spectra (reflecting the energy position of the local vacuum level) is shifted to lower final state energy, cf. Figure 4.18. Using (3.3) we can evaluate the local work function of regions 2 to 4 to be $4.6 \pm 0.2\,\mathrm{eV}$ and of region 5 to $4.7 \pm 0.2\,\mathrm{eV}$. Thus, the local work function is about 0.1 eV (± 0.05 as derived from Figure 4.18) lower for the nanoparticles in regions 2, 3 and 4 than for the continuous layer (region 5).

No other features are visible in the spectra of the nanoparticle films on the linear intensity scale. Only when we plot the spectra on an expanded scale, the Fermi level onset becomes visible in the spectra. Figure 4.20 compares the behavior at the Fermi level onset of the nanoparticle film in region 3 with the Ag continuous layer of region 5. The spectrum of region 5 was scaled by a factor of 8, because the Fermi level onset in the nanoparticle spectra is about 8 times more intense than that of the continuous film. Further, it is slightly broadened and significantly shifted to lower final state energies.

The nanoparticle structure of the deposited Ag films plays obviously an important role both for the total intensity of the electron emission and for the electron kinetic energy spectra. To summarize, in analogy with § 4.2.3, we observe four main differences between the spectra of the continuous Ag layer and those of the particle films:

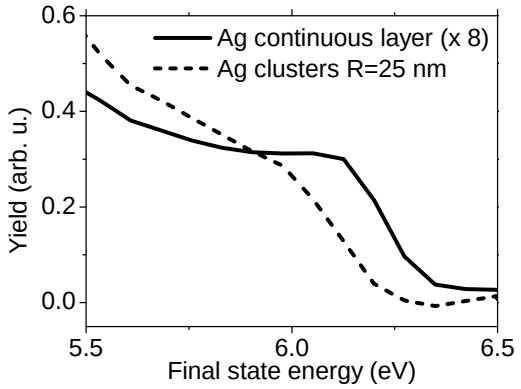

Figure 4.20: Behavior at the Fermi level onset of the nanoparticle film in region 3 (dashed line) and the Ag continuous layer of region 5 (full line). The spectrum of region 5 was scaled by a factor of 8.

(i) the nanoparticle films are characterized by a lower work function than the continuous film ($\Delta\phi_m \approx 0.1\,\mathrm{eV}$);

(ii) the nanoparticle film regions are characterized by a strongly enhanced image intensity, i.e. total electron emission yield (see Table 4.2);

(iii) the nanoparticle spectra exhibit Fermi level onsets that are several times more intense but slightly broadened and shifted by about 120 meV to lower final state energies as compared with the continuous layer.

(iv) the nanoparticle spectra exhibit a much steeper increase of the intensity towards lower energies as compared with the continuous layer.

These results are discussed in § 4.4.

Region	**Ag film nominal thickness (nm)**	**Average particle radius (nm)**	**Total electron emission yield (arb.u.)**
1	0	-	25 ± 2
2	2	20	95 ± 9
3	5	25	210 ± 21
4	20	40	130 ± 13
5	100	-	12 ± 2

Table 4.2: Photoemission yield from regions 1 to 5 under p-polarized laser illumination, obtained from integration of the spectra in Figure 4.18. These values are in good agreement with the intensities in the line scan of Figure 4.16.

4.3.4 Further results

Using the procedure described in § 4.3.1 we prepared a further sample consisting of Ag nanoparticle films deposited on a Si(111) substrate. It consists of 4 stripes (20 μm wide) with different nominal thicknesses varying between 0.5 nm and 10 nm and a thick continuous Ag layer. To distinguish this sample from the one described in § 4.3.1, we label the prepared films with letters. Table 4.3 summarizes the preparation data. Figure 4.21 shows an image of the prepared sample taken with an optical microscope.

Region	**Ag nominal thickness (nm)** ($\pm$**10** %)
A	0
B	0.5
C	1
D	2
E	10
F	100

Table 4.3: Nominal thickness of the prepared Ag films. Here, the films are labelled with letters (A to F). Region A corresponds to the bare Si(111) substrate, region F to a 100 nm thick continuous Ag layer.

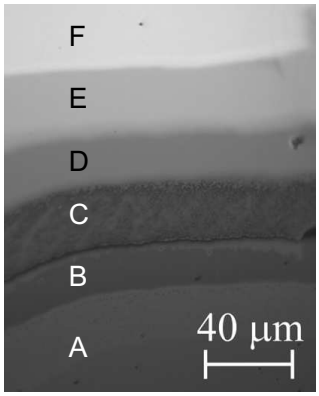

Figure 4.21: Image of the prepared sample taken with an optical microscope. The prepared stripes (marked with letters from A to F as in Table 4.3) are clearly visible.

Figure 4.22 shows PEEM images of the investigated sample obtained using the UV-lamp (Figures (a) and (c)) and the blue fs-laser (Figures (b) and (d)) as excitation sources. The images in (c) and (d) have been taken after cesium deposition onto the sample surface. Regions A to F have been marked in (c). Before cesium deposition, the PEEM images (a) and (b) reveal the same behavior of the Ag nanoparticle film described in § 4.3.1. After cesium chemisorption, the image (c) obtained with UV-light excitation shows an inverted contrast with respect to image (a) registered before cesiation. This is probably connected with the much larger surface area of the Ag cluster films, and hence a lower amount of Cs per surface unit. As a consequence the Ag

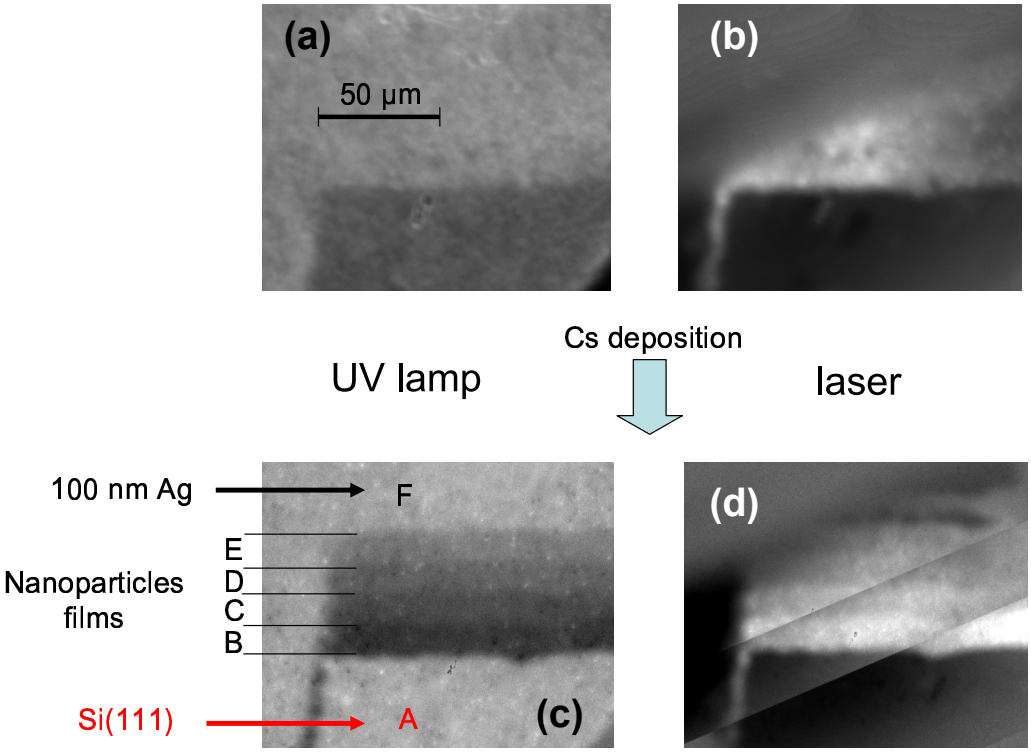

Figure 4.22: PEEM images of the investigated sample taken with UV-light (a) and (c) and with the blue fs-laser (b) and (d). (a) and (b) before cesiation, (c) and (d) after cesiation. The regions A to F are marked in (c). The diagonal lines in (d) are an artefact.

cluster films (regions B to E) exhibit a smaller work function decrease. This fact is confirmed by the 2PPE spectra presented in Figure 4.23. In particular, using equation (3.3) we evaluated the lowering of the work function in the Ag continuous layer (region F) to (0.7 ± 0.05) eV, while in the nanoparticle films of region C the lowering is (0.4 ± 0.05) eV.
Note, however, that the contrast of the fs-laser images in Figure 4.22 (b) and (d) is not affected by this fact. We will discuss this effect in § 4.4.

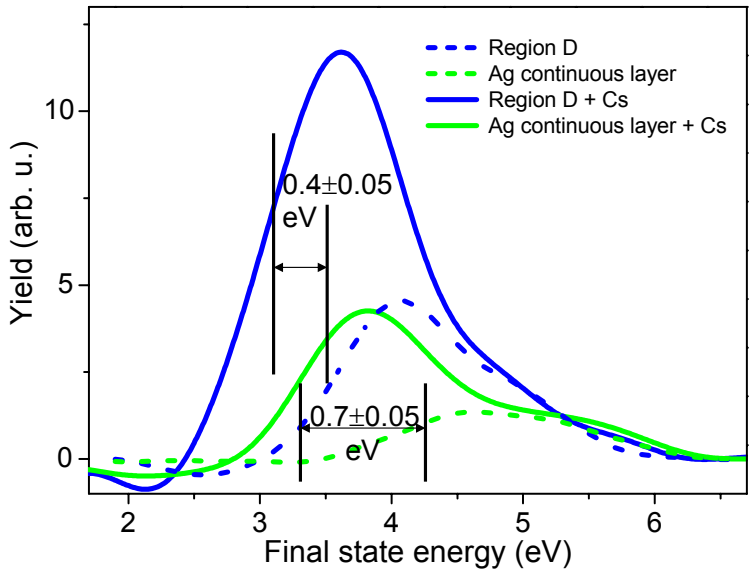

Figure 4.23: 2PPE spectra of the Ag continuous layer and of the nanoparticle film of region D, before and after cesiation. The intensity scale is identical for all curves. Both regions were exposed to the same amount of Cs. The changes in the work function are marked.

4.4 General considerations

We now give a detailed explanation of the features of the electron distribution spectra summarized in points (i) to (iv) in § 4.2.3 and § 4.3.3. If not otherwise stated, in this section we refer to:

- the Cu hot-spot and homogeneous Cu crystallite of Figure 4.6 (c) with the corresponding spectra of Figure 4.7 (a);
- the Ag nanoparticle film of region 3 and the Ag continuous layer of region 5 in Figure 4.15 (b) with the corresponding spectra of Figure 4.18.

4.4.1 Work function difference

We briefly recall point (i): the Cu hot-spot like inhomogeneities and Ag nanoparticles are characterized by a lower work function ϕ_m than the relative homogeneous surface ($\Delta\phi_m = 0.3\,\text{eV}$ for Cu and $0.1\,\text{eV}$ for Ag). We now present three possible explanations for this behavior and then discuss separately the case of Ag and Cu:

1. A first possible explanation is that the image forces acting on an electron emitted from a metal particle or from a planar surface differ from one another [Woo81, Nep85]. The image force is the principal interaction acting on an electron beyond a few Ångstroms above the surface. It directly influences the position of the vacuum level $E_{vac}(s)$, and therefore the position of the local work function of the sample ϕ_m (see § 3.1). In particular, the image force just outside a neutral metallic sphere with radius R, is smaller than just outside a metal plane. Thus, one expects a **reduction** of the local work function for the metal sphere by an amount $\Delta\phi_m$ relative to the planar value, with:

$$\Delta\phi_m(R) = \frac{5}{8}\frac{e^2}{R} \approx \frac{0.90}{R\,[\text{nm}]}\ \text{eV}\,. \tag{4.1}$$

   On the other hand, if the positive unit charge $+e$ of the photohole remains on the isolated sphere, it gives rise to an additive attractive energy e^2/R which will increase the work function. Adding the contribution of the image potential, one obtains a net **increase** of the work function $\Delta\phi_m$ relative to the planar value, with:

$$\Delta\phi_m(R) = \frac{3}{8}\frac{e^2}{R} \approx \frac{0.54}{R\,[\text{nm}]}\ \text{eV}\,. \tag{4.2}$$

These changes of the work function can reach several tenths of an eV. They are relevant in the range of particle sizes $R > 1.5\,\text{nm}$. If the radius R is smaller than 1.5 nm, the work function strongly increases due to quantum size effects, which have not been taken into account in [Woo81] to obtain (4.1) and (4.2).

2. The excitation of LSP's in the Cu hot-spot like inhomogeneities and in the Ag nanoparticles produces an enhanced NZ field. In § 3.5.3 it was shown that if the local field is sufficiently strong, electrons with energy closely below E_F may escape into vacuum by tunnelling through the potential barrier (cold field emission). This is possible if the NZ electric field amplitude reaches approximately 2 to 3 $\text{V}\cdot\text{nm}^{-1}$. Moreover, electrons excited by one or two photons into intermediate states with energies closely below $E_{vac}(s)$ may also tunnel through the temporarily lowered surface barrier. This process should be possible also for lower values of the local field. Experimentally, both electron emission mechanisms would result in a widening of the spectra towards lower final state energies and could explain the measured shifts.

   To discuss this possible effect more quantitatively, let us calculate the maximal value of the electric field E^0_{max} of the incoming laser beam. To do this, we assume that the laser pulse has a rectangular shape and a width given by the specified Full Width at Half Maximum (FWHM$\approx$ 200 fs), as depicted in Figure 4.24.

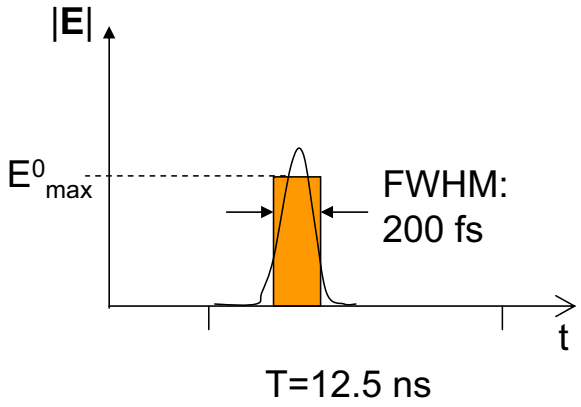

Figure 4.24: To evaluate the maximal value of the electric field in the fs laser beam, the laser pulse has been approximated by a rectangular pulse with width 200 fs.

The power dW of a free electromagnetic wave incident on a surface A in vacuum is given by:

$$dW = \varepsilon_0 Ac|\mathbf{E}|^2\, dt\ , \tag{4.3}$$

where c is the speed of light, ε_0 the vacuum dielectric constant and $\mathbf{E}$ the electric wave vector. To evaluate E^0_{max} we observe that:

$$\begin{aligned}\int_0^T dW &= \overline{W}\cdot 12.5\, ns = \\ &\approx \int_0^{200\,\mathrm{fs}} \varepsilon_0 Ac(E^0_{max})^2\, dt\ ,\end{aligned} \tag{4.4}$$

where $\overline{W}$ is the average laser power ($\approx$100 mW) and $T = 12.5$ ns is the laser repetition period. Inserting these values with $A = 100\cdot 250\,\mu\mathrm{m}^2$ (which corresponds to the laser spot size on the sample) in (4.4), we obtain $E^0_{max} \approx 1\cdot 10^7 \mathrm{V{\cdot}m^{-1}}$. To roughly estimate the maximal NZ field E^{NZ}_{max} generated by such an incoming field, in the following we will multiply E^0_{max} by the square root of the NZ efficiency[5] Q_{NZ} defined in § 3.2.4.

3. The action of the local contact potential differences between the nanoparticle and the substrate. The contact potential leads to microfields (also referred to as *patch fields*) about the nanoparticle that can be either attractive or repulsive for the escaping electron. This phenomenon occurs whenever particle and substrate have different material constituencies, i.e. it is relevant for the Ag on Si case but not for the Cu inhomogeneity.

Ag nanoparticles. The linear dimensions of the Ag particles deposited in the regions 2 to 4 are in the range 20 nm$< R <$40 nm. Assuming no charging on the nanoparticles, in first approximation considerable as spherical, (4.1) predicts an image-force induced lowering of the local work function of $0.02\,\mathrm{eV} < \Delta\phi_m < 0.04\,\mathrm{eV}$. This value lies somewhat below the observed shift of 0.1 ± 0.05 eV. However, the experimental error is in this situation too high to make any reliable conclusion. Probably for the same reason, we do not observe a size-dependent work function lowering, but the same shift of 0.1 eV for all particle sizes.

[5]Remember that Q_{NZ} expresses the enhancement of the NZ field **intensity**. That's why we take its square root.

In § 4.4.3 we discuss the behavior of the energy distribution spectra at the Fermi level onset. We will see that one of the spectral features (namely, the shift of the Fermi level onset towards lower final state energies) can be understood if one assumes that a unit positive charge $+e$ remains on the Ag nanoparticles during the time scale relevant for the 2PPE process. In this case (4.2) predicts a small **increase** of the local work function ($0.01 < \Delta\phi_m < 0.03\,\mathrm{eV}$), which is not observed.
We now ask the question whether field emission could affect the local work function of the Ag nanoparticles in regions 2 to 4. For Ag spheres with radius $R = 22\,\mathrm{nm}$, Figure 3.12 (a) gives the value $Q_{NZ} \approx 1000$ at the resonance wavelength 400 nm ($\hbar\omega = 3.0\,\mathrm{eV}$). Using this value we can roughly approximate the maximal value of the NZ field in the nanoparticle films:

$$E_{max}^{NZ} = \sqrt{Q_{NZ}} \cdot E_{max}^{0} \approx 3 \cdot 10^8 \,\frac{\mathrm{V}}{\mathrm{m}}\,. \tag{4.5}$$

The field E_{max}^{NZ} is an order of magnitude too small to allow cold field emission. On the other hand, it could be enough to allow tunnelling of photoexcited electrons with energy closely below $E_{vac}(s)$. If this was true, one should expect a strong dependence of the work function shift on the laser power. Figure 4.25 shows the spectra of the nanoparticle film in region 3 taken with different laser average intensities (from 58 mW to 10 mW). The value of E_k^{min} does not depend on the laser power. Thus, according to (3.3), there is no dependence between the local work function and the laser power. This supports the hypothesis that the recorded lowering of the work function is **not due to field emission from the Ag nanoparticle films**. Note, however, that measurements with a higher energy resolution would be necessary to completely rule out a small contribution from this emission mechanism.
The recorded work function lowering is most probably connected to the appearance of **local fields** between particles and substrate. They arise due to the contact potential difference and lead to a lowering of the local vacuum level $E_{vac}(s)$ in the nanoparticles. Figure 4.26 shows that the work function of the Ag continuous layer (region 5) is approximately 0.25 eV higher than that of the (p-doped) Si substrate. This gives rise to a local microfield between a Ag cluster and the Si surface. The field is directed from the substrate to the Ag particle, i.e. the electrons are accelerated when escaping from the particle.
This, in turn, causes the local vacuum level of the particle to be pulled down towards that of the substrate. For the continuous Ag film these local patch fields are absent except at the rim of the film [Nep85].

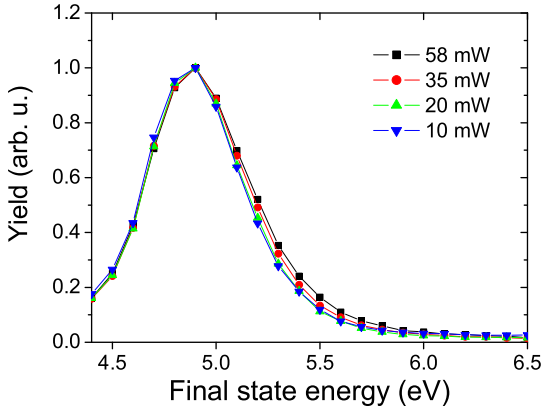

Figure 4.25: Spectra of the Ag nanoparticle film in region 3 taken with different average laser intensities (from 58 mW to 10 mW). The spectra have been normalized to unity.

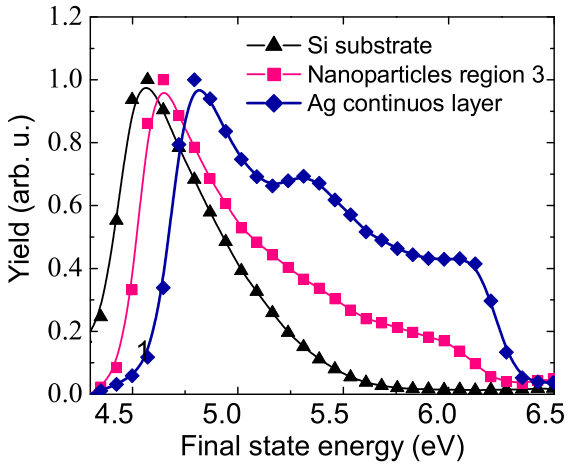

Figure 4.26: Comparison between the energy distribution spectra of the Ag continuous layer (region 5), the Si(111) substrate and the Ag nanoparticle film of region 3. All the spectra have been normalized to unity.

Cu hot-spot like inhomogeneities. Assuming that the hot-spot like inhomogeneity has a spherical shape with radius $R = 200\,\text{nm}$, equation (4.1) predicts a local work function lowering of $\Delta\phi_m = 0.005\,\text{eV}$. In this case, the change in the mirror forces on small spherical particles is far too small to explain the measured work function lowering of 0.3 eV, even within the experimental error ($\approx 0.05\,\text{eV}$).
Moreover, Figure 3.13 (b) gives the value $Q_{NZ} \approx 15$ for Cu nanospheres with radius $R = 100\,\text{nm}$ at the wavelength $\lambda = 400\,\text{nm}$. Thus:

$$E_{max}^{NZ} = \sqrt{Q_{NZ}} \cdot E_{max}^{0} \approx 4 \cdot 10^7 \,\frac{\text{V}}{\text{m}}\,, \tag{4.6}$$

which is two orders of magnitude too small to allow field emission.
The measured lowering of the work function may be explained by one of the following arguments:

- the hot-spot may consist of a different material characterized by a lower work function than Cu, for example Cu oxide or some impurity on the surface. This hypothesis is contradicted by the fact that the work function lowering $\Delta\phi_m \approx 0.3\,\text{eV}$ remains the same after cesiation. In fact, one expects cesiation to influence the work function of different materials in different ways.

- The hot-spot may consist of a Cu grain with different crystal orientation than the substrate. Table 3.1 shows that different Cu crystal orientations reveal differences in the local work function of up to 0.5 eV. A shift of 0.3 eV is, under this assumptions, not surprising. To support this hypothesis we analyzed the spectra of different hot-spot like inhomogeneities. Figure 4.27 shows another region of the Cu sample ($100 \times 100\,\mu\text{m}^2$) that presented different hot-spots. The spectra of these hot-spots have the same qualitative behavior as the spectrum in Figure 4.7. However, they reveal different values for the work function. A comparison of the different results is given in Table 4.4. All the analyzed hot-spots present a lower work function than the clean Cu surface ($\phi_m = 5.1\,\text{eV}$). The lowering ranges between 0.3 eV (corresponding to $\phi_m = 4.8\,\text{eV}$) and 0.5 eV (corresponding to $\phi_m = 4.6\,\text{eV}$). This supports our hypothesis of different grain orientations..

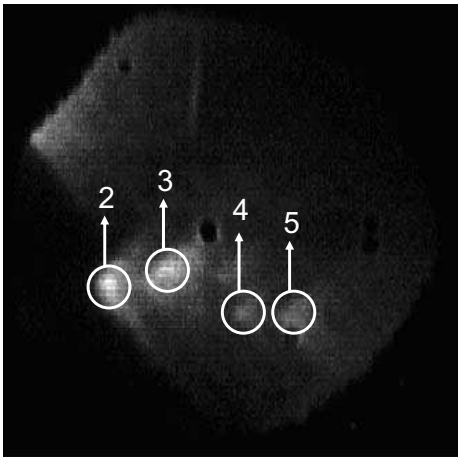

Figure 4.27: Energy integrated TOF-PEEM image of a region of the clean Cu sample prepared as described in § 4.2 and illuminated with laser light (hν=3.3 eV, s-polarization). Field of view $100 \times 100\,\mu m^2$. Different hot-spots can be seen in the image. They have been labelled with 2 to 5.

Hot spot	**Local work function**
1	(4.8 ± 0.1) eV
2	(4.6 ± 0.1) eV
3	(4.7 ± 0.1) eV
4	(4.8 ± 0.1) eV
5	(4.6 ± 0.1) eV

Table 4.4: Comparison between the work function of different hot-spots. Hot spot 1 is the hot-spot in Figure 4.6 (b) and (c); hot-spots 2 to 5 are marked in Figure 4.27. The work function has been determined by evaluating the width of the electron energy distribution spectra of every hot-spot and applying equation (3.3).

4.4.2 Total photoemission yield

We now address result (ii): the total 2PPE yield (i.e. the area under the energy distribution curves) is a factor of 17 higher for the Ag nanoparticle film in region 3 than for the Ag continuous layer (see Table 4.2). If we take into account the coverage of the substrate surface as discussed in § 4.3.1, a factor of 4 (80 % vs. 20 %) enters. Thus, a nanoparticle in region 3 emits on the average about 70 times more electrons than a region of the continuous layer with equal lateral size. Similarly, the total 2PPE yield from the Cu hot-spot like inhomogeneity of Figure 4.6 (c) is about 16 times enhanced with respect to the yield of the corresponding homogeneous surface.
From the considerations in Chapter 3 it is clear that the 2PPE yield enhancement from metal nanoparticles is a consequence of the combination of three factors:

1. As discussed in § 4.4.1, metal nanoparticles are characterized by **a lower work function** than the corresponding homogeneous metal surface. This influences directly the total photoemission yield, as is visible, for example, in Figure 4.23.

2. As discussed in § 3.3.2, the **escape function** from rough surfaces T_R is larger than the corresponding function T_S for smooth surfaces. This results in a further enhancement of the photoemission signal from rough surfaces.

3. The illumination of a rough surface by laser light with optical frequencies excites **LSP's** in the roughness features. This does not happen on a smooth surface. The excitation of LSP produces near zone fields with high intensities and a strong spatial dependence (§ 3.2.4). The behavior of the NZ fields is responsible for the enhancement of the two-photon excitation probability in rough films (§ 3.3). This enhancement has been expressed in equation (3.37) through the ratio $P_R^{(2p)}/P_S^{(2p)}$ between the electron distribution probability following 2PPE for smooth and rough surfaces.

Ag nanoparticles. Figure 4.28 (a) compares the total 1PPE yield with the total 2PPE yield of region 2 to 5 in Figure 4.15. The total yield has been evaluated by taking the average yield of every region from the line scans in Figure 4.16 and scaling this value with the effective coverage of the

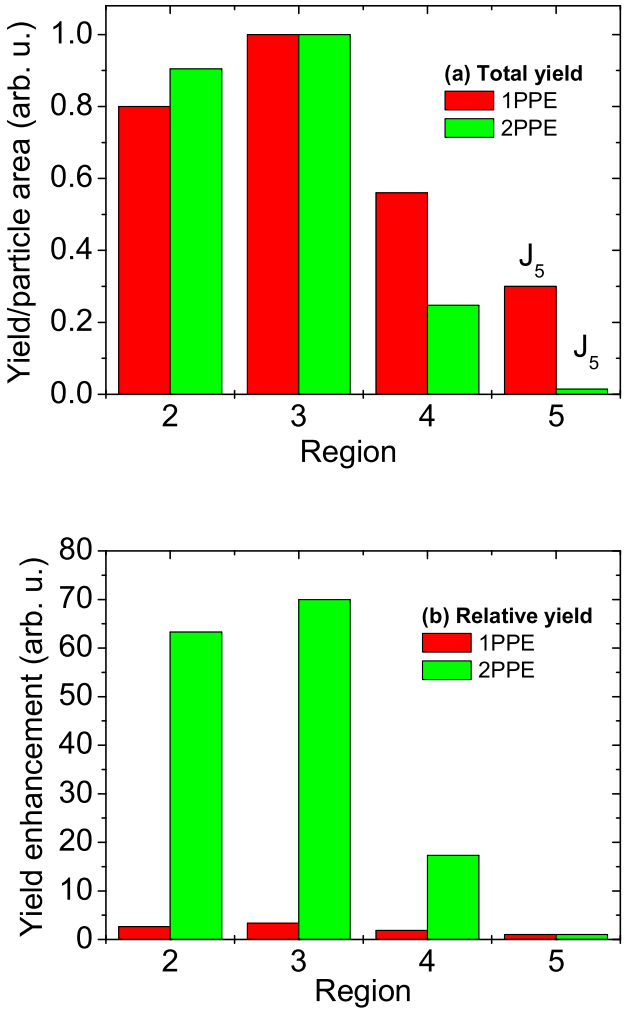

Figure 4.28: (a) Comparison of the total photoemission yield (maxima normalized to unity) for 1PPE and 2PPE of region 2 to 5 of Figure 4.15. The total yield read from Figure 4.16 has been scaled with the effective coverage of the substrate of every region. (b) Comparison of the photoemission yield for 1PPE and 2PPE of region 2 to 5 of Figure 4.15, relative to the yield J_5 of the Ag continuous layer, region 5.

substrate[6]. The 1PPE and 2PPE yield show the same qualitative behavior. In particular, the yield from the Ag nanoparticles is in both cases (1PPE and 2PPE) larger than the yield from the Ag continuous layer (region 5). This is due to the discussed factors 1 and 2, i.e. the difference in the work functions and in the escape functions. In fact, these factors determine the enhancement of the one-photon photoemission yield in the Ag nanoparticle films with respect to the Ag continuous layer as well.
Figure 4.28 (b) compares the 1PPE and 2PPE photoemission yield enhancement of regions 2 to 5 in Figure 4.15, with respect to the yield J_5 of the Ag continuous layer, region 5. It may be used to give a rough estimation of the ratio T_R/T_S. To do this, we argue as follows. The total 1PPE yield $J_{S,R}^{(1p)}$ is given, in analogy with equation (3.32), by the product of three factors[7]: the distribution probability following one-photon excitation $P_{R,S}^{(1p)}$, the transmission function t and the escape function $T_{R,S}$. If we assume $P_R^{(1p)} \simeq P_S^{(1p)}$[8], i.e. the photoexcitation probability through one-photon absorption to be the same in the smooth and rough Ag films, it holds:

$$\frac{J_R^{(1p)}}{J_S^{(1p)}} \simeq \frac{T_R}{T_S} \ . \tag{4.7}$$

This means that we can read the value of the ratio T_R/T_S directly from the 1PPE data in Figure 4.28. For example, for Region 3 it is $T_R/T_S \approx 3$.
Figure 4.28 (b) makes clear that the relative yield enhancement in the Ag nanoparticles is much larger for 2PPE than for 1PPE. The decisive effect that explains this fact is the excitation of LSP in the nanoparticles, that takes place only for illumination with the laser. The important role of LSP excitation played in the total 2PPE yield enhancement is confirmed by the behavior of the Ag sample described in § 4.3.4. As discussed, after cesium deposition the work function lowering of the Ag continuous layer (region F) was two times larger than the work function lowering of the nanoparticle film of region D. This caused a higher 1PPE yield from the Ag continuous layer with respect to the nanoparticle films after cesiation. On the other hand, the 2PPE yield after cesiation, was much more enhanced in the nanoparticle

[6]Remember: region 2 = 20 nm radius particles with 10% effective coverage, region 3 = 25 nm radius particles with 20% effective coverage, region 4 = 40 nm radius particles with 50% effective coverage, region 5 = continuous Ag layer with 80% effective coverage.

[7]Note that the Ag nanoparticle spectra are only 0.1 eV wider than the spectrum of the Ag continuous layer. In the following arguments we will thus ignore this small difference.

[8]This assumption is justified by the fact that with UV-light illumination no LSP excitation occurs, and the photoemission mechanism in rough and homogeneous surfaces should be the same.

films. This confirms that LSP excitation in the Ag nanoparticles is the main reason for the observed 2PPE yield enhancement.
At LSP resonance, the ratio $P_R^{(2p)}/P_S^{(2p)}$ expressed in equation (3.37) assumes high values. It contains two important contributions:

- the third power of the quality factor Q_f of the dipolar LSP resonance (see § 3.2.4), which takes into account the enhancement of the NZ fields due to the LSP resonance;

- a term that accounts for the decisive role of indirect electron transitions, that take place only in rough surfaces due to the strong spatial dependence of the NZ fields and normally dominate in number on the indirect transitions.

We should notice that the theoretical value of the LSP resonance in Ag spherical particles in vacuum is $\hbar\omega^*_{LSP}(Ag) = 3.5\,\text{eV}$ (see equation (3.18)). For Ag nanoparticle films on SiO_2 extinction curves with maxima shifting from 3.4 to 3.0 eV with increasing coverage have been measured [Höv93, Kre95]. Since the resonance curves have a width of about 0.7 eV, our photon energy, here 3.1 eV, was always within the region of enhanced extinction due to the vicinity of the LSP resonance. In this region a strong enhancement of the 2PPE yield has been previously observed, for example in [Leh00].
Using (3.32) and (3.44) for the total photoelectric yield $J_S^{(2p)}$ and the corresponding quantity for rough surfaces $J_R^{(2p)}$, we can express the 2PPE enhancement G in the form:

$$G \equiv \frac{J_R^{(2p)}}{J_S^{(2p)}} \sim (T_R/T_S)(P_R^{(2p)}/P_S^{(2p)}) \; . \tag{4.8}$$

We now use (4.8) to estimate the quality factor Q_f for the Ag nanoparticle of Region 3. Let us first rewrite (3.37):

$$\frac{P_R^{(2p)}}{P_S^{(2p)}} \approx f(R_s)Q_f^3(R_s)\left(\frac{a}{R_s}\right)^2\left[\frac{2V_G}{\hbar\Gamma_{mm}} + \left(\frac{R_s}{a}\right)^3\right] \; . \tag{4.9}$$

Taking for the light penetration depth $R_s \approx 10\,\text{nm}$ (see Appendix D), for the Ag lattice constant $a = 0.409\,\text{nm}$, we have $(R_s/a)^3 \approx 10^4$. Depending on the value of the lifetime $(\Gamma_{mm})^{-1}$, the factor $2V_G/\hbar\Gamma_{mm}$ can have approximate values in the range of 10^2 to 10^4 [Sha96]. Accordingly $(R_s/a)^3 \geq 2V_G/\hbar\Gamma_{mm}$. Since the light penetration depth is of the same order of magnitude as the nanoparticle sizes, we take for the occupied volume fraction $f(R_s) \approx 0.2$.

Using these values in (4.9) together with $T_R/T_S \approx 3$ and $G \approx 17$ we obtain a quality factor of $Q_f \approx 1$.
The obtained value is more than an order of magnitude smaller than expected. In fact, in § 3.2.4 we reported the value $Q_f \approx 50$ for Ag spherical nanoparticles with radius size between 5 and 50 nm; similarly, for rough Ag film modelled as a fractal with roughness features with linear size comparable to R_s, Shalaev *et al.* use in [Sha96] the value $Q_f \approx 24$. There are two possible reasons for the above inconsistency:

- Equation (4.9) has been derived in [Sha96] by modelling a rough surface as a fractal distribution of small polarizable elements. From the AFM images presented in Figure 4.14 it is difficult to make conclusions about the possible fractal geometry of our sample. It is known from literature [Chi91, Dou95, Bar95] that rough thin films (formed for example by condensation of an atomic beam on a low-temperature substrate) are typically fractal structures. They are characterized by the fact that inhomogeneities of all sizes are present, within a certain size interval, according to a power law distribution[9] (see equation (3.38)). In principle, we can not exclude that the Ag nanoparticle films described in § 4.3 consist of a fractal aggregate of Ag inhomogeneities with linear dimensions smaller than the estimated mean size and not resolved in the AFM images.

  Let us assume the above hypothesis to be true and use the value $Q_f = 24$ in (4.8) and (4.9) to estimate $f(R_s)$. We obtain $f(R_s) \approx 10^{-3}$, which is a reasonable value[10]. The fact that $f(R_s) \approx 10^{-3}$ for the nanoparticle film of region 3 would imply that the volume fraction of nanoparticles with linear dimensions in the order of $R_s \approx 10$ nm is only 10^{-3}. From the definition of $f(R_s)$ in (3.39), it follows that the rest of the nanoparticles should have larger dimensions.

  To verify the correctness of the fractal hypothesis further studies are necessary. For example, it would be very interesting to measure the spectral dependence of the scattering coefficient of the Ag sample over a wide spectral range. As underlined in § 3.2.4, fractal surfaces provide optical enhancement within a large spectral interval (from near UV to far infrared), while a 3D compact structure of small metal spheres would be characterized by a much narrower collective resonance. This different behavior would allow us to unambiguously characterize the structure of a nanoparticle film.

[9] Such fractal structures are called *self-affine*.
[10] In [Sha96] values of f between 10^{-1} and 10^{-3} are reported.

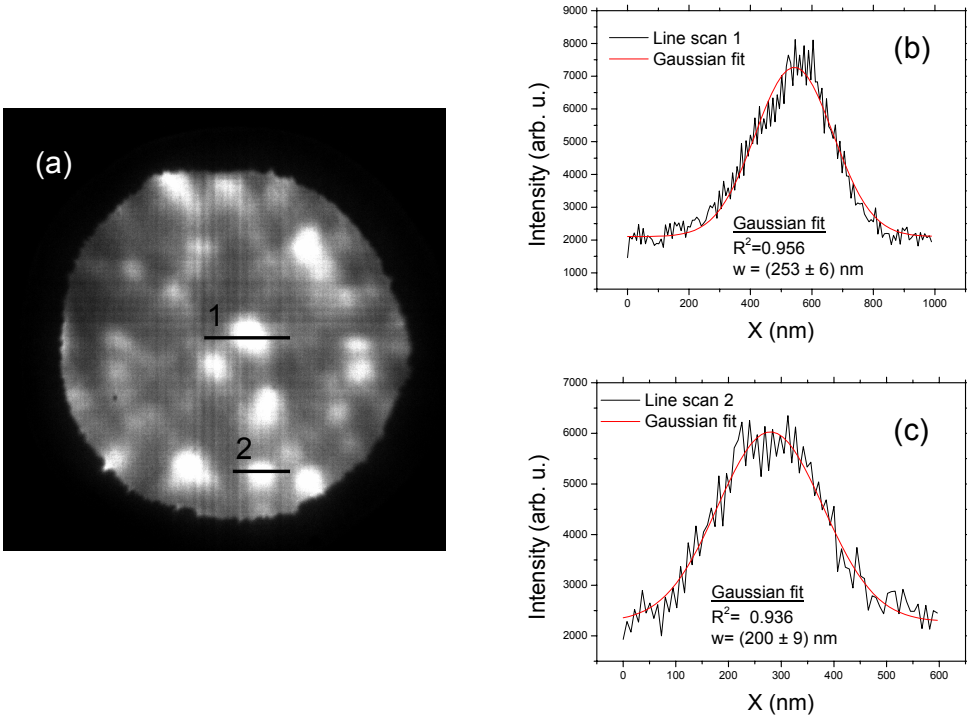

Figure 4.29: (a) PEEM image of a 4 μm part of the continuous Ag layer (region 5) taken by illumination with laser light ($\hbar\omega = 3.0$ eV, s-polarized). (b) and (c) Line scans along the lines marked with 1 and 2 in (a). The hot-spot-like inhomogeneities visible in the PEEM image have apparent linear dimensions that range between 200 nm and 300 nm.

- The continuous layer (region 5) is actually not completely homogeneous. This is easily discernible in the AFM image of Figure 4.14 (d). It shows that the continuous layer is constituted of large coalescence islands. However, we can not exclude that in some of these islands LSP excitation occurs. This would of course decrease the value of G in (4.8) and consequently the value of the estimated value of Q_f. Figure 4.29 (a) shows a high-resolution PEEM image of a 4 μm region of the Ag continuous layer illuminated by the laser ($\hbar\omega = 3.0$ eV, s-polarization). The presence of hot-spot like inhomogeneities on the surface with apparent linear dimensions between 200 nm and 300 nm confirms our hypothesis (see line scans in Figure 4.29 (b) and (c)). Obviously, the intensity of our reference spectrum 5 in Figure 4.18 is already enhanced by hot-

spot like contributions in the continuous Ag film. It is important to note, however, that the contribution of hot-spots is smaller in Figures 4.15 (b) and 4.18 (taken with p-polarized radiation) than in Figure 4.29 (taken with s-polarized radiation). This is connected with the special polarization dependence of hot-spot emission [Sch01b].

Cu hot-spot-like inhomogeneities. As reported in § 4.2 and § 4.4.1, the typical spectra of Cu surface inhomogeneities show a left-hand cutoff shifted by 0.3 to 0.5 eV to lower final state energies relative to the spectrum of the homogeneous surface. This difference is larger than the 0.1 eV in the case of the Ag nanoparticle films. For Cu, the effect of the reduced work function must be taken into account. Let us integrate the Cu hot-spot spectrum of Figure 4.12 in the energy interval $5.2 - 6.8\,\mathrm{eV}$, i.e. starting from the lowest energy of the electrons emerging from the Cu homogeneous surface, see Figure 4.30. We call this value $J'_R(Cu)$, to distinguish it from the total photoemission yield $J_R(Cu)$. The 2PPE enhancement G' obtained as:

$$G' = \frac{J'_R}{J_S} \tag{4.10}$$

has the value $G'(Cu) \approx 10$. Compared with $G(Cu) = J_R(Cu)/J_S(Cu) \approx 16$, the obtained value suggests that the increased width of the hot-spot spectra does not fully explain the measured enhancement $G(Cu)$.
Moreover, if we assume that $T_R/T_S \approx 3$ (as in the case of Ag), we conclude that the enhancement of the NZ fields at the surface inhomogeneities must play here an important role, too. There is, however, an important difference between this case and the discussed NZ field enhancement in the Ag nanoparticle films. In fact, we are dealing here with an **isolated** surface inhomogeneity. To explain the enhancement in the 2PPE yield we have to assume that the electrons in the Cu hot-spot absorb a photon from the NZ field of the particle itself, which is not known. Alternatively, the electron emission proceeds through non-radiative decay of the collective excitation, a process that is quantitatively not understood.
An interesting quantity for this situation is, of course, the absorption efficiency Q_{abs}. We recall that, by definition, $Q_{abs} > 1$ implies that the distortion of the incoming plane wave at the small metal particle surface results in the absorption of all photons out of an increased "effective"particle cross section [Mes81]. Figure 3.13 shows that for a Cu spherical particle with $R = 100\,\mathrm{nm}$ immersed in water $Q_{abs}(\lambda = 400\,\mathrm{nm}) \approx 1.6$. Note that $Q_{abs} > 1$ even out of the LSP resonance.
The resonance of LSP in Cu spherical particles in vacuum is $\hbar\omega^*_{LSP}(Cu) = 2.1\,\mathrm{eV}$ (see (3.19)). This value is of course quite far from the used photon

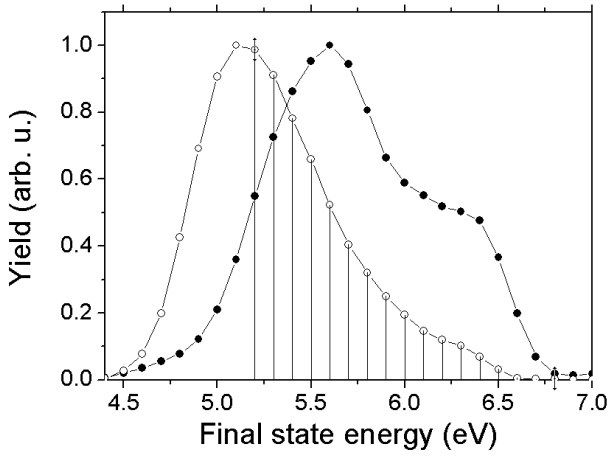

Figure 4.30: Spectra of the homogeneous Cu layer (filled circles) and the Cu hot-spot-like inhomogeneity (empty circles) ($\hbar\omega = 3.3\,\mathrm{eV}$, s-polarized). The vertical lines indicate the energy range where the latter spectrum has been integrated to obtain the quantity $J'_R(Cu)$ discussed in the text.

energy ($\hbar\omega = 3.3\,\mathrm{eV}$). If we assume that the hot-spot consists of a single Cu surface inhomogeneity on a Cu substrate, the only shift and broadening of the resonance frequency may come from its dimensions and irregular shape. More precisely:

- for a radius $R = 200\,\mathrm{nm}$ one expects **retardation effects** to shift the resonance frequency to the red, i.e. away from our laser frequency (see Figure 3.9);
- for **irregular shapes** very large shifts (generally towards the red) and splitting of the resonance are expected.

Without further measurements we can not determine wether the laser frequency was in resonance with the LSP. The above considerations are rather against this hypothesis. This may explain why the 2PPE yield enhancement relative to the homogeneous surface is much more pronounced in the Ag nanoparticle films than in the Cu hot-spots (up to 70 times in Ag against 16 times in Cu). Moreover, in § 3.2.3 it was pointed out that extinction spectra show that Ag spheres in vacuum have a better developed LSP than Cu spheres because of the smaller damping.
To conclude, the above considerations suggest that even if **LSP are not excited** in the Cu hot-spot, but if the laser frequency is in a region where

the **absorption efficiency** of the particle is larger than one, then the photoemission yield is still enhanced. This is due to the fact that synchronous collective excitation of the electrons in the metal particle produces intense NZ fields that affect the 2PPE yield in the same way as the NZ fields produced by the excitation of LSP. The difference between these two situations is that in the case of LSP excitation, the frequency of the electron oscillations corresponds to a natural mode of the system (see § 3.2.2): in this case the field enhancement is much stronger.
A direct evidence of the NZ influence on 2PPE will be given in § 4.6, where a sample with known NZ field behavior has been studied.

4.4.3 Behavior at the Fermi level onset

We now address result (iii), i.e. the behavior of the spectra at the Fermi level onset. Figure 4.31 compares the behavior at E_F of the spectra from the homogeneous Cu crystallite and the hot-spot (a) with the one from the Ag homogeneous layer and the Ag nanoparticle film of region 3 (b). As anticipated, the Fermi level onset of the nanoparticles is enhanced, slightly broadened and shifted to lower final state energies.
To quantify the enhancement, we integrate[11] the Cu spectra between 6.2 and 6.8 eV final state energy and the Ag spectra between 5.8 and 6.4 eV (the integration ranges are marked in Figure 4.31). We obtain that the Cu hot-spot integral yield close to E_F is about 4 times larger than the one from the homogenous crystallite. For the Ag nanoparticles in region 3, the enhancement factor is about 8. Scaled with the coverage ratio (80 % vs. 20 %) this corresponds to a factor of 32 for the Fermi edge signal enhancement of a particle in region 3 compared to that of an area with equal lateral size in the continuous layer. The enhancement in the region of the Fermi level onset is thus significantly less than the factor of 70 for the total intensity enhancement. The same holds for Cu, with an enhancement of about 4 at E_F compared to a total enhancement of 16. This difference, together with the slight broadening of the Fermi edge, is part of result (iv) and is discussed in § 4.4.4.
We now discuss the shifts of 0.13 eV and 0.12 eV towards lower final state energies of the Fermi level onset in the Cu and Ag nanoparticle spectra, respectively, in comparison with the Fermi level onset of the continuous layers. They can be explained using the "final-state cluster charge model" of Wertheim *et al.* [Wer83, Wer88].
As shown in Figure 4.32, during the photoemission process a unit positive

[11] Obviously, for this evaluation the spectra have been taken with their original intensity.

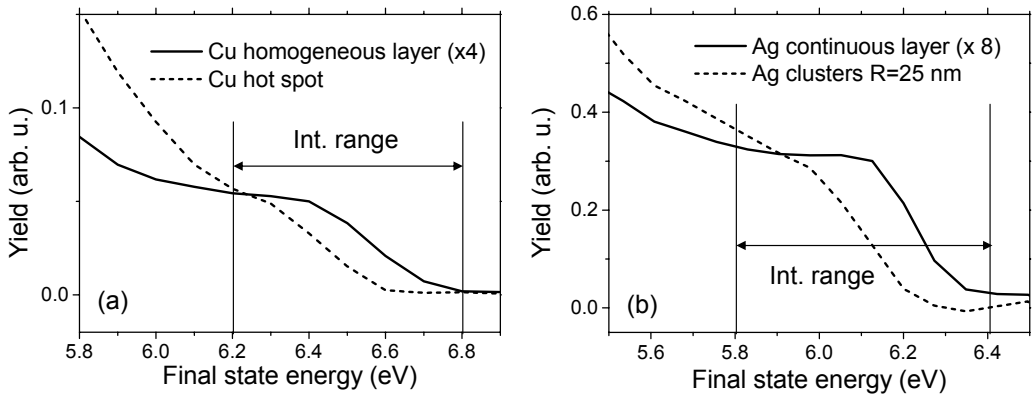

Figure 4.31: (a) Spectra from the homogeneous Cu crystallite (full line, scaling factor 4) and the hot-spot (dashed line). (b) Spectra from the Ag homogeneous layer (full line, scaling factor 8) and the Ag nanoparticle film of region 3 (dashed line). The vertical lines indicate the integration range used to evaluate the total 2PPE yield close to E_F (see text).

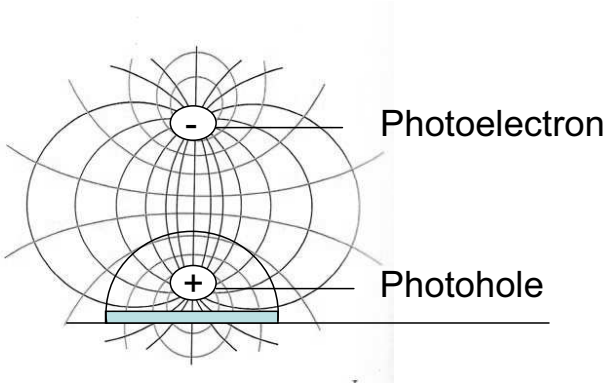

Figure 4.32: Schematic representation of the "final-state cluster charge model" of Wertheim *et al.* [Wer83, Wer88]. One positive unit charge (photohole) resides on the cluster surface during the time scale relevant for photoemission. The resulting Coulomb attraction with the photoelectron decreases its final state energy by $\sim e^2/R$, where R is the cluster radius.

charge can remain localized on a nanoparticle supported by a poorly conducting substrate like carbon or a semiconductor. In this case charge neutralization happens on a time scale longer than the intrinsic time scale of photoemission (about 1 fs, [Wer88]) but long before the next photoemission process from the given particle ($> 12\,\mathrm{ns}$). At our experimental conditions a nanoparticle cannot emit more than one photoelectron per laser pulse. This is evident from the total intensity values and the experimental count rate[12]. Thus there is no long-term charge build-up like on insulators. Instead, a transient state with one positive charge located on the surface of the particle exists. The Coulomb energy of this transient, non-neutralized state of the particle leads to a corresponding reduction of the final state energy of the outgoing photoelectron, fulfilling the energy balance equation of photoemission. The resulting shift of the Fermi level onset ΔE_F depends on the characteristic time τ_n for the positive charge neutralization [Höv98]. In the limit $\tau_n \longrightarrow \infty$ it holds: $\Delta E_F \sim e^2/R$, for spherical metal clusters.
Using for the shift ΔE_F the measured value of 0.1 eV, we obtain a rough estimate for the particle radius $R \approx 15\,\mathrm{nm}$. This value is of the same order of magnitude of the Ag nanoparticle sizes. Thus, we can consider this explanation valid for the Ag nanoparticle films. The Cu hot-spot appears an order of magnitude larger in the images. However, we have mentioned the problem of the apparent size [Nep02]. In addition, the shape of the Cu cluster could deviate strongly from a spherical shape. Possibly, prolate nanostructures protruding from the surface could exhibit the final-state unit charge effect even if one end of the structure is connected with the underlying metal.

4.4.4 Different overall shape

Finally, we discuss result (iv). The different overall shape of the Cu and Ag cluster spectra with respect to the corresponding spectra of the homogeneous surfaces gives information about the different dynamics of 2PPE in the small metal clusters with respect to the homogeneous metal surface. Table 4.5 recalls the most important data. It makes clear that the Cu and Ag nanoparticle spectra are characterized by a steeper increase of the 2PPE yield at low final state energies (J^{max}) compared to the homogeneous surfaces.
The description of two-photon excitation as a two-step process, where a first (pump) photon creates a non-equilibrium distribution which is probed by a second (probe) photon, is justified whenever the sum frequency ω' of the two photons is far away from ω_{LSP} [Tim04]. At our experimental conditions

[12] For our laser fluence of $6.4\,\mu\mathrm{J{\cdot}cm^{-2}}$, about $2{\cdot}10^2$ photons per pulse shine on a spherical cluster with 25 nm radius. Combined with the maximal experimental count rate of 100 kHz, this gives about $2 \cdot 10^{-5}$ electrons emitted per photon pulse and per cluster.

	Enhancement close to E_F	**Enhancement at J^{max}**	**Total enhancement**
Cu	4	20	16
Ag	32	80	70

Table 4.5: 2PPE yield enhancement close to the Fermi level onset E_F, at the maximum yield J^{max} of the 2PPE spectra and of the total yield (area below the spectra) of the Cu hot-spot and the Ag nanoparticles of region 3 compared to the corresponding homogeneous/continuous layers.

($\hbar\omega' = 2\hbar\omega \approx 6\,\text{eV}$) this is always the case, since $\hbar\omega_{LSP}$ for Ag and Cu nanoparticles lies between 2 eV and 4 eV. We now use this illustrative picture to describe the dynamics of a 2PPE process in Cu and Ag homogeneous surfaces and in the corresponding clusters.

Homogeneous Cu and Ag surfaces. In our experiments, the photon momentum of the incident light q is negligible with respect to the electron momentum k. In fact for $\hbar\omega' \approx 6\,\text{eV}$ one has $q \approx 3 \cdot 10^5\,\text{cm}^{-1} \ll k_F$, where k_F is the momentum of electrons at the Fermi level that is of the order of $10^8\,\text{cm}^{-1}$ for most metals. This implies that 2PPE is dominated by **direct transitions** ($\Delta k = 0$). As discussed in § 3.3.1, in a homogeneous Ag or Cu flat surface direct transitions proceed mainly **through virtual intermediate states**. Thus, simultaneous excitations are much more probable. In simultaneous 2PPE transitions there is no time-delay between the absorption of two photons: this means that the probe photon is absorbed from the nascent non-thermal distribution produced by the absorption of the pump photon from the laser field. This process is schematically depicted in Figure 4.33.

Cu and Ag nanoparticles. In Cu and Ag clusters, the pump and probe photon are absorbed out of the enhanced NZ field of the particle (or a neighboring one), or results directly from the decay of the collective mode into a single electron-hole pair. As discussed in § 3.3.2, the strong spatial dependence of the NZ fields allows 2PPE to proceed via **indirect transitions** ($\Delta k \neq 0$) **through real intermediate states** as well. Thus, both simulta-

neous and cascade (sequential) excitations are possible. In a sequential excitation the intermediate state population experiences an energy-dependent relaxation process, mainly due to electron-electron scattering and according to equation (3.45). The typical lifetimes of this intermediate population range from about 2 fs [Bau02] at its high-energy end to several hundreds of fs close to E_F [Sze64]. Note that the term population refers to the statistical average of many single electron excitations and not to an ensemble in one particle. The probe photon is then absorbed within the FWHM of the laser pulse ($\sim 200\,\mathrm{fs}$), as schematically depicted in Figure 4.34. The relaxation of the intermediate population during this intrinsic time delay causes a stronger reduction of the 2PPE yield at higher energies than at lower energies. This explains the differences in the shape of the spectra.
Note that the second photon probes a transient, *partly* thermalized distribution that still deviates from a Fermi distribution, because not all conduction electrons have participated in the thermalization process. Fann *et al.* [Fan92] call the part above E_F the *hot tail*.

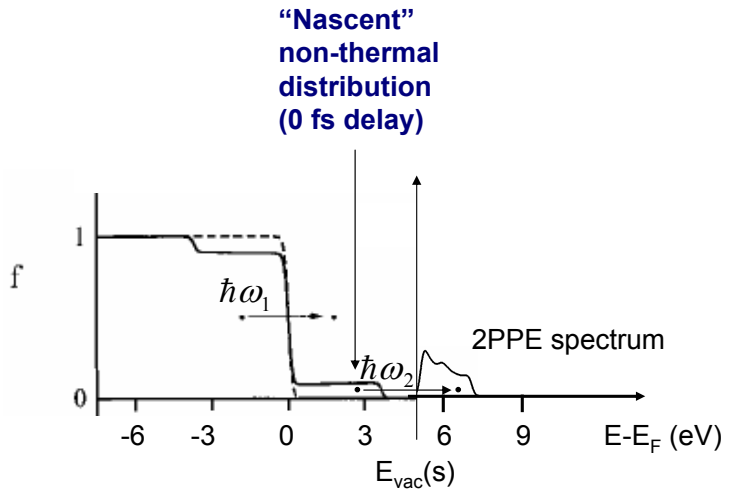

Figure 4.33: Dynamics of 2PPE in a Cu or Ag homogeneous layer. 2PPE proceeds via simultaneous excitations through a virtual intermediate state. The virtual states are populated by the electrons excited by the first photon $\hbar\omega_1$. The second photon $\hbar\omega_2$ is immediately absorbed from the "nascent" non-thermal distribution created by the first photon (0 fs delay).

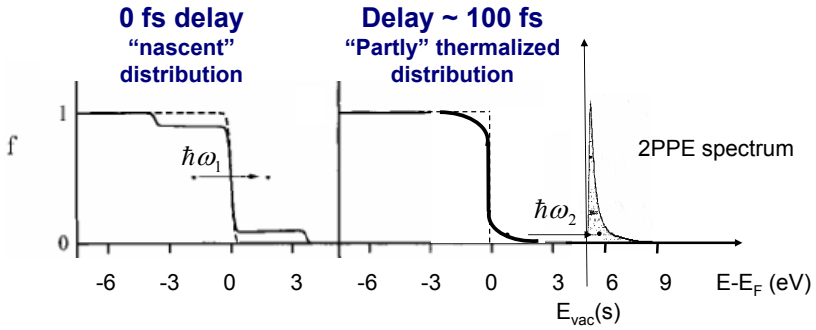

Figure 4.34: Dynamics of 2PPE in a Cu or Ag nanoparticle. 2PPE may proceed via cascade excitations through a real intermediate state. The real states populated by the electrons excited by the first photon $\hbar\omega_1$ relax according to (3.45). The second photon $\hbar\omega_2$ is absorbed at the time t, which lays within the FWHM of the laser pulse ($t < 200$ fs). Within this delay time, "partial" relaxation of the electron population occurs.

4.4.5 On thermionic emission

At this point we may ask the question whether thermionic emission could contribute to the registered photoemission signal. Such an emission mechanism has been reported for example in [Ken01], where Au nanoparticles have been illuminated by laser light in resonance with LSP excitation (at 2.1 eV) and with high fluence ($1\,\mathrm{mJ{\cdot}cm^{-2}}$). Our TOF PEEM technique is capable of distinguishing between the two processes: 2PPE is characterized by a visible Fermi level onset around the final state energy $2\hbar\omega$, whereas thermionic emission would give rise to a Boltzmann-type energy distribution. The presence of a Fermi level onset in the measured nanoparticle spectra proves that there is a substantial 2PPE contribution, in particular at energies close to E_F. Since multiphoton excitation probability strongly decreases with the order n of the n-photon process, thermionic emission may play an increasingly iportant role by red-laser illumination.
The question if 2PPE is the only electron emission mechanism in small metal clusters is still open. Equation (3.28) shows that within the dipole approximation and for simultaneous excitations, a power law $J \propto I^n$ with $n = 2$ between the electron yield J and the intensity I of the exciting laser is expected. Different authors registered a deviation from this behavior, and reported power laws with fractional exponents n, in general higher than 2 [Fuj84, Sch01b, Fec02, Kor04]. This was taken as a hint that electron emission mechanisms alternative to 2PPE may take place in small metal particles. A full understanding of such behavior is, however, still not achieved.

4.5 Dependence of two-photon photoemission on the laser polarization

In this section we discuss the influence of the laser polarization on 2PPE from homogeneous metal surfaces and small metal particles. This issue has been widely discussed in different works [Sch01b, Sch00, Fec02], where the authors employed a PEEM to observe the 2PPE spatially resolved, however, without energy resolution.

Homogeneous surfaces. The 2PPE yield from homogeneous metal surfaces $J_S^{(2p)}$ is proportional to the squared intensity of the laser beam, see equation (3.28). In this case it holds [Aes95]:

$$J_S^{(2p)}(\alpha) = J_u + J_{0,S}^{(2p)} \cos^4(\alpha) \ , \tag{4.11}$$

where α is the angle between the electric vector and the light propagation direction, i.e. $\alpha = 0^\circ$ corresponds to p-polarized light and $\alpha = 90^\circ$ to s-polarized light. The factor J_u gives the contributions to the photoemission yield that do not depend on the polarization. The $\cos^4(\alpha)$ dependence in (4.11) is responsible for the total photoemission yield difference between s- and p-polarized light illumination. Under the assumption that the total yield $J_S^{(2p)}$ depends on the squared intensity of the non-reflected light, it is possible to write:

$$\frac{J_S^{(2p),p}}{J_S^{(2p),s}} = \left(\frac{1 - R_p(\theta)}{1 - R_s(\theta)} \right)^2 \ . \tag{4.12}$$

$R_p(\theta)$ and $R_s(\theta)$ are respectively the Fresnel reflection coefficients for p- and s-polarized light [Ber87], depending on the complex index of refraction n of the surface material and on the angle of photon incidence θ:

$$R_p(\theta) = \left| \frac{n^2 \cos(\theta) - \sqrt{n^2 - \sin^2(\theta)}}{n^2 \cos(\theta) + \sqrt{n^2 - \sin^2(\theta)}} \right|^2 \tag{4.13}$$

$$R_s(\theta) = \left| - \frac{\left[\sqrt{n^2 - \sin^2(\theta)} - \cos(\theta) \right]^2}{n^2 - 1} \right|^2 \ . \tag{4.14}$$

Figure 4.35 shows the dependence of the ratio $J_S^{(2p),p}/J_S^{(2p),s}$ from the light angle of incidence θ for Cu and Ag homogeneous surfaces, calculated using the respective complex refraction indices $n = 1.18{+}2.21\mathrm{i}$ and $n = 0.73{+}2.11\mathrm{i}$, valid for the photon energy $\hbar\omega = 3.0\,\mathrm{eV}$ [Pal85].

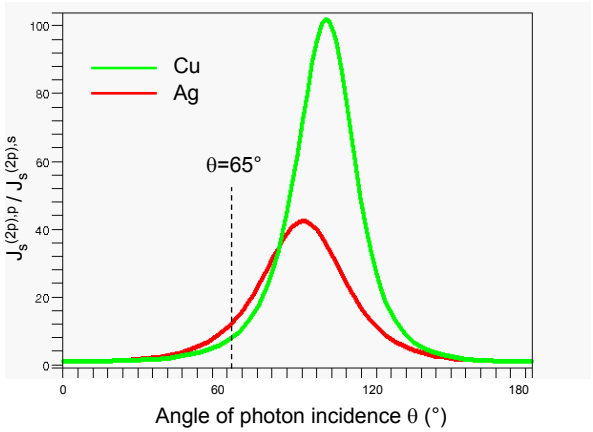

Figure 4.35: Dependence of the ratio $J_S^{(2p),p}/J_S^{(2p),s}$ from the angle of photon incidence θ for Cu and Ag homogeneous surfaces. The indices of refraction $n = 1.18 + 2.21\mathrm{i}$ and $n = 0.73 + 2.11\mathrm{i}$ have been respectively used for Cu and Ag, and correspond to the photon energy $\hbar\omega = 3.0\,\mathrm{eV}$ of the incoming light [Pal85].

The theoretical values of the ratio (4.12) for $\theta = 65^\circ$ are compared in Table 4.6 to the corresponding measured values. To obtain the latter values we evaluated the total photoemission yield from PEEM images of homogeneous regions of the Cu and Ag samples described in § 4.2 and § 4.3, respectively. In the case of Ag the experimental value is smaller than the theoretical prediction of equation (4.12). This is probably due to the fact that, as already

Sample	$J_S^{(2p),p}/J_S^{(2p),s}$, calculated	$J_S^{(2p),p}/J_S^{(2p),s}$, measured
Cu	8.2	12 ± 2
Ag	12.4	1.7 ± 0.5

Table 4.6: Comparison of the value of the ratio $J_S^{(2p),p}/J_S^{(2p),s}$ calculated for Ag and Cu homogeneous surfaces using equation (4.12) with $\theta = 65^\circ$ and the corresponding experimental values. The latter values have been obtained evaluating the total photoemission yield for s- and p-polarized illumination in PEEM images of the homogeneous Cu and Ag samples described in § 4.2 and § 4.3, respectively.

observed in § 4.4.2, the analyzed regions are not perfectly flat and homogeneous. In this case, the presence of inhomogeneities drastically influences the 2PPE dependence on the light polarization, as explained in the following. For Cu, on the other hand, the experimental value is larger than the theoretical value. In this situation, the analyzed Cu crystallites were flat and homogeneous. The higher experimental value can be explained by considering that for s-polarized light the electrons are preferentially excited along the electric vector, i.e. parallel to the surface [Sas75]. Due to refraction at the surface potential barrier, some of the excited electrons cannot escape through the surface potential barrier itself. This reduces the emissivity for s-polarization.

Small metal particles. Figure 4.36 (a) and (b) show laser-PEEM images of the Ag sample described in § 4.3, taken from the Ag film of region 5 (field of view 10μm). (a) and (b) correspond to s- and p-polarization, respectively. Both images show various hot-spots with an enhanced photoemission yield. Figure 4.36 (c) and (d) are obtained respectively by taking the difference (pixel-by-pixel) between the p- and s-polarized images and vice-versa. After subtraction, a constant offset has been added in order to visualize negative intensity values as well. The gray level corresponding to zero intensity appears outside the round images. The same gray level appears in the center of some of the hot-spots (see for example the region marked in (d)). This is due to the fact that in these spots, the original images (a) and (b) are overexposed, leading to identical gray values in the PEEM images. Brighter regions indicate a positive difference, while darker regions a negative difference. The words bright and dark will be used in the following with respect to the offset value.

Let us now discuss Figure (c), i.e. the pixel-by-pixel (p-s)-polarization difference image. As expected, the substrate (underlying Ag thick layer) appears brighter than the offset. The hot-spots have a rather complicated behavior. Most of them exhibit an asymmetrical intensity distribution. A typical object of this kind is marked in (a) with a square.

The photon impact direction is indicated in (a) as well. All the asymmetrical patterns of Figure (c) show their bright side on the right. A detailed analysis of the behavior of the hot-spot marked in (a) is presented in Figure 4.37 (a) and (b). In particular, (a) shows the line scans across the hot-spot for p- and s-polarization. The intensity maxima are shifted by about 150 nm. Figure 4.37 (b) shows the line scan of the (p-s)-polarization image. The enhancement for p-polarization results here in positive values of the difference. The apparent size of the hot-spot is 327 nm.

In [Fec02] it was already observed that the photoemission intensity for p-

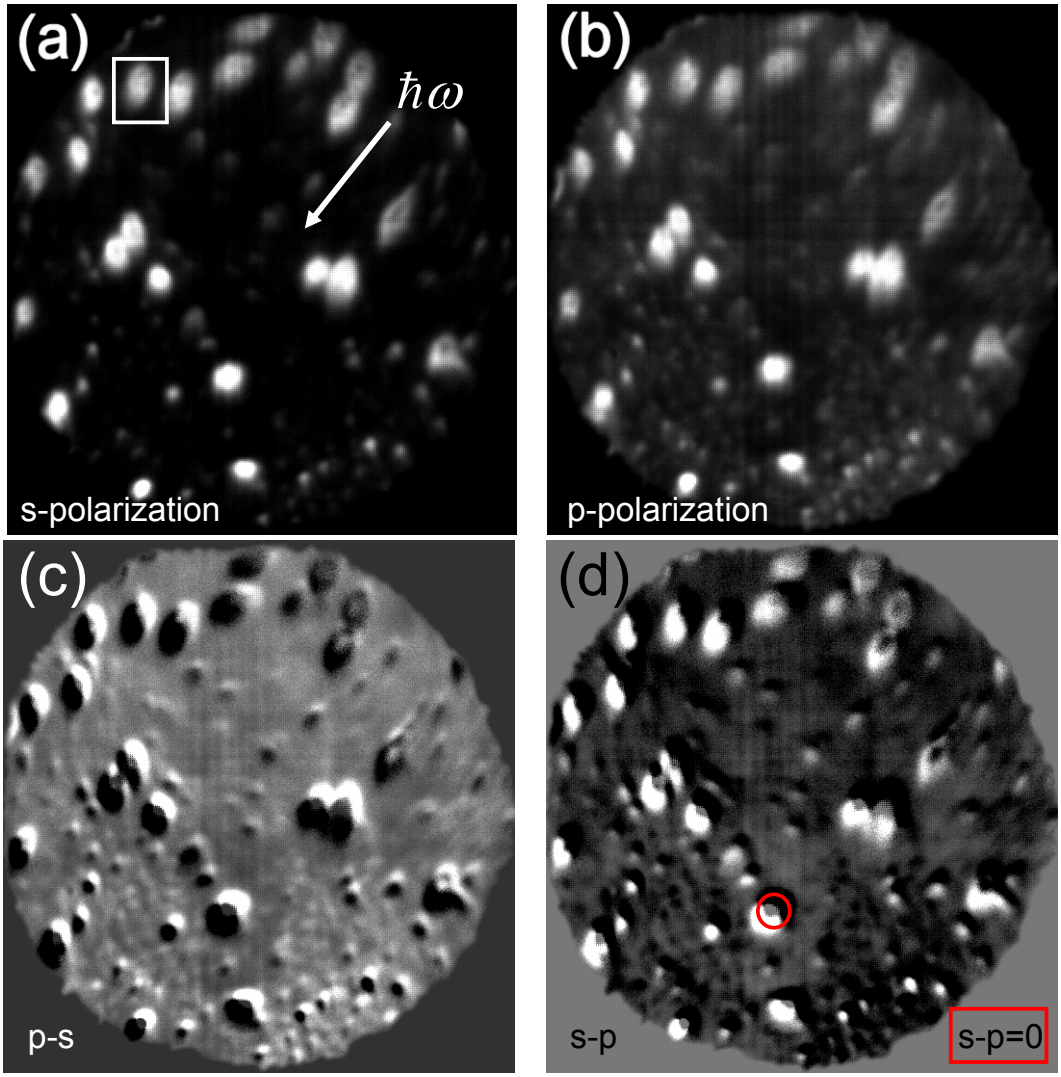

Figure 4.36: Laser-PEEM images ($\hbar\omega = 3.1\,\mathrm{eV}$) of the Ag sample described in § 4.3, taken from an area of the continuous Ag film of region 5. Field of view 10μm. (a) s-polarized laser light; (b) p-polarized light; (c) difference between p- and s-polarization; (d) difference between s- and p-polarization. The arrow in (a) indicates the photon impact direction. In the difference images a constant offset (visible outside the circular images) has been added in order to visualize negative intensity values as well.

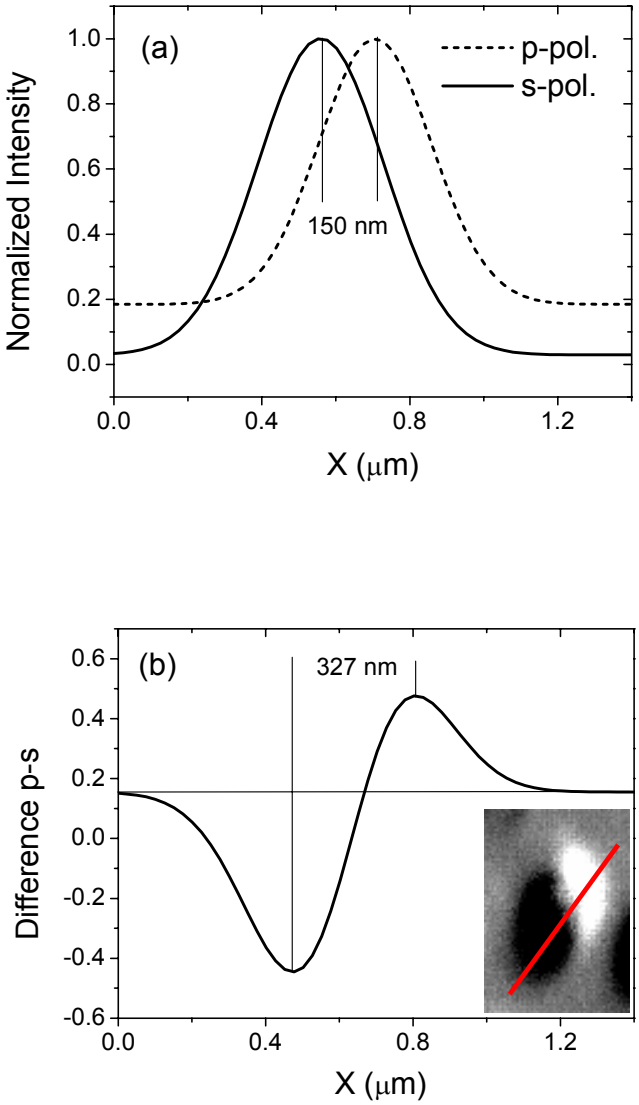

Figure 4.37: (a) Intensity distribution of the hot-spot marked with a square in Figure 4.36 (a). The line scans were taken along the line shown in (b). Full line indicates s-polarization, dashed line p-polarization. (b) Line scan for the same hot-spot taken in the (p-s)-polarization image (Figure 4.36 (c)). The (p-s)-polarization image of the considered hot-spot and the line used for the line scan, are shown in the inset.

polarized light is higher on the photon-impact side. This effect has been explained as a combination of two factors, namely:

- a topographic effect, since normally the side of a 3D object directed towards the illumination source appears brighter (because here the photon density is higher);
- the excitation of LSP in the particles themselves. In particular, s- and p-polarized light may excite different plasmon modes in non-spherical clusters. For example in oblate spheroids, the LSP resonance splits into two modes [Kre93, Sti99]: the (1,1)-mode with dipole along the main axis and the (1,0)-mode along the short axis. Let us now assume the particles to lie on the surface with the short axis directed along the surface normal. In this case, p-polarized light excites both modes , since the electric field has a component along both axes. On the other hand, s-polarized light may excite only the (1,1)-mode. This resonance leads to an essentially homogeneous emission of the entire particle surface.

The above considerations explain qualitatively the behavior observed in Figure 4.36 (c) and (d). However, to obtain a more quantitative description, it would be necessary to know the NZ field behavior for p- and s-polarization. This behavior is mainly connected with the real shape of the nanoparticles. The above considerations suggest that the PEEM technique, if applied to well defined nanostructured materials where the NZ field behavior is known, would allow to determine a direct correspondence between the spatial distribution of the 2PPE yield and the NZ field behavior, and thus could be developed to a very convenient technique to laterally resolve the NZ fields produced by small metal particles. A first step in this direction is described in the next section (§ 4.6).

Comparison of 2PPE spectra taken with different laser polarizations. Figure 4.38 compares the electron energy spectra taken from a Cu homogeneous crystallite and from a Cu hot-spot with p- and s-polarization ($\hbar\omega = 3.3\,\mathrm{eV}$). In particular, in (a) the spectra for the Cu homogeneous crystallite (taken with p- and s-polarization) are plotted in the original intensity scale. As expected, the homogeneous crystallite shows a higher 2PPE yield for p-polarized laser illumination. In (b), the same spectra have been normalized at the Fermi level onset region. This Figure makes clear that the spectra essentially differ only for the different 2PPE yield, but have almost the same shape. In particular, the Fermi level onset and the low-energy cutoff look perfectly identical. The s-polarization spectrum exhibits a significantly higher secondary electron peak at about 5.2 eV. This can be attributed to the

directional behavior of the photoelectrons. The s-electrons are preferentially excited parallel to the surface thus enhancing their scattering probability. Figure 4.38 (c) shows the spectra taken from a hot-spot with p- and s-polarization. In this case, the 2PPE yield is enhanced for s-polarization. Moreover, the spectra show a markedly different behavior:

- the 2PPE total yield from the hot-spot for p-polarized light is a factor of 2 enhanced with respect to the yield from the Cu crystallite with the same polarization. This means that in this case the NZ field is not significantly enhanced for p-polarized light. This fact is reflected also in the same qualitative behavior of the spectra, that are compared in Figure 4.39 (a) (here their maxima have been normalized to unity);

- for s-polarization, the 2PPE total yield from the hot-spot is a factor of 65 enhanced with respect to the yield from the Cu crystallite. Thus, in this case, the NZ field is significantly enhanced. The NZ field enhancement and spatial dependence effect the spectrum of the hot-spot as it is clear from Figure 4.39 (b). In particular, the region of the Fermi level onset is visibly changed in the hot-spot spectrum. We refer to § 4.4 for the discussion of this behavior.

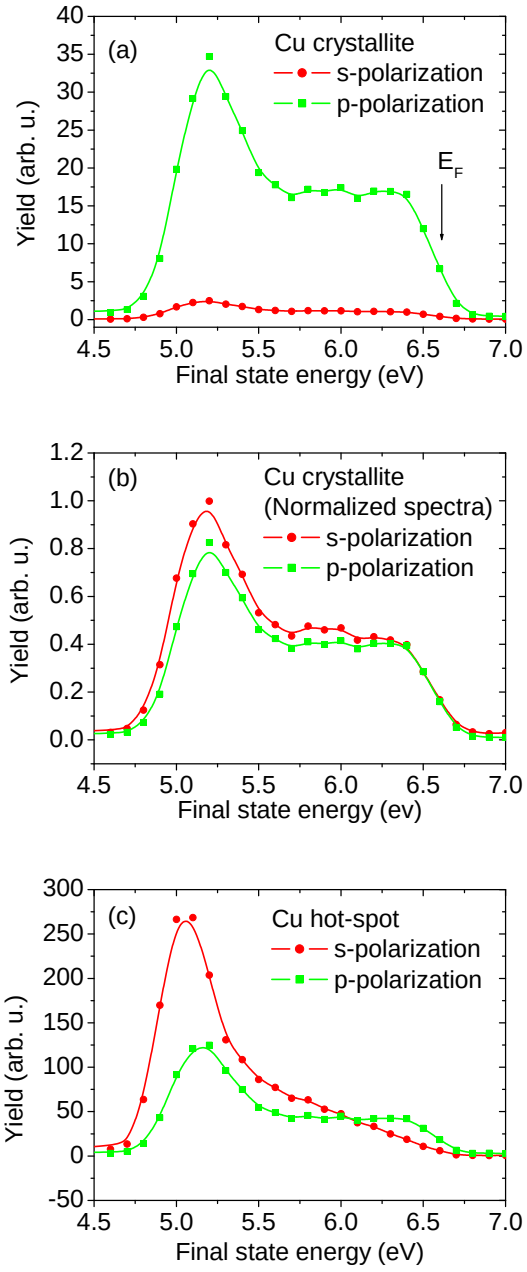

Figure 4.38: (a) 2PPE spectra taken from an homogeneous Cu crystallite ($\hbar\omega = 3.3\,\mathrm{eV}$) for p- and s-polarization. (b) Same as (a) but with the maxima of the spectra normalized to unity. (c) 2PPE spectra taken from a Cu hot-spot ($\hbar\omega = 3.3\,\mathrm{eV}$) for p- and s-polarization. In all the figures, p- and s-polarization are indicated by squares and circles, respectively. (a) and (c) have the same absolute intensity scale.

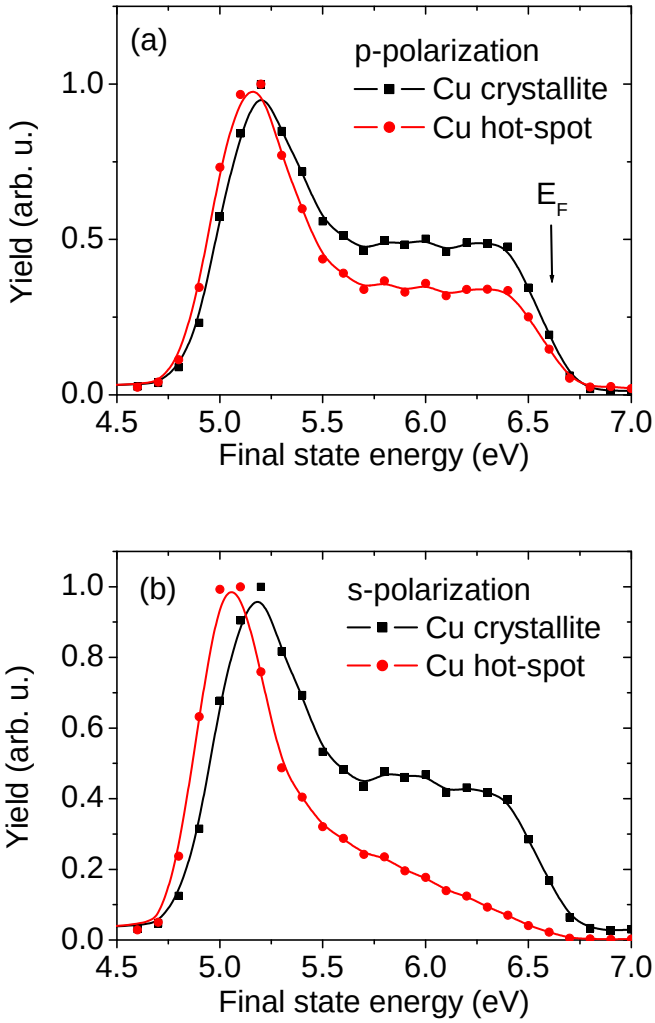

Figure 4.39: Comparison between the 2PPE spectra shown in Figure 4.38, taken with p-polarization (a) and s-polarization (b), for the Cu homogeneous crystallite and the Cu hot-spot. The maxima of the spectra have been normalized to unity.

4.6 Direct evidence of the near zone field in two-photon photoemission

In this section we present an experiment that directly demonstrates the influence of the NZ field behavior generated by small metal particles on 2PPE. The basic idea was to investigate with the PEEM small metal structures, whose NZ field is theoretically predictable, and to compare the analytical solution of the NZ field with the laterally resolved 2PPE signal. We will show that the theoretically predicted spatial dependence of the NZ field can be directly measured.
The sample preparation described in § 4.6.1, together with the theoretical calculation of the NZ field, have been carried out at the *Max Planck Institute for Polymer Research, Mainz*, by Heiko Rochholz, Dr. Jennifer Shumaker-Parry and Dr. Max Kreiter.

4.6.1 Sample preparation and characterization

Figure 4.40 shows the preparation procedure. First (a), polystyrene spheres are deposited on a Si substrate (with its native oxide, SiO_x). Successively, Ag is deposited on the prepared substrate by thermal evaporation, with an angle $\theta \neq 0$ with respect to the sample surface normal. In the next step (b), the sample is sputtered by bombardment with an Ar beam parallel to the surface normal. In this way, part of the deposited Ag is removed from the surface. Since the angles of Ag deposition and ion bombardment differ one from another, moon-like Ag structures remain on the SiO_x surface. Finally, the spheres are removed from the surface. By turning the sample around the surface normal before removing the polystyrene spheres, and evaporating Ag a second time, it is possible to tailor structures with different gaps α (c).
Figure 4.41 shows two Scanning Electron Microscopy (SEM) images of moon-like samples with different gap apertures. The moons' linear dimension is 400 nm. Such structures are of great interest because they should produce a strongly localized NZ field in correspondence of LSP excitation. This is shown in Figure 4.42. It presents the result of a calculation of the NZ field enhancement for a Ag moon-shaped nanostructure for different wavelengths λ of the incoming field (namely, λ = 300, 302, 318, 326, 374 and 412 nm). Different colors correspond to different values of the enhancement factor E/E_0 (from 1 to 100), where E_0 is the incoming field amplitude and E the amplitude of the NZ field.
The Figure shows clearly that for particular values of the wavelength of the incoming light, strong resonances occur. In correspondence of those

resonances, the NZ field shows a variety of different behaviors. For example, at $\lambda = 412\,\text{nm}$ the NZ field is extremely localized at the tips of the moon, with an enhancement factor up to 100. According to the calculations this behavior is almost not polarization-dependent.

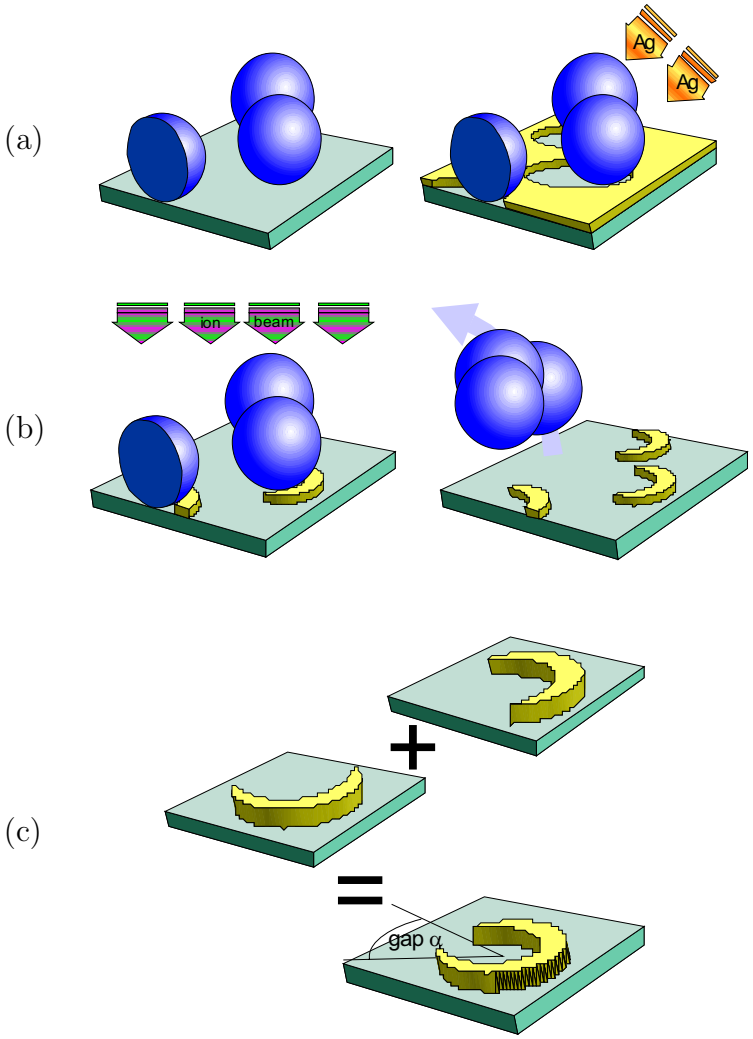

Figure 4.40: Schematic representation of the sample preparation steps for Ag moon-like nanostructures; (a), (b) and (c) are described in the text. Ag moons with different gap apertures α were deposited on a SiO_x substrate. Sample preparation at the *Max Planck Institute for Polymer Research, Mainz.*

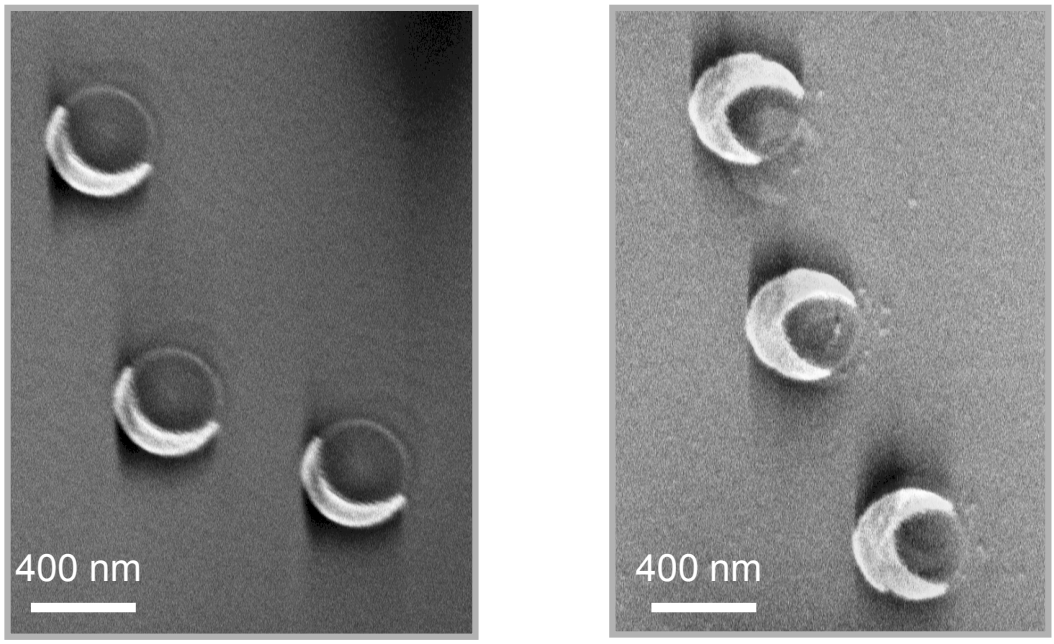

Figure 4.41: Scanning electron microscopy (SEM) images of two Ag moon-like samples prepared with different gap apertures α, see Figure 4.40 (c). The prepared structures are 400 nm in size. Performed at the *Max Planck Institute for Polymer Research, Mainz.*

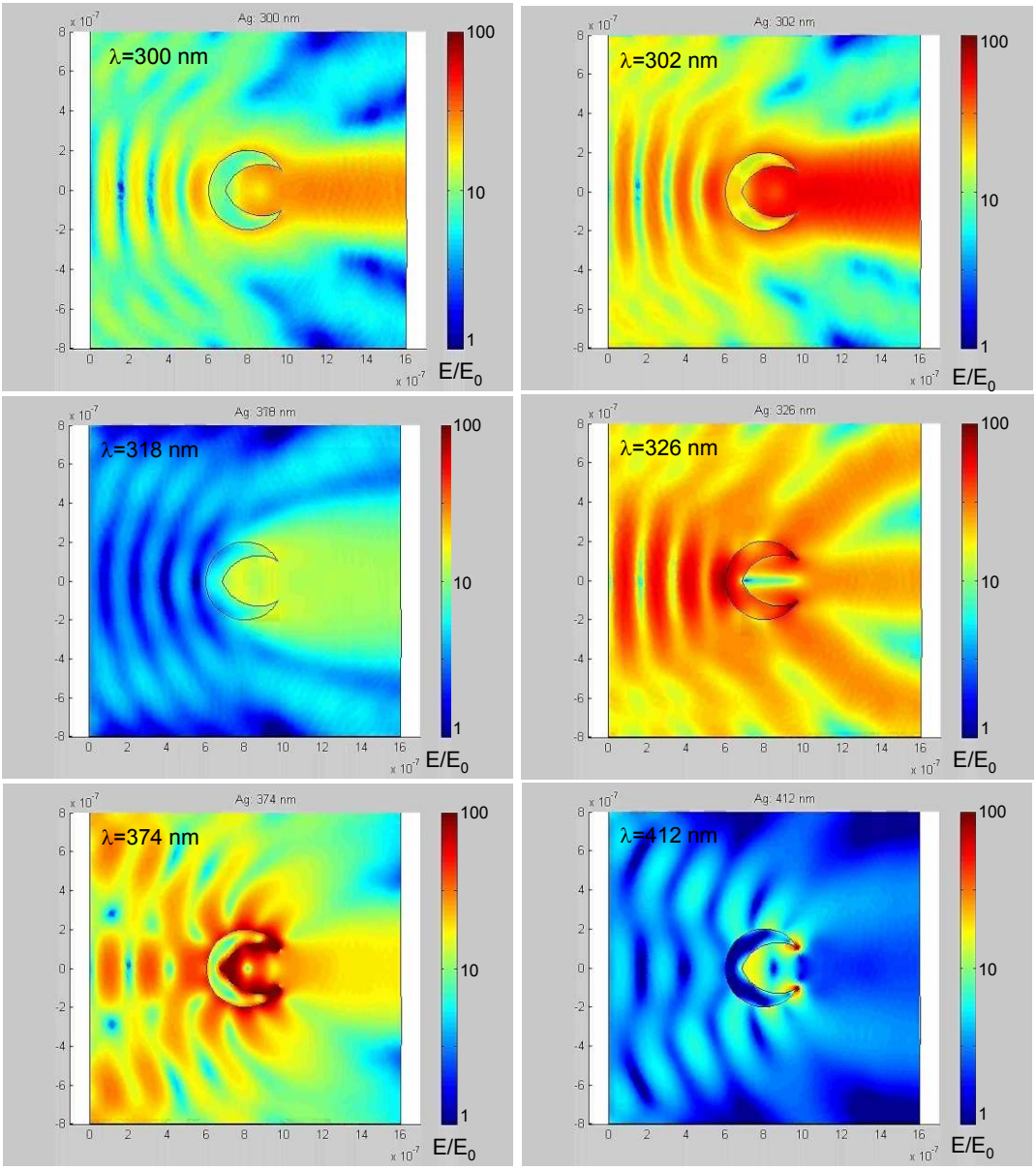

Figure 4.42: Calculation of the NZ field enhancement close to an Ag moon sample, for different wavelengths λ of the incoming light (λ = 300, 302, 318, 326, 374 and 412 nm). The NZ field enhancement is represented on a logarithmic scale (on the right side of every picture), where dark blue corresponds to no enhancement ($E = E_0$), green to enhancement factor $E/E_0 = 10$ and red $E/E_0 = 100$. Calculation performed at the *Max Planck Institute for Polymer Research, Mainz* (courtesy of H. Rochholz).

4.6.2 Experimental results and discussion

We now present PEEM images obtained from an Ag-moon sample with a small gap aperture $\alpha \approx 60^{\circ}$. The sample was illuminated with the Hg UV lamp ($\hbar\omega = 5.8\,\mathrm{eV}$, $\lambda = 220\,\mathrm{nm}$) and afterwards with the blue laser ($\hbar\omega = 3.1\,\mathrm{eV}$, $\lambda = 400\,\mathrm{nm}$, p-polarization). The images were recorded using a standard PEEM imaging unit (see § 2.2.2). Since no resonances should occur for $\lambda = 220\,\mathrm{nm}$, we expect the UV-PEEM images to give information about the topography of the sample. On the other hand, the blue-laser-PEEM images should show a contrast connected to the influence of the NZ field behavior at $\lambda = 400\,\mathrm{nm}$ on the 2PPE signal.

Figure 4.43 shows a UV-PEEM image of the sample (field of view $3\,\mu\mathrm{m}$, exposure time $\Delta t = 200\,\mathrm{s}$) and a laser-PEEM image of the same region of the sample ($\Delta t = 5\,\mathrm{s}$). Five moon-structures are clearly visible in the UV-PEEM image. Comparing the UV-PEEM with the laser-PEEM images, brings to the conclusion that the wavelength of the incoming electromagnetic field drastically influences the photoemission pattern.

The bottom part of Figure 4.43 compares two details in the UV- and laser-PEEM images, corresponding to the same region on the sample. A moon-like structure is visible in the UV-PEEM image. The aperture gap, however, is not clearly recognizable: this is probably due to an imperfection in the preparation procedure, or to the fact that the gap is rather small. The circle indicates the position where the gap is expected to lie. In the laser-PEEM image, the 2PPE yield is enhanced in correspondence of the gap position. On the other hand, the moon-like structure appears dark. Note that the images have been digitally processed to enhance the contrast. In the original laser-PEEM image, the ratio between the intensity of the area marked with the circle and a surrounding darker region (of the same size) is at least a factor of 4.

Comparing the laser-PEEM image with the NZ-field simulation for $\lambda = 400\,\mathrm{nm}$ (shown in the bottom part of Figure 4.43, center panel), it is clear that the 2PPE yield is enhanced in correspondence of the NZ field enhancement. This is clearly visible in the line scans presented in Figure 4.44. In the chosen angular scale, the gap is located approximately between 100° and 170°, see scan of the SEM image. As expected, in this region the scan in the UV-PEEM image shows a low intensity, while the scan in the laser-PEEM image reveals the maximum of the 2PPE intensity.

This experiment is very promising. A systematic study of these structures with TOF-PEEM spectromicroscopy under different conditions (size, shape, material, light polarization, angle of incidence) could bring to find a quantitative relation between the NZ field of a single structure and the 2PPE

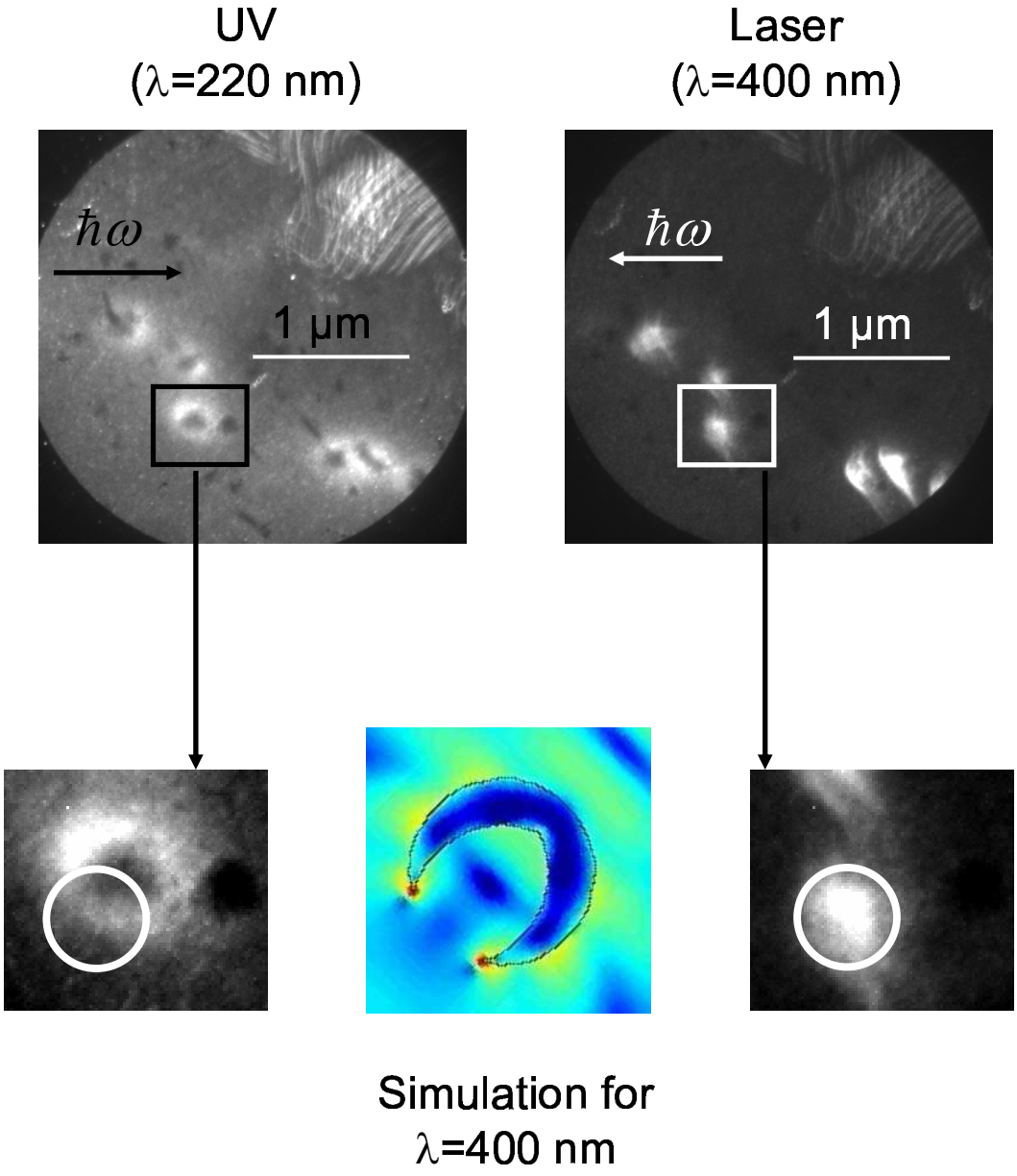

Figure 4.43: High-resolution PEEM images of Ag moon-shaped nanostructures on SiO_x with small aperture gap $\alpha \approx 60°$; field of view $3\,\mu$m. The images have been taken with the standard PEEM imaging unit. Exposure time: UV-PEEM image 200 s; laser-PEEM image 5 s. The arrows indicate the photon impact directions. The bottom left and right panels show in detail a moon-structure imaged with UV-PEEM and laser-PEEM, respectively. For comparison, the result of the theoretical computation for the NZ field at $\lambda = 400$ nm is also shown (center panel). The circles mark the same position on the sample. The different emission patterns visible in the images are discussed in the text. The pattern in the upper right of the topmost panels is an artefact of the screen.

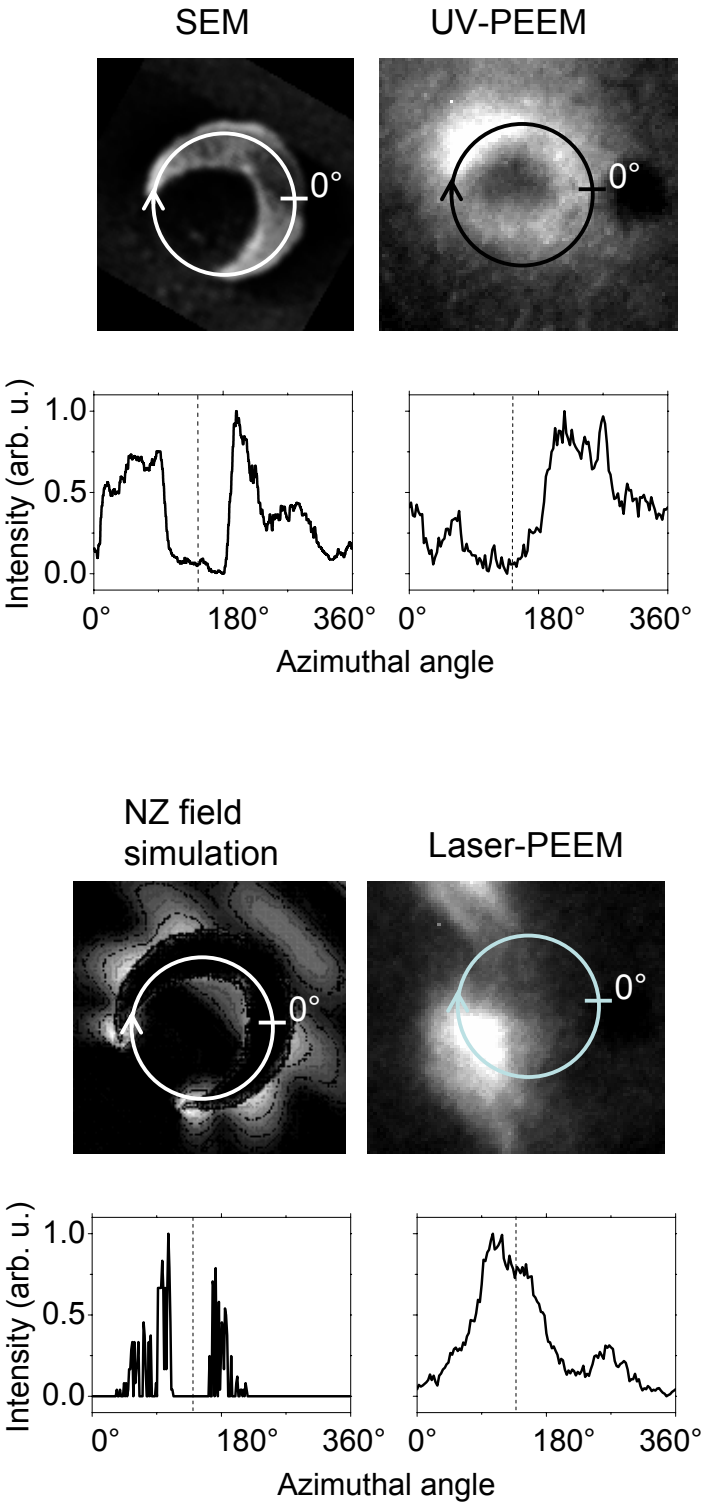

Figure 4.44: Line scans along the circular lines drawn in the SEM image, the UV-PEEM image, the NZ field simulation image and the laser-PEEM image of the Ag moon-like sample. The gap is located approximately between 100° and 170°, its center is denoted by a dashed line.

signal. Moreover, it could make of PEEM a good technique for the direct lateral visualization of the NZ field behavior of nanostructured samples.

4.7 Three-photon photoemission from Ag nanoparticle films on Si(111)

In this section we compare the photoemission from Ag nanoparticle films with different nominal thicknesses, illuminated with the Hg UV-lamp, the blue laser and the red laser beam. As explained in Chapter 3, if the photon energy $\hbar\omega$ is smaller than the local work function ϕ_m, nonlinear photoemission can be generated through a multiphoton process nPPE, where n is the minimum number of photons for which $n\hbar\omega > \phi_m$. For the red laser beam ($\hbar\omega = 1.6\,\text{eV}$) at least three photons are required ($3\hbar\omega = 4.8\,\text{eV} > \phi_m$).

4.7.1 Sample preparation and characterization

The sample consisted of Ag nanoparticle films deposited on a Si(111) substrate, prepared following the procedure described in § 4.3.1. We prepared 5 stripes with nominal thicknesses varying between 0.5 and 15 nm and a thicker Ag layer with a thickness of 50 nm. Every stripe will be numbered progressively from 1 to 5, with increasing thickness. Table 4.7 summarizes the sample specifications. The nanoparticle sizes have been estimated by comparison with the data presented in § 4.3.1. They range from below 20 nm up to 40 nm.

Stripe number	**Nominal thickness (nm)** (±10%)	**Estimated nanoparticle radius R (nm)**
1	0.5	$R_1 < 20$
2	1	$R_1 < R_2 < 20$
3	2	20 ± 4
4	5	25 ± 5
5	15	$25 < R_5 < 40$

Table 4.7: Nominal thickness of the deposited Ag nanoparticle films, numbered for convenience from 1 to 5, and estimated nanoparticle average radii.

4.7.2 Experimental results and discussion

Figure 4.45 shows four PEEM images of a 150 μm wide region of the sample. (a) was taken by UV-light illumination ($\hbar\omega = 5.8\,\text{eV}$, exposure time 2 s). (b) corresponds to blue-laser illumination ($\hbar\omega = 3.1\,\text{eV}$, p-polarization, exposure

time 0.5 s). The films 1 to 5, the 50 nm thick Ag film and the bare Si(111) substrate have been marked. (c) and (d) were taken by red-laser illumination (photon energy $\hbar\omega = 1.5\,\text{eV}$ and $\hbar\omega = 1.6\,\text{eV}$, respectively; exposure time 20 s). The red laser is p-polarized. In all the images, the structure visible on the top-right is a defect on the screen.
Figures 4.45 (c) and (d) are very similar. First of all, only 3 of the 5 deposited films can be recognized in these images (film number 3, 4 and 5). Secondly, no photoemission intensity is registered from the 50 nm thick Ag film and from the bare Si(111) substrate. Finally, different hot-spots can be recognized in the images. The presence of hot-spots on an Ag film deposited on Si(100), and illuminated by a red-fs-laser, was already observed in [Sch02a]. It was attributed to local field enhancement at roughness features.
It is interesting to note that upon changing the photon energy by just 0.1 eV, the intensity of one hot-spot may drastically change. An example is marked with a circle in (c) and (d). This behavior is not surprising: the simulations of the NZ field presented in Figure 4.42 (§ 4.6.1), show that very small changes in the incoming wavelength (in that case, for example between 300 and 302 nm) may produce drastic changes in the NZ field configuration and enhancement. Note that this hot-spot is completely absent at $\hbar\omega = 3.1\,\text{eV}$ (see (b)).
The intensity profiles taken from Figures 4.45 (a) to (d) along section AB (white line in (b)) are shown in Figure 4.46. They reveal several interesting features:

- upon red-laser illumination regions 3, 4 and 5 have almost the same intensity, while regions 1, 2, the bare Si substrate and the 50 nm thick Ag film are characterized by a very low intensity. In particular, the bare Si substrate and the 50 nm thick Ag film do not show any significant signal above the background;

- upon blue-laser illumination, region 5, the 50 nm thick Ag film and the Si substrate are characterized by a very low intensity if compared to regions 1 to 4;

- upon UV light illumination the intensity increases monotonously with increasing Ag coverage from the bare Si substrate to region 5 and then slightly decreases towards the 50 nm thick Ag film (the same behavior was observed and discussed in § 4.3).

Clearly, the particle structure of the different films plays an important role to explain the above behavior. In analogy with the sample described in § 4.3.1, we expect that with increasing nominal thickness the regions 1 to 5 are constituted of small Ag particles with increasing linear dimensions (see

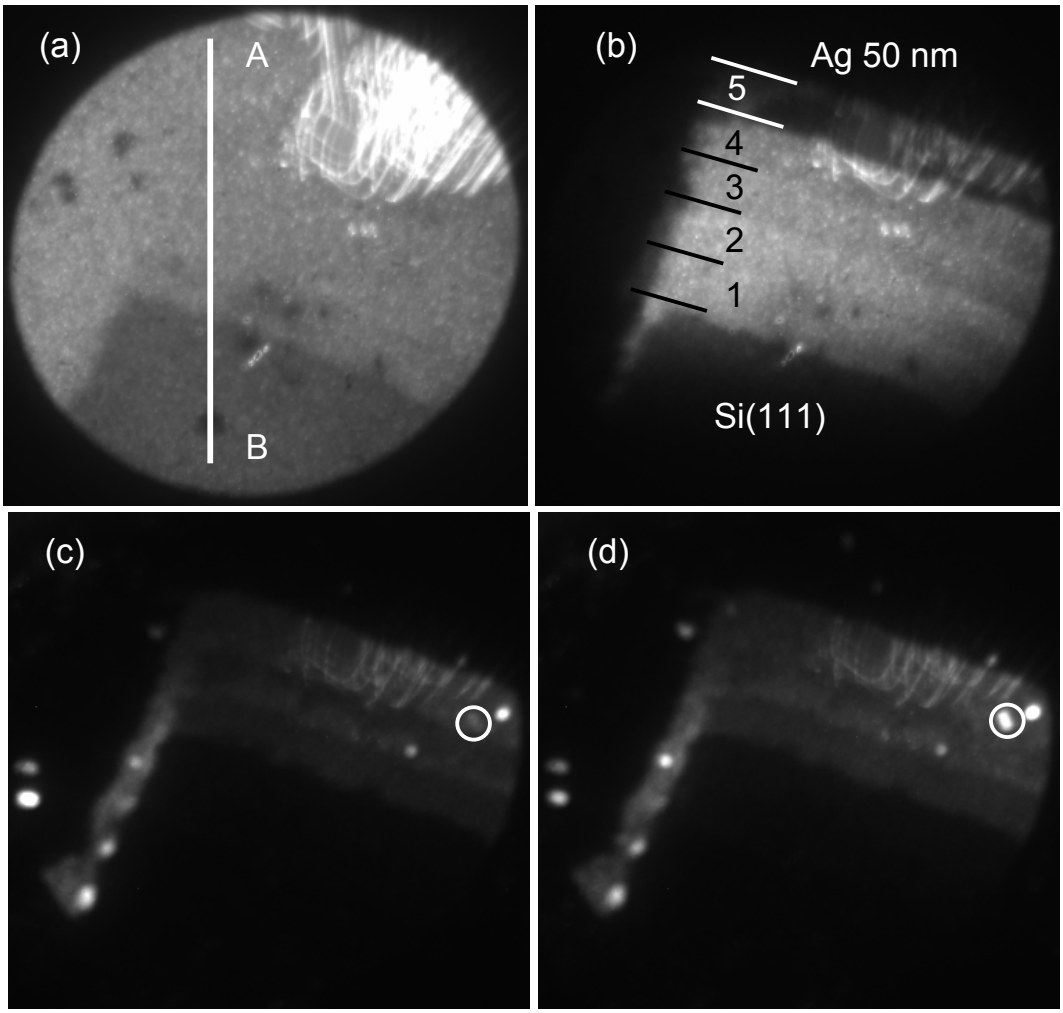

Figure 4.45: PEEM images of a 150 μm wide region of the Ag nanoparticle sample (stepped wedge, described in the text). Illumination sources: (a) Hg UV-lamp ($\hbar\omega = 5.8\,\mathrm{eV}$), (b) blue laser ($\hbar\omega = 3.1\,\mathrm{eV}$, p-polarization), (c) red laser ($\hbar\omega = 1.5\,\mathrm{eV}$, p-polarization), (d) red laser ($\hbar\omega = 1.6\,\mathrm{eV}$, p-polarization). The line AB in (a) indicates the position where the intensity profiles shown in Figure 4.46 have been taken. The feature on the top right is an artefact of the screen.

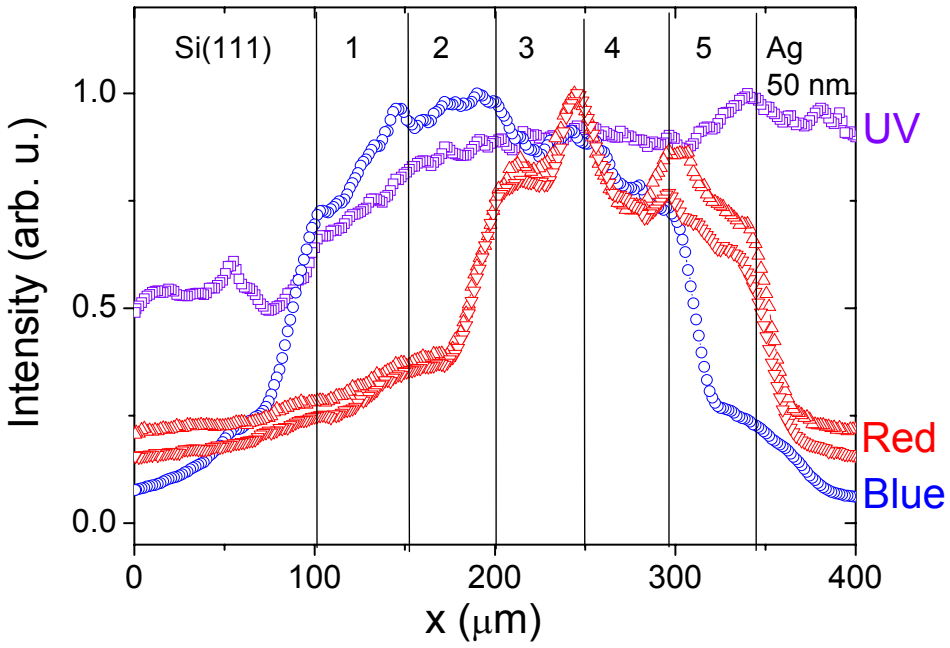

Figure 4.46: Intensity profiles from Figure 4.45 (a) (UV illumination), (b) (blue-laser illumination), (c) and (d) (red-laser illumination). These files have been taken along section AB marked in Figure 4.45 (a). The vertical lines indicate the position of the borders between the films 1 to 5.

Table 4.7). The blue laser obviously excites preferentially Ag particles with smaller radii, and the opposite holds for the red laser beam.
Since Figures 4.45 (a) to (d) have been taken with different exposure times, a comparison between absolute intensities for different illumination sources is not possible in Figure 4.46. Figure 4.47 compares the intensity of different regions on the sample, normalized to equal surface area and exposure times. The data are presented for UV, blue-laser and red-laser illumination. The latter have been multiplied by a factor of 200 in order to make them visible.

Figure 4.47 allows to make some interesting considerations:

- the 2PPE intensity (blue-laser excitation) from the 50 nm thick Ag layer is smaller than the 1PPE intensity (UV illumination). On the other hand, it is higher starting from region 4 and until the bare Si(111) substrate. This is a clear indication that the NZ field enhancement

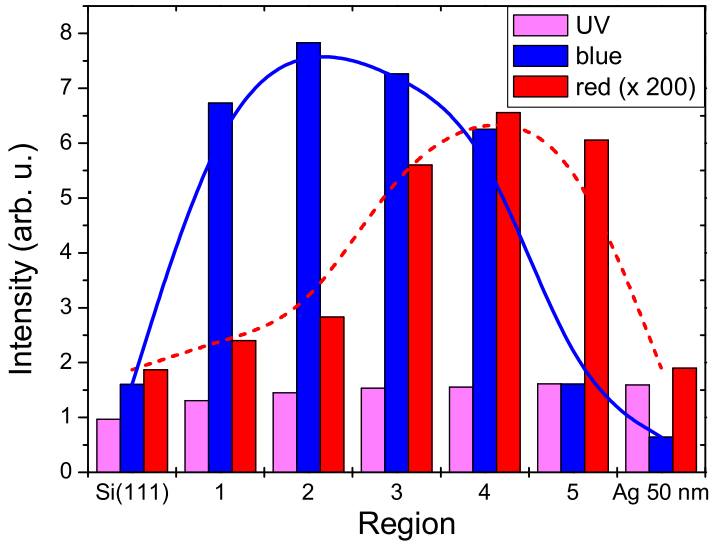

Figure 4.47: Photoemission intensities from regions 1 to 5, the bare Si(111) substrate and the 50 nm Ag film. The intensity is given per unit surface area and unit exposure time. Illumination sources: UV-lamp, blue laser and red laser. The data have been derived from Figures 4.45 (a), (b) and (c), respectively. For evaluation we used 10 μm square regions of interest.

produced by the nanoparticles in regions 1 to 4 under blue-laser illumination is extremely high and enhances 2PPE in comparison with 1PPE via UV illumination.

- the photoemission intensity under red-laser illumination is small if compared to the 1PPE and 2PPE intensity (about a factor of 200). The count rate from the 50 nm thick Ag film and the bare Si(111) substrate is mainly due to noise in the image intensifier (channelplate). No significant count rate is measured from these regions.

  Remember that the red-laser fluence (70 μJ cm^{-2}) is an order of magnitude higher than the blue fluence (6.4 μJ cm^{-2}). Despite of this, the yield for 3PPE is still much lower (by a factor of $2.3 \cdot 10^{-4}$) than the 2PPE yield. Only in regions 3, 4 and 5, where probably LSP resonance occurs, the NZ field is intense enough to allow 3PPE. Note that with the red laser beam mainly the regions with larger nanoparticles ($R \geq 20$ nm) emit electrons. This is in agreement with the fact that

for larger particle sizes ($R \geq 10\,\mathrm{nm}$) and irregular shapes, the LSP resonance is expected to show large red-shifts and splittings (see § 3.2.2).

Chapter 5

Conclusions and Outlook

Time-of-flight photoemission spectromicroscopy was used to measure and compare the two-photon photoemission (2PPE) spectra of Cu and Ag nanoparticles with linear dimensions ranging between 40 nm and several 100 nm, with those of the corresponding homogeneous surfaces.
2PPE was induced employing femtosecond laser radiation from a frequency-doubled Ti:sapphire laser in the spectral range between 375 nm and 425 nm (photon energy $\hbar\omega = 2.9 - 3.3\,\mathrm{eV}$) with a pulse width of 200 fs and a repetition rate of 80 MHz. A high-resolution photoemission electron microscope was equipped with a low-energy drift space for time-of-flight energy dispersion of the photoelectrons forming the image (resolution about 150 meV). Time-resolved image acquisition was facilitated using a (x,y,t)-resolving electron counting detector (delay-line detector). The 4D data-set accumulated by this special device allows to extract both energy-resolved images (a mode called spectromicroscopy) and local electron energy distribution curves (microspectroscopy mode). This newly developed hybrid technique turned out to be highly advantageous for the study of inhomogeneous surfaces, since it allows to extract all the required information from one single data-set. This assures that the absolute intensity scale, energy positions and resolution are perfectly identical in all the spectra extracted from the same data-set. Moreover, since the acquired 4D data-set can be processed after the measurement, the energy resolution of the energy-filtered images and the spatial resolution of the microspectra can be varied and optimized after data acquisition.
Ag nanoparticle films have been deposited on Si(111) by electron-beam evaporation, a technique leading to hemispherically-shaped Ag clusters. *Isolated Cu nanoparticles* (in the context of 2PPE also referred to as *hot-spots*) have been generated by prolonged heating of a polycrystalline Cu sample. Such inhomogeneities are preferentially formed at grain boundaries.
If compared to the spectra of the corresponding homogeneous surfaces, the

Cu and Ag nanoparticle spectra are characterized by a strongly enhanced total 2PPE yield (enhancement factor up to 70), by a shift (about 0.1 eV) of the Fermi level onset towards lower final state energies, by a reduction of the work function (typically by 0.2 eV) and by a much steeper increase of the 2PPE yield towards lower final state energies. The shift of the Fermi level onset in the nanoparticle spectra has been explained by a positive unit charge (localized photohole) residing on the particle during the time-scale relevant for the 2PPE process (few femtoseconds). A similar behavior has been found by Wertheim *et al.* [Wer83] in one-photon photoemission from clusters deposited on low-conductance substrates. The cluster charge is neutralized before the next photon pulse (12.5 ns) so that there is no long-term charge build-up.
The total 2PPE yield enhancement and the different overall shape of the spectra have been explained by considering that the laser frequency was close to the localized surface plasmon (LSP) resonance of the Cu and Ag nanoparticles. The synchronous oscillations induced by the laser in the metal electrons enhance the near-zone (NZ) field. It is defined as the linear superposition of the laser field and the field produced in the vicinity of the particles by the forced charge oscillations. The NZ field behavior directly influences the 2PPE and its dynamics.
The results allow the following conclusions:

- 2PPE from Cu and Ag homogeneous surfaces illuminated with laser light of about 400 nm wavelength ($\hbar\omega \approx 3.0$ eV) proceeds mainly via direct transitions ($\Delta k = 0$) through virtual intermediate states. In this case, mainly simultaneous 2PPE excitations occur, with no time-delay between the absorption of two photons from a laser pulse. This is in accordance with earlier results from spectroscopy experiments without spatial resolution.

- The missing translational symmetry and, in particular, the strong spatial dependence of the NZ electric field of the nanoparticles allows 2PPE to proceed via indirect transitions ($\Delta k \neq 0$) through real intermediate states as well. In this case, both simultaneous and cascade (i.e sequential) excitations are possible. In a sequential excitation the intermediate state population undergoes relaxation processes by electron-electron and electron-surface scattering before the second photon is absorbed (within the duration of a laser pulse). This relaxation is the main cause for the steeper intensity increase at lower final-state energies in the electron energy distribution spectra of the nanoparticles. The typical lifetime of an electron in the intermediate state 3 eV above the Fermi energy is 3 fs, whereas the laser pulse has a duration of 200 fs.

The spatial dependence of the NZ field discussed by Shalaev *et al.* [Sha96] is characterized by a field amplitude proportional to r^{-3}, with r being the radial coordinate of the particle. As discussed in § 3.3, this has been derived for the case of a fractal aggregate, i.e. a statistical distribution of roughness features on a surface. Clearly, the NZ field produced by isolated clusters strongly depends on their shape, material and on the wavelength. An accurate solution for the NZ fields of LSP-resonant particles of arbitrary shape is still a theoretical challenge. Analytical solutions are known only for particles with a very simple shape, like that of a sphere or an ellipsoid.

From the present measurements it is clear that the NZ field behavior is responsible for the 2PPE enhancement and affects the 2PPE spatial and energy distribution and its dynamics. In particular, its strong spatial dependence allows indirect transitions through real intermediate states to take place in the metal clusters. Such transitions are forbidden by momentum conservation arguments and are thus experimentally at least much less probable on homogeneous surfaces.

We have also shown that even three-photon photoemission processes on rough surfaces are induced by illumination with laser light of 800 nm wavelength (photon energy $\hbar\omega = 1.5\,\mathrm{eV}$). Analogously, the results can be explained with nPPE by considering the effects of collective electron excitations in nanoparticles and roughness features and the consequent modification of the NZ field.

Other possible electron emission mechanisms that could be induced by the excitation of LSP are discussed in the literature. Among them, there are for example field emission induced by the laser field, thermionic emission from a transient hot electron gas and radiationless decay of a collective electron excitation into a single electron-hole pair. At our experimental conditions, with a laser fluence per pulse of $6.4\,\mu\mathrm{J{\cdot}cm^{-2}}$ and 80 MHz repetition rate, we could rule out a decisive contribution from such emission mechanisms. We expect, however, that for higher laser pulse fluences, particularly the first two mentioned emission mechanisms could play an important role.

All these observations led us to the idea of investigating with the photoemission microscope specially tailored small metal structures, whose NZ field is theoretically predictable, and to compare the quantitative solution of the NZ field with the laterally resolved 2PPE signal. For this purpose we investigated so-called *Ag moon-like nanostructures* prepared by M. Kreiter and coworkers (MPI for Polymer Research, Mainz). We could show that the laterally resolved 2PPE signal gives a clear fingerprint of the theoretically predicted spatial dependence of the NZ field.

This latter experiment is very promising for future research. A systematic study of well-defined structures should lead to find a quantitative relation between the NZ field spatial distribution of a single structure and the cor-

responding 2PPE signal. This could make photoelectron microscopy a good technique for the direct lateral visualization of the NZ field behavior of nanostructured samples. This potential of our method is highly attractive for the novel field of *plasmonics* [Ebb98, Lez02, Sch03], dealing with the interplay between electromagnetic radiation in vacuum and both localized and propagating surface plasmons (or plasmon-polaritons) in nanostructured devices. The crucial point is that 2PPE or nPPE electron microscopy is capable of probing the NZ fields, whereas optical microscopy gives access only to the far-field behavior and scanning near-field optical microscopy (SNOM) influences the NZ field due to the presence of the tip.

Zusammenfassung und Ausblick

Die Zweiphotonen-Photoemission (2PPE) von Cu- und Ag-Nanoteilchen mit Größen zwischen 40 nm und einigen 100 nm wurde mit Hilfe einer neuartigen Flugzeit-Spektromikroskopietechnik untersucht. Die zugehörigen Elektronen-Energieverteilungskurven wurden mit den entsprechenden Spektren homogener Oberflächen verglichen. 2PPE-Übergänge wurden durch einen Femtosekundenlaser induziert, dazu stand ein Ti:Sa-Laser mit Frequenzverdopplung zur Verfügung. Somit lag die Laserwellenlänge in einem Bereich zwischen 375 nm und 425 nm (Photonenenergie $\hbar\omega = 2.9 - 3.3\,\mathrm{eV}$) bei einer Pulsbreite von 200 fs und einer Wiederholungsrate von 80 MHz. Ein hochauflösendes Photoemissions-Elektronenmikroskop (Auflösungsgrenze 20 nm) wurde mit einer Niederenergiedriftstrecke ausgestattet, so dass über die Flugzeit eine Energiedispersion der abbildenden Photoelektronen auftrat (Auflösung ca. 150 meV). Zeitaufgelöste Aufnahmen wurden durch einen (x,y,t)-auflösenden Elektronendetektor (delay-line detector) erreicht. Der so erhaltene 4D-Datensatz erlaubt es, sowohl energieaufgelöste Bilder (Spektromikroskopie), als auch lokale Energieverteilungskurven von Elektronen (Mikrospektroskopie) zu bestimmen. Diese neu entwickelte Hybrid-Technologie erwies sich als äußerst vorteilhaft für die Untersuchung inhomogener Oberflächen, da sie die Extraktion sämtlicher benötigter Informationen aus nur einem Datensatz erlaubt. Dadurch ist sichergestellt, dass die absolute Intensitätsskala, Energiepositionen und Auflösung in Raum und Zeit (d.h Energie) in allen Spektren und Bildern eines Datensatzes, identisch sind. Aufgrund der Möglichkeit, den akkumulierten 4D-Datensatz nach der Messung zu bearbeiten, können die Energieauflösung der energiegefilterten Bilder sowie die örtliche Auflösung der Mikrospektren auch nach der Datenaufnahme variiert werden, um Parameter wie Bildkontrast oder Signal-zu-Rauschvehältnis zu optimieren.

Ag Nanoteilchen-Filme wurden durch Elektronenstrahl-Verdampfung auf Si(111) aufgebracht, was zu hemisphärisch geformten deponierten Ag-Clustern führt. *Isolierte Cu-Nanoteilchen* (im Kontext der 2PPE auch *hot-spots* genannt) wurden durch längeres Erhitzen einer polykristallinen Cu-Probe erzeugt. Dabei bilden sich solche Inhomogenitäten bevorzugt an Korngrenzen.

Verglichen mit den Spektren der jeweiligen homogenen Oberflächen, zeigen die Spektren der Cu- und Ag-Nanoteilchen eine stark erhöhte 2PPE-Ausbeute (bis zu 70 fach erhöht), eine Verschiebung des Fermikanten-Ansatzes in Richtung kleinerer Endzustandsenergien (etwa 0.1 eV), eine Absenkung der Austrittsarbeit (typisch 0.2 eV) und eine sehr viel steilere Zunahme der 2PPE-Ausbeute in Richtung kleinerer Endzustandsenergien.
Die Verschiebung des Fermikanten-Ansatzes in den Spektren der Nanoteilchen konnte durch eine positive Elementarladung (lokalisierter Lochzustand) erklärt werden, die sich in der für den 2PPE-Prozess relevanten Zeit (einige fs) auf den Partikeln befindet. Ein ähnliches Verhalten wurde von Wertheim *et al.* [Wer83] in Einphotonen-Photoemission von Clustern auf schlecht leitenden Substraten beobachtet. Die Cluster-Ladung wird vor dem nächsten Photonenpuls (d.h. innerhalb von 12.5 ns) neutralisiert, so dass keine Ladung akkumuliert wird. Die erhöhte 2PPE-Ausbeute und die unterschiedliche Form der Spektren wurden dadurch erklärt, dass die Laserfrequenz im Bereich der lokalisierten Oberflächenplasmonen (localized surface plasmons - LSP) Resonanz der Cu- und Ag-Nanoteilchen liegt. Die vom Laser im Metall angeregten synchronen Oszillationen verstärken das Nahzonenfeld (NZ-Feld). Dies besteht aus der linearen Überlagerung des Laserfeldes und des durch die erzwungene Ladungsbewegung des Clusters erzeugten Feldes im nahen Umfeld der Partikel. Das Verhalten des NZ-Feldes beeinflusst direkt die 2PPE und deren Dynamik.
Aus den Resultaten kann man folgendes schließen:

- Die 2PPE von homogenen Cu- and Ag-Oberflächen, die von Laserlicht mit Wellenlängen um 400 nm ($\hbar\omega \approx 3.0$ eV) bestrahlt werden, geschieht hauptsächlich durch direkte Übergänge ($\Delta k = 0$) über virtuelle Zwischenzustände. In diesem Fall treten überwiegend simultane 2PPE-Anregungen ohne Zeitverzögerung zwischen der Absorption zweier Photonen aus einem Laserpuls auf. Dieser Befund bestätigt Resultate aus früheren spektroskopischen Arbeiten ohne Ortsauflösung.

- Die fehlende Translationssymmetrie und besonders die starke örtliche Abhängigkeit des elektrischen NZ Feldes der Nanoteilchen machen 2PPE auch durch indirekte Übergänge ($\Delta k \neq 0$) über reelle Zwischenzustände möglich. In diesem Fall sind nicht nur simultane sondern auch sequentielle 2PPE-Anregungen (Kaskadenprozesse) möglich. Bei einer sequentiellen Anregung wird die Besetzung der Zwischenzustände durch inelastische Elektron-Elektron- und Elektron-Oberflächen-Streuung beeinflußt, bevor ein zweites Photon absorbiert wird (innerhalb der Dauer eines Laserpulses). Diese Relaxation ist der Hauptgrund für den steileren

Intensitätsanstieg bei niedrigeren Endzustandsenergien in den Energieverteilungskurven der Elektronen von Nanoteilchen. Die typische Lebensdauer eines Elektrons in einem Zwischenzustand 3 eV oberhalb der Fermienergie ist 3 fs, während der Laserpuls eine Länge von 200 fs hat.

Laut Shalaev *et al.* [Sha96] ist die örtliche Abhängigkeit des NZ-Feldes durch eine Feldamplitude proportional zu r^{-3} charakterisiert, wobei r die radiale Koordinate des Teilchens ist. Wie in § 3.3 diskutiert, wurde dies für den Fall von fraktalen Aggregaten, d.h. statistisch verteilten Rauhigkeitsstrukturen auf der Oberfläche, abgeleitet. Offensichtlich hängt das von isolierten Clustern erzeugte NZ-Feld stark von deren Form, Material und der Wellenlänge ab. Eine analytische Lösung des NZ-Feldes in der Plasmonenresonanz von Partikeln beliebiger Form ist noch immer eine Herausforderung an die Theorie. Analytische Lösungen des NZ Feldes sind nur für Teilchen mit spezieller Form wie Kugeln oder Ellipsoide bekannt.
Aus den gezeigten Messungen geht eindeutig hervor, dass das Verhalten des NZ-Feldes verantwortlich sowohl für die Erhöung, als auch für die örtliche und energetische Verteilung des 2PPE-Signals und dessen Dynamik ist. Besonders die starke räunmliche Abhängigkeit des NZ-Feldes erlaubt indirekte Übergänge durch reelle Zwischenzustände in metallischen Clustern. Solche Übergänge sind aus Impulserhaltungsgrunden verboten und daher experimentell zumindest sehr unwahrscheinlich für homogene Oberflächen.
Weiterhin wurde gezeigt, dass sogar Dreiphotonen-Photoemissionsprozesse von rauhen Oberflächen durch Beleuchtung mit Laserlicht um 800 nm Wellenlänge (Photonenenergie $\hbar\omega \approx 1.5\,\mathrm{eV}$) induziert werden. Auch diese Ergebnisse können durch Effekte von kollektiven Elektronenanregungen in Nanopartikeln und Unebenheiten der Oberfläche und der damit verbundenen Modifikationen am NZ-Feld erklärt werden. In der Literatur werden neben der nPPE andere Emissionsmechanismen diskutiert, z.B. die durch das Laserfeld induzierte Feldemission, die thermoelektrische Emission eines transienten heißen Elektronengases oder der strahlungslose Zerfall der kollektiven Elektronenoszillation in ein einzelnes Elektron-Loch-Paar. Bei den gegebenen Parametern von Laserfluenz ($6.4\,\mu\mathrm{J{\cdot}cm^{-2}}$ pro Puls) und Repetitionsrate (80 MHz) wurden keine eindeutigen Hinweise auf signifikante Beiträge solcher Prozesse gefunden. Es ist jedoch zu erwarten, dass bei höheren Pulsleistungen des Lasers insbesondere die beiden erstgenannten Emissionsmechanismen bedeutend werden.
Aufgrund der Beobachtungen schien es vielversprechend, Photoemissions-Untersuchungen an gezielt präparierten Nanostrukturen durchzuführen, deren NZ-Feld theoretisch berechenbar ist, und die quantitative Lösung des NZ-Feldes mit dem lateral aufgelösten 2PPE-Signal zu vergleichen. Zu die-

sem Zweck wurden *sichelförmige Ag-Strukturen* von M. Kreiter und Mitarbeitern (MPI für Polymerforschung, Mainz) hergestellt. Wir konnten zeigen, dass das lateral aufgelöste 2PPE-Signal einen klaren Fingerabdruck der theoretisch vorhergesagten räumlichen Abhängigkeit des NZ-Feldes liefert.
Das letztgenannte Experiment ist sehr vielversprechend für zukünftige Forschungen. Eine systematische Untersuchung wohldefinierter Strukturen sollte zu einem quantitativen Zusammenhang zwischen örtlicher Verteilung des NZ Feldes und dem korrespondierenden 2PPE-Signal führen. Dies könnte Photoemissionsmikroskopie als geeignete Technik für direkte, laterale Visualisierung des NZ-Feld-Verhaltens nanostrukturierter Proben etablieren. Hohes Potential besteht ebenso bei der Anwendung im neuen Forschungsgebiet *Plasmonics* [Ebb98, Lez02, Sch03], das sich mit dem Zusammenhang zwischen elektromagnetischer Strahlung im Vakuum und lokalisierten bzw. propagierenden Oberflächenplasmonen (oder Plasmon-Polaritonen) in nanostrukturierten Einheiten befasst. Der entscheidende Punkt ist, dass durch 2PPE oder nPPE-Eektronenmikroskopie das NZ-Feld abgetastet werden kann, während optische Mikroskopie nur Zugang zum Fernfeldverhalten bietet und scanning near-field optical microscopy (SNOM) das Nahfeld durch die vorhandene Spitze signifikant beeinflusst.

Appendix A

PEEM's Transmission Function

The contrast aperture located in the PEEM back focal plane (BFP) (see Figure 2.3) limits the angle of the electrons transmitted by the objective lens. The maximal transmitted angle ($\alpha_{0,max}$) depends on the electron start energy as well. To calculate it, let us consider an electron starting on the sample with an energy E_0 at the position r_0 and with the angle α_0. For the coordinates (E_i, r_i, α_i) in the first image plane we apply the Helmholtz-Lagrange theorem:

$$\sqrt{E_0} r_0 \sin\alpha_0 = \sqrt{E_i} r_i \sin\alpha_i \,. \tag{A.1}$$

With $\alpha_i \ll 1$ and the magnification $M = r_i/r_0$ it follows:

$$\alpha_i = \frac{1}{M} \sin\alpha_0 \sqrt{\frac{E_0}{E_i}} \,. \tag{A.2}$$

The PEEM objective can be schematized as a thick lens. Figure A.1 shows a schematic representation of the PEEM objective lens and the region of the first image plane. For a thick lens it holds $M \cdot f_2 = (q - f_2)$. Moreover, for a small aperture it is $\alpha_i = r_{ap}/(q - f_2)$, and thus:

$$r_{ap} = \sin\alpha_0 \sqrt{\frac{E_0}{E_i}} \frac{q - f_2}{M} \,. \tag{A.3}$$

This gives for the maximal start angle on the sample:

$$\alpha_{0,max} = \arcsin\left\{ \frac{r_{ap} M}{q - f_2} \sqrt{\frac{E_i}{E_0}} \right\} . \tag{A.4}$$

For the Focus PEEM used in the standard imaging mode (tetrode mode) one has $M = 40$, $(q - f_2) = 150\,\mathrm{mm}$. Figure A.2 shows the dependence of $\alpha_{0,max}$ vs. start energy E_0, calculated with the parameters given above and

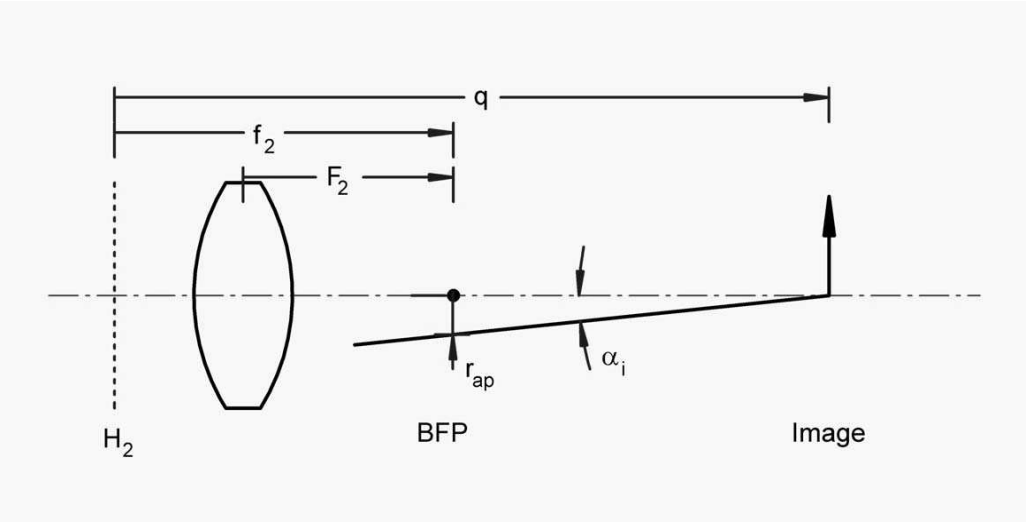

Figure A.1: Schematic representation of the PEEM objective towards the first image plane. The objective can be schematized as a thick lens with principal plane H_2 and focal distances f_2 and F_2. The contrast aperture with radius r_{ap} lies in the back focal plane (BFP) and limits the possible values for the angle α_i.

with $E_i = 1.2\,\mathrm{keV}$ (corresponding to the standard column voltage of $1.2\,\mathrm{kV}$). The curve is plotted for different values of r_{ap}.
To evaluate the PEEM transmission function, we now consider that electrons with an angle α are emitted within the solid angle:

$$d\Omega = \pi \cdot \sin\alpha\,. \tag{A.5}$$

If we assume that the photoelectrons are emitted under the angle α with a probability proportional to $\cos(\alpha)$ (valid for isotropic photoemission), we can estimate the transmission function T as follows:

$$T \sim \int_0^{\alpha_{0,max}} \cos\alpha\, d\Omega \sim \sin^2\alpha_{0,max}\,, \tag{A.6}$$

and using Equation A.4:

$$T \sim sin^2\left\{\arcsin\left\{\frac{r_{ap}M}{q-f_2}\sqrt{\frac{E_i}{E_0}}\right\}\right\} = \left(\frac{r_{ap}M}{q-f_2}\right)^2 E_i \cdot \frac{1}{E_0}\,. \tag{A.7}$$

Thus, in the standard operation mode of the PEEM it holds:

$$T(r_{ap}, E_0) \sim 8.5 \cdot 10^7\, \frac{r_{ap}^2}{E_0}\,. \tag{A.8}$$

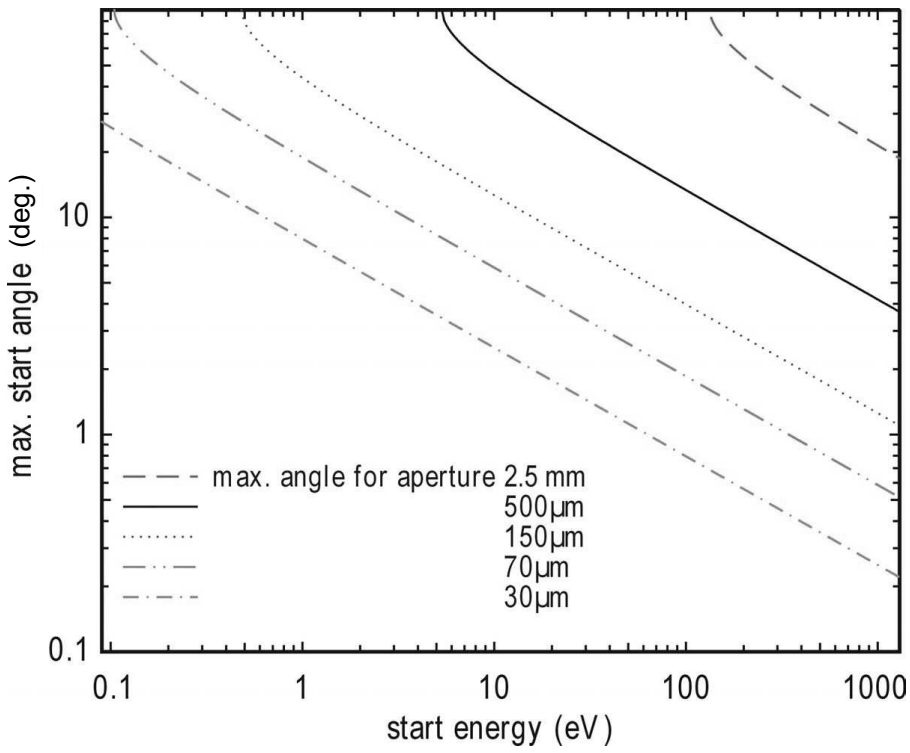

Figure A.2: Maximal start angle ($\alpha_{0,max}$) for the electrons on the sample vs. start energy (E_0), calculated for different aperture radii r_{ap} from equation (A.4). Used values: $M = 40$, $(q - f_2) = 150\,\text{mm}$, $E_i = 1200\,\text{eV}$.(Courtesy M. Escher, Focus GmbH.)

Appendix B

Dielectric Function of a Free-Electron Gas

The complex dielectric function $\varepsilon(\mathbf{k}, \omega)$ plays an extremely important role in the description of the response of metals to an external electromagnetic field. In the following we describe the context in which the dielectric function is defined, together with the magnetic permeability $\eta(\mathbf{k}, \omega)$ and present a calculation of the dielectric function in the framework of the Drude model for metals.

B.1 Definition of the dielectric function

The propagation of an electromagnetic wave in a medium can be described by Maxwell's equations (in CGS units):

$$\left.\begin{aligned} &\nabla \cdot \mathbf{D} = 4\pi\rho \\ &\nabla \times \mathbf{H} - \tfrac{1}{c}\tfrac{\partial \mathbf{D}}{\partial t} = \tfrac{4\pi}{c}\mathbf{J} \\ &\nabla \times \mathbf{E} + \tfrac{1}{c}\tfrac{\partial \mathbf{B}}{\partial t} = 0 \\ &\nabla \cdot \mathbf{B} = 0 \end{aligned}\right\} \tag{B.1}$$

where $\mathbf{E}$ and $\mathbf{B}$ are the macroscopical average values of the fields $\mathbf{E}$ and $\mathbf{B}$ defined by Maxwell's equations in vacuum. Analogously the density of charge and current ρ and $\mathbf{J}$ are macroscopical averages of the *free* density of charge and current. The charges and currents that are produced in the medium as a consequence of the presence of the external field are included

in the equations through the definition of the fields **D** and **H**:

$$\begin{aligned} D_\alpha &= E_\alpha + 4\pi \left(P_\alpha - \textstyle\sum_\beta \frac{\partial Q'_{\alpha\beta}}{\partial x_\beta} + \ldots \right) \\ H_\alpha &= B_\alpha - 4\pi (M_\alpha + \ldots) \end{aligned} \tag{B.2}$$

where the quantities **P**, **M**, $Q'_{\alpha\beta}$ and analogous terms of superior order are the macroscopic averages of the electric dipole, magnetic dipole, electric quadrupole and terms of higher order, acquired from the medium in the presence of the external field.
In non ferroelectric or non ferromagnetic materials, and for sufficiently weak external fields the presence of an electric or magnetic field produces a linear response in the medium. If, moreover, the medium is isotropic, one can rewrite the Fourier transform of (B.2) as:

$$\begin{aligned} \mathbf{D}(\mathbf{k},\omega) &= \varepsilon(\mathbf{k},\omega)\mathbf{E}(\mathbf{k},\omega) \\ \mathbf{B}(\mathbf{k},\omega) &= \eta(\mathbf{k},\omega)\mathbf{H}(\mathbf{k},\omega) \end{aligned} \tag{B.3}$$

with

$$\begin{aligned} \varepsilon(\mathbf{k},\omega) &= \tfrac{\mathbf{D}}{\mathbf{E}} = 1 + 4\pi \mathbf{P}/\mathbf{E} \\ \eta(\mathbf{k},\omega) &= \tfrac{\mathbf{H}}{\mathbf{B}} = 1 - 4\pi \mathbf{M}/\mathbf{B} \end{aligned} \tag{B.4}$$

Equations (B.4) define the dielectric function $\varepsilon(\mathbf{k},\omega)$ and the magnetic permeability $\eta(\mathbf{k},\omega)$ of the medium.

B.2 Dielectric function and plasma frequency of a free-electron gas

We now consider the propagation of an electromagnetic field in a free-electron metal. In the range of optical frequencies it is possible to assume $\eta(\mathbf{k},\omega) = 1$ and concentrate only on the effects of a propagating free electric field [Kre93]. The strong dependence of the dielectric function from the frequency ω and from the wave vector $\mathbf{k}$ characterizes the physical properties of the metal. On the one side, the limit value $\varepsilon(\mathbf{0},\omega)$ describes the collective excitations of the free-electrons sea (i.e., the bulk and surface plasmons); on the other side the

value $\varepsilon(\mathbf{k}, 0)$ describes the electrostatic screening produced by the electron-electron and electron-phonon interaction in the crystal. We now derive an expression for the quantity $\varepsilon(\mathbf{0}, \omega) \equiv \varepsilon(\omega)$.
The response of a free electron of mass m and charge e to an external electric field $\mathbf{E} = \mathbf{E}_0 e^{-\imath\omega t}$ can be described by the equation:

$$m\frac{\partial^2 \mathbf{r}}{\partial t^2} + m\Gamma\frac{\partial \mathbf{r}}{\partial t} = e\mathbf{E}_0 e^{-\imath\omega t} \tag{B.5}$$

where Γ is a phenomenological parameter that describes the damping of the electron motion. The solution of (B.5) can be used to calculate the polarization $\mathbf{P} = ne\mathbf{r}$, with n giving the volume density of electrons. Substituting the expression of $\mathbf{P}$ in (B.4), gives:

$$\varepsilon(\omega) = 1 - \frac{\omega_p^2}{\omega^2 + \imath\Gamma\omega} = 1 - \frac{\omega_p^2}{\omega^2 + \Gamma^2} + \imath\frac{\omega_p^2\Gamma}{\omega(\omega^2 + \Gamma^2)} \tag{B.6}$$

where

$$\omega_p = \sqrt{\frac{4\pi n e^2}{m}} \tag{B.7}$$

is the plasma frequency. The constant Γ can be related to the electron mean free path ℓ by $\Gamma = v_F/\ell$, where v_F is the Fermi velocity. Taking $\ell \approx 10\,\text{nm}$ and $v_F \approx 10^8\,\text{cm/sec}$, that are reasonable values for most noble and alkali metals we obtain $\Gamma \approx 10^{14}\,\text{Hz}$. Thus, in the optical region one has $\omega \gg \Gamma$ and it is possible to write the real and imaginary part of the dielectric function (ε_1 and ε_2) as:

$$\varepsilon_1 \approx 1 - \tfrac{\omega_p^2}{\omega^2} \tag{B.8}$$

$$\varepsilon_2 \approx \tfrac{\omega_p^2}{\omega^3}\Gamma \tag{B.9}$$

B.3 Dispersion relation of an electromagnetic wave

In an isotropic and non-magnetic medium the wave equation of an electromagnetic wave reads:

$$\frac{\partial^2 \mathbf{D}}{\partial t^2} = c^2\nabla^2\mathbf{E}\ . \tag{B.10}$$

If one looks for a solution of (B.10) with $\mathbf{E} \propto e^{-\imath\omega t}e^{\imath\mathbf{k}\cdot\mathbf{r}}$ and $\mathbf{D} = \varepsilon(\mathbf{k}, \omega)\mathbf{E}$, then one finds that the following relation must be satisfied:

$$\varepsilon(\mathbf{k}, \omega)\omega^2 = c^2k^2\ . \tag{B.11}$$

Equation (B.11) is the dispersion relation of the electromagnetic wave. Depending on the value of ε one can distinguish between the following situations:

- ε real and > 0. If ω is real, then also k is real. This corresponds to the propagation of a transversal electromagnetic wave with phase velocity $c/\sqrt{\varepsilon}$.
- ε real and < 0. If ω is real, then k is imaginary. The electromagnetic wave is damped with the characteristic length $1/|k|$.
- ε complex. If ω is real, then k is complex and the wave is damped.
- $\varepsilon \to \infty$. Even for very small external fields the system shows a finite reaction. Thus, the poles of $\varepsilon(\mathbf{k}, \omega)$ define the frequencies of free oscillations of the medium.
- $\varepsilon = 0$. This is the condition for the propagation of longitudinal waves in the medium (bulk plasmons) [Kre93].

Appendix C

Escape Function of Rough Surfaces

We consider the escape function $T_R(E)$ of rough films and compare it with the corresponding quantity for smooth films $T_S(E)$ (see 3.31):

$$T_S(E) = \frac{1}{2}\left[1 - \left(\frac{E_F + \phi_m}{E + \hbar\omega'}\right)^{1/2}\right] \ . \tag{C.1}$$

Within the three step model for photoemission, an electron can escape from a solid into vacuum if its momentum along the surface normal k_n is large enough to pass through the surface barrier. In other words, it must hold:

$$E_n \equiv E_0 + \beta k_n^2 > E_F + \phi_m \ , \tag{C.2}$$

where E_n defines the electron energy corresponding to its momentum component k_n along the surface normal, E_0 is a constant and ϕ_m is the metal work function. After absorption of one or more photons it may happen that the energy of an electron is $E > E_F + \phi_m$, but $E_n < E_F + \phi_m$. This means actually that the electron is not moving along a direction favorable for photoemission. If the electron's mean free path l is sufficiently large compared to the roughness dimensions, elastic scattering with the roughness features provides a mechanism for reorienting its direction so that ultimately $E_n < E_F + \phi_m$. This qualitative argument suggests that eventually it will hold $T_R > T_S$. Assuming spherical roughness features with radius R_0 it is possible to write the escape function T_R^0 for elastic diffuse reflections as [Che86]:

$$T_R^0(E) = \frac{T_S(E)T_t(E)}{\{1 - [1 - T_S(E)]T_t'(E)\}} \ , \tag{C.3}$$

with

$$\begin{aligned} T_t(E) &= 3/2(l/R_0)^4\{2(R_0/l) - 3 + \\ &\quad + \exp(-2R_0/l)[2(R_0/l)^2 + 4(R_0/l) + 3]\} \ , \\ T_t^{'}(E) &= (l/2R_0)[1 - \exp(-2R_0/l)] \ . \end{aligned}$$

From a comparison between (C.3) and (C.1) one has that in the limit $l \gg R_0$ and in the threshold region it holds $T_S \ll T_R^0$. In general, it is possible to show that $T_S \ll T_R$, where T_R contains the term T_R^0 plus the contribution from specular (not diffuse) reflections [Sha96].

Appendix D

Light Penetration Depth in Ag

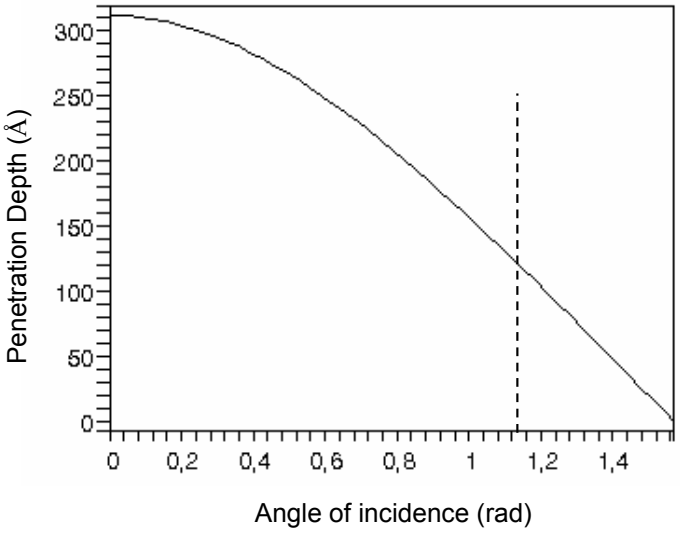

Figure D.1: Penetration depth (in $\mathring{A}$) for s-polarized light with photon energy $\hbar\omega = 3.0\,\mathrm{eV}$ incident onto a Ag surface vs. the angle of incidence (in rad.). Optical constants :$n = 0.173$, $k = 2.11$ from [Pal85]. Across a particle with 30 nm diameter the photon intensity drops by a factor $1/e$ only. At our given angle of incidence of 65° ($\approx 1.13\,\mathrm{rad}$), see dashed line, the $1/e$ drop is already reached at about 12 nm depth.

Appendix E

List of Used Abbreviations

2PPE	Two-Photon Photoemission
2PPS	Two-Photon Photoemission Spectroscopy
AFM	Atomic Force Microscopy
BFP	Back Focal Plane
FWHM	Full Widht at Half Maximum
LEED	Low-Energy Electron Diffraction
LSP	Localized Surface Plasmon
MCP	Multichannelplate
NZ	Near Zone (Field)
PEEM	Photoemission Electron Microscope
PES	Photoemission Electron Spectroscopy
RFA	Retarding Field Analyzer
SEM	Scanning Electron Microscopy
SNOM	Scanning Near-field Optical Microscopy
SPW	Surface Plasmon Wave
TDC	Time-to-Digital-Converter
TOF	Time-of-Flight
TR-2PPE	Time-Resolved Two-Photon Photoemission
UHV	Ultra High Vacuum
UPS	Ultraviolet Photoemission (electron) Spectroscopy
UV	Ultra-Violet (light)

Bibliography

[Aes95] M. Aeschlimann, C. A. Schmuttenmaer, H. E. Elsayed-Ali, R. J. D. Miller, J. Cao, Y. Gao and D. A. Mantell. *Journal of Chemical Physics* **102 (21)** (1995), 8606.

[Ash98] Ashcroft and Mermin. *Solid State Physics*. Saunders College (1998).

[Asp83] D. E. Aspnes. *Surface Science* **132** (1983), 406.

[Bar83] P. W. Barber, R. K. Chang and H. Massoudi. *Physical Review B* **27 (12)** (1983), 7251.

[Bar95] A. L. Barbasi and H. E. Stanley. *Fractal Concepts in Surface Growth*. Cambridge University Press, Cambridge (1995).

[Bau02] M. Bauer and M. Aeschlimann. *Journal of Electron Spectroscopy and related Phenomena* **124** (2002), 225.

[Bea69] D. Beaglehole. *Physical Review Letters* **22** (1969), 708.

[Ber64a] C. N. Berglund and W. E. Spicer. *Physical Review* **136 (4A)** (1964), A1044.

[Ber64b] C. N. Berglund and W. E. Spicer. *Physical Review* **136 (4A)** (1964), A1030.

[Ber87] Bergmann and Schaefer. *Lehbuch der Experimentalphysik*, vol. 3, Optik. Walter de Gruyter, Berlin New York, 8 ed. (1987).

[Bor81] J. P. Borel and J. Buttet. *Surface Science* **106**.

[Bra93] M. Brack. *Review of Modern Physics* **65** (1993), 677.

[Cad78] M. Cadorna and L. Ley. *Photoemission in Solids 1*, vol. 26 of *Topics in Applied Physics*. Springer-Verlag Berlin (1978).

[Cah03] D. Cahen and A. Kahn. *Advanced Materials* **15 (4)** (2003), 271.

[Che86] Q. Y. Chen and C. W. J. Bates. *Physical Review Letters* **57** (1986), 2737.

[Chi91] R. Chiarello, V. Panella, J. Krim and C. Thompson. *Physical Review Letters* **67** (1991), 3408.

[De 98] G. De Stasio, M. Capozi, G. F. Lorusso, P. A. Baudat, T. C. Droubay, P. Perfetti, G. Margaritondo and B. P. Tonner. *Revew of Scientific Instruments* **69** (1998), 2062.

[Des93] M. C. Desjonquères and D. Spanjaard. *Concepts in Surface Physics*. Springer (1993).

[DH87] W. A. De Heer, W. D. Knight, M. Y. Chou and M. L. Cohen. *Solid State Physics* **40** (1987), 93.

[Dou95] C. Douketis, Z. Wang, T. L. Haslett and M. Moskovits. *Physical Review B* **51** (1995), 11022.

[Dür02] H. A. Dürr, F. Kronast and W. Eberhardt. *Advances in Solid State Physics* **41** (2002), 557.

[Ebb98] T. W. Ebbesen, H. J. Lezec, H. F. Ghaemi, T. Thio and P. A. Wolff. *Nature* **391** (1998), 667.

[Ehr62] H. Ehrenreich and H. R. Philipp. *Physical Review* **128 (4)** (1962), 1622.

[End70] J. G. Endriz and W. E. Spicer. *Physical Review Letters* **24** (1970), 64.

[Fan92] W. S. Fann, R. Storz, H. W. K. Tom and J. Bokor. *Physical Review Letters* **68** (1992), 2834.

[Fec] G. H. Fecher. Privat communication.

[Fec02] G. H. Fecher, O. Schmidt, Y. Hwu and G. Schönhense. *Journal of Electron Spectroscopy and Related Phenomena* **126** (2002), 77.

[Fed00] R. D. Fedorovich, A. G. Naumovets and P. M. Tomchuk. *Physics Reports* **328** (2000), 73.

[Fuj84] J. G. Fujimoto, J. M. Liu, E. P. Ippen and N. Bloembergen. *Physical Review Letters* **53** (1984), 1837.

[Gav99] L. Gavioli, K. R. Kimberlin, M. C. Tringides, J. F. Wendelken and Z. Zhang. *Physical Review Letters* **82 (1)** (1999), 129.

[Gün02] S. Günther, B. Kaulich, L. Gregoratti and M. Kiskinova. *Progress in Surface Science* **70** (2002), 187.

[Gor91] S. A. Gorban, S. A. Nepijko and P. M. Tomchuk. *International Journal of Electronics* **70** (1991), 485.

[Hac86] F. Hache, D. Ricard and C. Flytzanis. *Journal of the Optical Society of America B* **3 (12)** (1986), 1647.

[Hag75] H. J. Hagemann, W. Gudat and C. Kunz. *Journal of the Optical Society of America* **65** (1975), 742.

[Hai95] R. Haight. *Surface Science Reports* **21** (1995), 275.

[Hen91] M. Henzler and W. Göpel. *Oberflächenphysik des Festkörpers*. Teubner Studienbücher, Physik (1991).

[Hen98] C. R. Henry. *Surface Science Reports* **31** (1998), 235.

[Hil01] A. Hilger, M. Tenfelde and U. Kreibig. *Applied Physics B* **73** (2001), 361 .

[Hor78] K. Horn, M. Scheffler and A. M. Bradshaw. *Physical Review Letters* **41** (1978), 822.

[Höv93] H. Hövel, S. Fritz, A. Hilger, U. Kreibig and M. Vollmer. *Physical Review B* **48** (1993), 18178.

[Höv97] H. Hövel, A. Hilger, I. Nusch and U. Kreibig. *Zeitschrift für Physik D* **42** (1997), 203 .

[Höv98] H. Hövel, B. Grimm, M. Pollmann and B. Reihl. *Physical Review Letters* **81 (21)** (1998), 4608.

[Kaw66] A. Kawabata and R. Kubo. *Journal of the Physical Society of Japan* **21** (1966), 1765.

[Ken01] C. Kennerknecht, H. Hövel, M. Merschdorf, S. Voll and W. Pfeiffer. *Applied Physics B* **73** (2001), 425.

[Kno96] E. Knoesel, A. Hotzel, T. Hertel, M. Wolf and G. Ertl. *Surface Science* **368** (1996), 76.

[Kor04] Z. Korczac, L. Douillard, F. Charra and H. J. Ernst. *Observation of localized enhancement in nonlinear photoemission from Cu surfaces* (2004). Contribution at the 4th international conference on LEEM/PEEM, May 9-13.

[Kos63] G. F. Koster, J. O. Dimmock, R. G. Wheeler and H. Statz. *Properties of the Thirty-Two Point Groups*. MIT Press, Cambridge, MA (1963).

[Kot01] J. P. Kottmann, O. J. F. Martin, D. R. Smith and S. Schultz. *Physical Review B* **64** (2001), 235402.

[Kre70] U. Kreibig and P. Zacharias. *Zeitschrift für Physik* **231** (1970), 128.

[Kre85] U. Kreibig and L. Genzel. *Surface Science* **156** (1985), 678.

[Kre93] U. Kreibig and M. Vollmer. *Optical Properties of Metal Clusters*. Springer Series in Materials Science (1993).

[Kre95] U. Kreibig and L. Genzel. *Surface Science* **156** (1995), 678.

[Kre99] J. R. Krenn, A. Dereux, J. C. Weeber, E. Bourillot, Y. Lacroute, J. P. Goudonnet, G. Schider, W. Gotschy, A. Leitner, F. R. Aussenegg and C. Girard. *Physical Review Letters* **82 (12)** (1999), 2590.

[Lam00] B. Lamprecht, G. Schider, R. T. Lechner, H. Ditlbacher, J. R. Krenn, A. Leitner and F. R. Aussenegg. *Physical Review Letters* **84** (2000), 4721.

[Leh00] J. Lehmann, M. Merschdorf, W. Pfeiffer, A. Thon, S. Voll and G. Gerber. *Physical Review Letters* **85 (14)** (2000), 2921.

[Lez02] H. J. Lezec, A. Degiron, E. Devaux, R. A. Linke, L. Martin-Moreno, F. J. Garcia-Vidal and T. W. Ebbesen. *Science* **297** (2002), 820.

[Lie93] A. Liebsch. *Physical Review B* **48 (15)** (1993), 11317.

[Lin01] S. Linden, J. Kuhl and H. Giessen. *Physical Review Letters* **86** (2001), 4688.

[Mai02] S. A. Maier, P. G. Kik and H. A. Atwater. *Applied Physics Letters* **81** (2002), 1714.

[Mai03] S. Maier, P. Kik and H. A. Atwater. *Phisical Review B* **67** (2003), 205402.

[Mar91] V. A. Markel, L. S. Muratov, M. I. Stockman and T. F. George. *Physical Review B* **43 (10)** (1991), 8183.

[Mar96] V. A. Markel, V. M. Shalaev, E. B. Stechel, W. Kim and R. L. Armstrong. *Physical Review B* **53 (5)** (1996), 2425.

[Mer00] M. Merschdorf, W. Pfeiffer, A. Thon, S. Voll and G. Gerber. *Applied Physics A* **71** (2000), 547.

[Mes81] B. J. Messinger, K. U. von Raben, R. K. Chang and P. W. Barber. *Physical Review B* **24** (1981), 649.

[Mic77] H. B. Michaelson. *Journal of Applied Physics* **48 (11)** (1977), 4729.

[Mie08] G. Mie. *Annals of Physics* **25** (1908), 377.

[Mül56] E. W. Müller. *Physical methods in chemical analysis*, vol. 3. Academic Press, New York (1956).

[Mon97] P. Monchicourt, M. Raynaud, H. Saringar and J. Kupersztych. *Journal of Physics: Condensed Matter* **9** (1997), 5765 .

[Mos85] M. Moskovits. *Review of Modern Physics* **57** (1985), 783.

[Nep85] S. A. Nepijko. *Physical Properties of Small Metal Particles*. Naukova Dumka, Kiev (1985).

[Nep02] S. A. Nepijko, N. N. Sedov, O. Schmidt, G. H. Fecher and G. Schönhense. *Annals of Physics (Leipzig)* **11** (2002), 39.

[Oel01] A. Oelsner, O. Schmidt, M. Schicketanz, M. Klais, G. Schönhense, V. Mergel, O. Jagutzki and H. Schmidt-Böcking. *Review of Scientific Instruments* **72 (10)** (2001), 3968.

[Oga96] S. Ogawa and H. Petek. *Surface Science* **363** (1996), 313.

[Ott68] A. Otto. *Zeitschrift für Physik* **216** (1968), 398.

[Pal85] E. D. Palik. *Handbook of Optical Constants of Solids*. Academic Press (1985).

[Paw98] S. Pawlik, R. Burgermeister, M. Bauer and M. Aeschlimann. *Surface Science* **402-404** (1998), 556.

[Per81] J. A. A. Perenboom, P. Wyder and F. Meier. *Physics Reports* **78** (1981), 173.

[Pet97] H. Petek and S. Ogawa. *Progress in Surface Science* **56 (4)** (1997), 239.

[Plu82] E. W. Plummer and W. Eberhardt. *Advanced Chemical Physics* **49 (1982)** (1982), 533.

[Prz04] M. D. V. Przychowski, G. K. L. Marx, G. H. Fecher and G. Schönhense. *Surface Science* **549 (1)** (2004), 37.

[Rae88] H. Raether. *Surface Plasmons on Smooth and Rough Surfaces and on Gratings*. Springer Berlin (1988).

[Roe] *www.roentdek.de*.

[SAE] *www.saesgetters.com/prdfr_amd.htm*.

[Sal00] L. Salomon, C. Charbonnier, F. de Fornel, P. M. Adam, P. Guérin and F. Carcenac. *Physical Review B* **62** (2000), 17072.

[Sam89] A. Samsavar, E. S. Hirschorn, F. M. Leibsle and T. C. Chiang. *Physical Review Letters* **63 (26)** (1989), 2830.

[Sas75] J. K. Sass. *Surface Science* **199** (1975), 444.

[Sch86a] G. Schönhense. *Applied Physics A* **41** (1986), 39.

[Sch86b] G. Schönhense, A. Eyers and U. Heinzmann. *Physical Review Letters* **56** (1986), 512.

[Sch00] O. Schmidt. *Betrachtung von chemichen Reaktionen und mesoskopischen Strukturen auf Oberflächen mittels spektroskopischer Photoelektronenmikroskopie*. Ph.D. thesis, Johannes Gutenberg-Universität Mainz (2000).

[Sch01a] M. Scharte, R. Porath, T. Ohms, M. Aeschlimann, J. R. Krenn, H. Ditlbacher, F. R. Aussenegg and A. Liebsch. *Applied Physics B* **73** (2001), 305 .

[Sch01b] O. Schmidt, G. H. Fecher, Y. Hwu and G. Schönhense. *Surface Science* **482-485** (2001), 687.

[Sch01c] G. Schönhense, O. Oelsner, O. Schmidt, G. H. Fecher, V. Mergel, O. Jagutzki and H. Schmidt-Böcking. *Surface Science* **480** (2001), 180.

[Sch02a] O. Schmidt, M. Bauer, C. Wiemann, R. Porath, M. Scharte, O. Andreyev, G. Schönhense and M. Aeschlimann. *Applied Physics B* **74** (2002), 223.

[Sch02b] C. Schneider and G. Schönhense. *Reports on Progress in Physics* **65** (2002), 1785.

[Sch02c] G. Schönhense and H. Spiecker. *Journal of Vacum Science and Technology B* **20 (6)** (2002), 2526.

[Sch03] B. Schechter. *New Scientist* **178 (2392)** (April 26, 2003), 31.

[Sha78] J. Shah. *Solid State Electronics* **21** (1978), 43.

[Sha96] V. M. Shalaev, C. Douketis, T. Haslett, T. Stuckless and M. Moskovits. *Physical Review B* **53 (16)** (1996), 11193.

[Sha00] V. M. Shalaev. *Nonlinear Optics of Random Media*, vol. 158 of *Springer Tracts in Modern Physics*. Springer (2000).

[Sha02] V. M. Shalaev. *Optical Properties of Nanostructured Random Media*. Topics in Applied Physics 82. Springer (2002).

[Smi69] N. V. Smith. *Physical Review* **183** (1969), 634.

[Sti99] F. Stietz and F. Träger. *Philosophical Magazine B* **79 (9)** (1999), 1281.

[Str41] J. A. Stratton. *Electromagnetic Theory*. McGraw-Hill Book Company, New York and London (1941).

[Sze64] S. M. Sze, J. L. Moll and T. Sugano. *Solid State Electronics* **7** (1964), 509.

[Tig93] J. Tiggesbäumker, L. Köller, K. H. Meiwes-Broer and A. Liebsch. *Physical Review A, Rapid Communications* **48 (3)** (1993), R1749.

[Tim04] C. Timm and K. H. Bennemann. *Journal of Physics: Condensed Matter* **16** (2004), 661.

[Ven94] J. A. Venables. *Surface Science* **299** (1994), 798.

[Voi01] C. Voisin, N. Del Fatti, D. Christofilos and F. Vallée. *Journal of Physical Chemistry B* **105** (2001), 2264.

[Wei02] M. Weinelt. *Journal of Physics: Condensed Matter* **14** (2002), R1099.

[Wer83] G. K. Wertheim, S. B. DiCenzo and S. E. Youngquist. *Physical Review Letters* **51** (1983), 2310.

[Wer88] G. K. Wertheim and S. B. DiCenzo. *Physical Review B* **37** (1988), 844.

[Woo81] D. M. Wood. *Physical Review Letters* **46** (1981), 749.

[Zie98] C. Ziethen, O. Schmidt, G. H. Fecher, C. M. Schneider, G. Schönhense, R. Frömter, M. Seider, K. Grzelakowski, M. Merkel, D. Funnemann, W. Swiech, H. Grundlach and J. Kirschner. *Journal of Electron spectroscopy and Related Phenomena* **88-91** (1998), 983.